This electronic thesis or dissertation has been downloaded from the King's Research Portal at https://kclpure.kcl.ac.uk/portal/

The Paradox of Youth, Dark Matter Accretion and Void Models

De Lavallaz, Arnaud

Awarding institution:
King's College London

The copyright of this thesis rests with the author and no quotation from it or information derived from it may be published without proper acknowledgement.

END USER LICENCE AGREEMENT

Unless another licence is stated on the immediately following page this work is licensed

under a Creative Commons Attribution-NonCommercial-NoDerivatives 4.0 International

licence. https://creativecommons.org/licenses/by-nc-nd/4.0/

You are free to copy, distribute and transmit the work

Under the following conditions:

- Attribution: You must attribute the work in the manner specified by the author (but not in any way that suggests that they endorse you or your use of the work).
- Non Commercial: You may not use this work for commercial purposes.
- No Derivative Works - You may not alter, transform, or build upon this work.

Any of these conditions can be waived if you receive permission from the author. Your fair dealings and other rights are in no way affected by the above.

Take down policy

If you believe that this document breaches copyright please contact librarypure@kcl.ac.uk providing details, and we will remove access to the work immediately and investigate your claim.

Download date: 05. May. 2023

This electronic theses or dissertation has been downloaded from the King's Research Portal at https://kclpure.kcl.ac.uk/portal/

KING'S College LONDON

Title: The Paradox of Youth, Dark Matter Accretion and Void Models

Author: Arnaud De Lavallaz

The copyright of this thesis rests with the author and no quotation from it or information derived from it may be published without proper acknowledgement.

END USER LICENSE AGREEMENT

This work is licensed under a Creative Commons Attribution-NonCommercial-NoDerivs 3.0 Unported License. http://creativecommons.org/licenses/by-nc-nd/3.0/

You are free to:

- Share: to copy, distribute and transmit the work

Under the following conditions:

- Attribution: You must attribute the work in the manner specified by the author (but not in any way that suggests that they endorse you or your use of the work).
- Non Commercial: You may not use this work for commercial purposes.
- No Derivative Works - You may not alter, transform, or build upon this work.

Any of these conditions can be waived if you receive permission from the author. Your fair dealings and other rights are in no way affected by the above.

Take down policy

If you believe that this document breaches copyright please contact librarypure@kcl.ac.uk providing details, and we will remove access to the work immediately and investigate your claim.

The Paradox of Youth, Dark Matter Accretion and Void Models

University of London
Arnaud de Lavallaz
PhD Thesis

October 2011

Contents

To my parents

Overview

Equipped with his five senses, man explores the Universe around him and calls the adventure Science.
- Edwin P. Hubble

A person who never made a mistake never tried anything new.
- Albert Einstein

Scientific curiosity and thirst for knowledge have driven human progress and helped mankind develop an always deeper understanding of our world. New - and sometimes controversial - ideas have been proposed in order to explain its mysteries. Looking for alternative perspectives has proven essential, particularly when the current paradigms do not give complete satisfaction.

Such is the case for three important questions in modern astrophysics and cosmology, which we intend to investigate: **the Paradox of Youth**, Dark Matter and Dark Energy. We will first explore a new possible explanation to the paradoxical observation of young, massive stars near the centre of our galaxy. Hosting a solar mass black hole might allow them to spare some of their burning material, giving them enough time to travel from further galactic distances. In the second part of our thesis, we will study **Dark Matter accretion** onto neutron stars. Considering different types of Dark Matter particles, we will determine the consequences of their capture by these very dense objects and look for observable signatures. Finally, our current views on Dark Energy will be examined through its role in **void models**. Among them, the Swiss-Cheese Universe and central void models will be analysed in order to evaluate the impact of inhomogeneities on the determination of cosmological parameters.

All three parts are similarly structured: conceptual introduction, analytical and computational considerations, commented results and conclusive remarks. Bibliographies are given separatly after each part. Lists of figures, tables and abbreviations can be found at the end of the document.

Part I

The Paradox of Youth

Chapter 1

Introduction

During our first year of research, we have been working mostly on theories and simulations concerning accreting objects - essentially black holes (Fig. 1.1) - in particular environments. Inspired by similar studies in the literature, we have been developing numerical tools in order to be able to implement our own simulation codes. Creating our own methods allows us to insure a thorough understanding of the numerical results, which proves essential when a higher degree of precision is required.

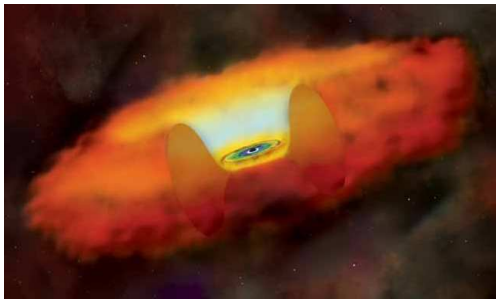

Figure 1.1: Artistic view of a black hole showing accretion of the surrounding material. [Credit: NASA/CXC/SAO]

The present part of our thesis aims at summarising the essential articles about the subject and provide the necessary background to understand the issues at stake. It contains analytical considerations which are used afterwards in our simulations and explains the approach we followed and the results we obtained. We will conclude this first part by giving an outlook of the future possible propsects in this domain.

The work presented here may be seen as a first self-consistent part investigating a possible explanation for the "Paradox of Youth". The numerical tools and the analytical aspects which are developed here will however be used as a base for the rest of our research. Before describing them in the following Chapters, we will briefly introduce the two main protagonists in this study: B-type main sequence stars and black holes.

Class	Temperature [K]	Apparent Colour	Mass $[M_\odot]$	Radius $[R_\odot]$	Luminosity $[L_\odot]$
O	$\geq$ 33,000	Blue	$\geq$ 16	$\geq$ 6.6	$\geq$ 30,000
B	10,000-33,000	Blue white	2.1-16	1.8-6.6	25-30,000
A	7,500-10,000	Blue white to white	1.4-2.1	1.4-1.8	5-25
F	6,000-7,500	White	1.04-1.4	1.15-1.4	1.5-5
G	5,000-6,000	Yellow-white	0.8-1.04	0.96-1.15	0.6-1.5
K	3,700-5,200	Yellow-orange	0.45-0.8	0.7-0.96	0.08-0.6
M	$\leq$ 3,700	Orange-red	$\leq$ 0.45	$\leq$ 0.7	$\leq$ 0.08

Table 1.1: Harvard spectral classification of stars [3]. In our research, we will be interested essentially in massive stars of type B.

1.1 B-Type Main Sequence Stars

Our research will focus on one particular type of stars which is but a part of the very complex theory of stellar evolution[1]. Our interest lies in a family of bright and large stars classified as B-type main sequence (hydrogen-burning) stars. Their surface temperature ranges between 10,000 and 33,000 K, giving them an apparent blue-white colour. They have a radius of 1.8 to 6.6 $R_\odot$[2]; their mass lies betwen 2 to 16 solar masses[3] and they are up to 30,000 times more luminous than our star[4].

B-type stars are among the most luminous stars in the Harvard spectral classification (Table 1.1), in which they were first identified through the presence of non-ionized helium lines, with no singly ionized helium line in the blue-violet portion of the spectrum. However, this characteristic distinction proved to lack consistency, and subsequent classifications are based on the strengths of absorption lines at specific frequencies.

Unlike the Sun, the interior structure of B-type stars shows no corona (most external plasmatic 'atmosphere' of a star) and no convection zone in their outer atmosphere. Their higher mass loss rate and luminous power result in a very short life expectancty, preventing them from travelling far from their birth place. Their core is surrounded by a convection zone caused by the highly energetic CNO cycle taking place at the centre of the star.

B-type stars tend to cluster with another type of stars, O-type stars, which are even larger and more luminous. These clusters are called OB associations and can usually be found in giant molecular clouds. One of the most famous among them, the Orion OB1 association, gathers a large part of the brighter stars of its constellation. It is estimated that about 1 star out of 800 main sequence stars in the vicinity of the Sun is identified as a B-type star.

[1] We will refrain from giving here a complete theoretical background on stellar evolution as this would hinder the conciseness of our discourse. Such information can easily be found in the literature, e.g. [1, 29].

[2] The radius of the Sun, noted $R_\odot$, is 6.955×10^8 m.

[3] A solar mass, noted $M_\odot$, is equal to 1.9891×10^{30} kg.

[4] The luminosity of the Sun is $L_\odot = 3.846 \times 10^{26}$ W.

1.2 Black Holes

The second objects we will be using in this study are black holes, which we are choosing for their accretion capacities. The first hint of their existence was given by an English clergyman and geologist, John Mitchell, at the end of the 18th century [4]. Using Newton's equations and theory of light, he considered the idea of a body so massive that even light could not escape it. Putting the escape velocity equal the speed of light, c, in Newton's equation $v = \sqrt{GM/r}$ shows that

$$R = \frac{2GM}{c^2} \approx 2.95 \left(\frac{M}{M_\odot}\right) \text{km}$$

is the radius of a star of mass M from which nothing can escape. This radius is known as the Schwarzschild radius R_S in the simple case of a non-rotating star [5].

It is conventionally thought that black holes are the results of the gravitational collapse of larger stars. Their collapsed core become ever denser until forming a singularity, a point of zero volume and infinite density where the whole mass of the black hole is located. This singularity can never be observed, however, as it has to be cloaked by an event horizon which materialises the spherical surface at $r = R_S$.

Direct observation of black holes is, by definition, impossible. But they can be detected indirectly through the emission of radiation caused by the accretion of matter. The gravitational well of a black hole attracts the surrounding gas which falls towards its centre, forming a disk-like structure around the object. Friction and the release of the gravitational energy increase the temperature of the gas, which becomes hot enough to emit vast amount of radiation (mainly X-rays). In the present study, we are particularly interested in these accretion processes, as they might bring an alternative explanation to the so-called "Paradox of Youth", presented in the next Section.

1.3 A Paradoxical Situation

According to the most recent astronomical observations, we presume that a super-massive black hole (SMBH), called Sagittarius A* (Sgr A*) and of mass $3.7 \times 10^6\, M_\odot$ [6], dwells in the very centre of our galaxy. Because of its huge mass, the SMBH causes tremendous tidal forces on the surrounding gas. As star formation usually results from condensing clouds of gas, these strong forces imply that burgeoning stars would have much more difficulty in gathering enough mass and reaching the critical conditions needed to initiate nuclear reactions and start their lives. Despite this seemingly hopeless situation, a cluster of young and massive stars has been discovered within the first parsec[5] (pc) around the SMBH. This apparent contradiction is referred to as the "Paradox of Youth" [7].

In order to explain this mystery, several hypotheses and models have been proposed during the past few years. In the next Section, we will briefly expose their main ideas and deduce from them the elements that lead our reflexion towards the new conceptual approach studied here.

[5] 1 parsec = 3.0857×10^{16} m = 3.26 light-years.

1.4 Previous Discussions

Some of the most interesting approaches concerning the question of the paradoxical star formation at the Galactic Centre have been discussed during Cornell University's Fall 2006 Astronomy 233 Symposium and summarised in its proceedings. We will briefly review them here and extend somewhat this survey in order to draw the overall picture.

1.4.1 Dense Gaseous Disk around the SMBH

In their paper [8], Levin and Beloborodov propose a new hypothesis to explain the presence of apparently young and massive stars in the vicinity of Sgr A* (Fig. 1.2). Since we believe that the formation of stars from standard molecular clouds should be impossible because of the important tidal forces exerted by the central black hole, the authors suggest that in situ stellar formation would have been conceivable if the presence of a very dense gaseous disk around Sgr A* could have supported it in the recent past.

In order to put their hypothesis to the test, the authors use data that have been collected about the orbital velocities of 13 stars orbiting close to the SMBH [9], among which 11 have been found to move in a clockwise direction in the sky. They manage to fit a plane for 10 of them with a relatively good precision and, comparing their dispersion to Monte Carlo simulations producing random velocity distributions, they concluded that these stars were formed from a dense gaseous disk surrounding Sgr A*.

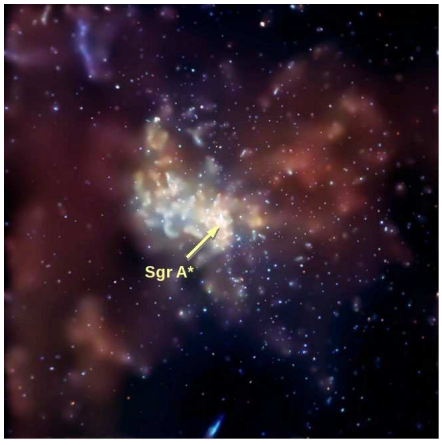

Figure 1.2: Image of the Galactic Centre (NASA's Chandra X-ray Observatory) with its SMBH, Sgr A* (arrow).
[Credit: NASA/CXC/MIT]

Refuting the idea that these stars could belong to a cluster that would have spiraled towards the SMBH due to gravity (see Subsection 1.4.4), the authors claim that the stars around it have formed from a dense disk-shaped molecular cloud that once orbited it. This dense gaseous disk could have influenced the orbit of other older stars that were initially inclined to the plane of the disk. It has also been shown [10] that the accretion matter from the disk could cause these stars to grow in size and appear as younger stars than they really are.

To explain the absence of any observable dense gaseous disk around Sgr A* at present, the authors argue that the accretion of mass by the newborn stars could cause gaps to appear in the disk and that the gas could be blown away by stellar wind. According to their hypothesis, the Paradox of Youth could thus be explained by noting that the strangely young stars around the SMBH actually are very young massive stars, recently formed in a dense gaseous disk which has now disappeared, or older stars whose orbits have been shifted due to the gravitational interaction with the gaseous disk and who seem younger due to the accretion of the disk's matter around their older cores.

1.4.2 Cluster of Stars Migrating towards the SMBH

An alternative model [11] that could give a sensible explanation to the observation of young, massive stars forming in a hostile environment is based on a rather simple but elegant idea: these stars might actually have formed at larger radii, where the tidal shear due to the central black hole is less extreme, and then have migrated towards the Galactic Centre. This model gets rid of the sufficiently dense gas clouds that are needed in other cases and yet not observed. However, it requires the stellar cluster to be dense enough to migrate to within a few arcseconds of the SMBH during the relatively short lifetime of its massive young stars; as a matter of fact, its density should be high enough to make its core collapse and contain an intermediate mass black hole (IMBH).

Using the data of a newly discovered comoving group of stars (called IRS 16SW) in the central parsec around the SMBH, the authors propose a formation mechanism suggesting that the observed group is the remnant core of an infalling stellar cluster. The results suggest that this group, whose members appear to be young and massive stars, is located at ~ 0.08 pc from the SMBH and orbits clockwise on the orbital plan.

There has been another such group, IRS 13 (see Subsection 1.4.3), observed within the central parsec to the SMBH and which might contain an IMBH as well. Although these two groups orbit in opposite ways and show some important differences - e.g. their stellar density number, they both contain young, massive stars presumably of similar ages, suggesting that the same formation mechanism must be applicable to both distinctive situations. The main issue with IRS 16SW is that, according to calculations, all stars of the group are not gravitationally bound to each other. In such a case, it is difficult to understand how such a comoving group can have survived in the tremendous tidal field of the SMBH. The authors suggest that it could be the remnant core of a tidally disrupted core. It has been shown [12] that, given the orbital period of IRS 16SW and assuming that it is the remaining core of a massive star cluster, disruption may have begun at larger radii (~ 0.4 pc) and spread in phase members of the cluster that now seem to lie on the same orbital plane as the rest of the comoving group. Similarly, IRS 13 could then be a second infalling cluster, orbiting in another plane and observed in an earlier stage of disruption.

1.4.3 IRS 13: a Cluster Harbouring an IMBH?

As previously mentioned, investigations have been made [6] about another cluster of unusual young, massive stars (IRS 13E) detected near the centre of our Galaxy. As in [11], the authors explore the possibility that the complex is a

remnant of a massive stellar cluster with a central IMBH that would balance the gravitational effects of Sgr A*. They analyse the proper motions of the stars in the IRS 13E complex using data from 10 years of near-infrared adaptative optics observations. Combining different methods, they find that the mass of the black hole should lie between $7,000\ M_\odot$ and $15,000\ M_\odot$ depending on its location with respect to the four main stars. Since the addition of other sources would cause the IMBH's mass to increase, the authors have chosen the mass required to bind the IRS 13E complex to be at least $10^4\ M_\odot$ as an order of magnitude estimate.

Such a black hole, given the interstellar medium and the warm dust located around the complex, should be detectable by its nonthermal radio and X-ray emissions. None of them have been observed though. The only radio emissions that are exhibited are most likely thermal emissions from a source of the complex or from colliding stellar winds. It is thus unlikely that an accreting IMBH exists in IRS 13E since the cluster does not show the presence of a black hole through its characteristic behaviour. However, according to the authors, the cluster could still be a cluster in the process of dissolution, but further studies are needed to solve this galactic riddle.

1.4.4 Other Important Contributions

Some other intriguing ideas have been developed in an attempt to explain the Paradox of Youth. As they can often be seen as references in most of the following papers, we believe that they deserve to be at least summarised here in a few words.

In his paper [12], Gerhard claims that, under plausible conditions, a cluster of massive young stars may form well outside the central few parsecs of our galaxy and then spiral into the Galactic Centre during the life-time of its most massive stars. On its way inwards, the cluster loses much of its mass and its dense core is finally disrupted deep in the galactic nucleus. According to his results, such a cluster could travel on a spiral path from its initial galactocentric radius of 30 pc and reach the first parsec around Sgr A* where its most massive and central components could actually be the unusually young stars that we observe today. In order to achieve this journey though, the cluster should be substantially more massive than the other ones (the Arches and Quintuplet) that are detected at similar radii. Such a large mass is also required to avoid too rapid dynamical dissolution in the strong tidal field caused by the SMBH.

Following the idea, the authors of [13] performed simulations with models of clusters that have an initial mass of 10^5–$10^6\ M_\odot$ and initial galocentric radii of 2.5–40 pc. The authors identified a few cases in which dynamical friction actually brings a cluster within the central parsec, but this is conceivable only if the cluster is either very massive ($\sim 10^6\ M_\odot$) or is formed quite near the SMBH ($\lesssim$ 5pc). Such a cluster would have too many massive stars compared to the number found in the central parsec and the surrounding volume. No satisfactory explanation has yet been proposed to explain this discrepancy.

In [14], Morris, studying the massive star formation near the Galactic Centre, examines the observed central cluster of luminous objects. Rejecting the idea that they could be massive young stars remaining from a recent episode of star formation, the author claims that compact remnants of massive stars that are massive enough (as for black hole remnants) would be susceptible to migrate

towards the Galactic Centre. A central cluster of such compact stellar remnants could provide for an alternative class of explanations for the Paradox of Youth: the luminosity of the luminous central objects could derive from accretion, either of the interstellar gas or, most likely, of a stellar atmosphere through a collision with a red giant. In the latter case, observations seem to indicate that a $\sim$ 10 $M_{\odot}$ black hole could acquire a temporary, optically thick atmosphere and appear externally as a luminous, massive and young blue star.

1.5 Accreting Black Holes inside Massive Stars

Extrapolating from the review of literature presented in the previous Section, we have good reasons to believe that accreting black holes inside massive young stars may provide a sensible explanation to the Paradox of Youth. In this context, we think that a deciding argument would be to actually investigate whether such astrophysical configurations are possible and stable enough to survive.

That is the reason why we propose to build some realistic models and perform a series of simulations, after having considered the main analytical aspects of the question. Solutions, if they exist, could play an important role in at least two attractive scenarii which will be summarised hereafter: migrating stars and accreting stars near the Galactic Centre.

1.5.1 Migrating Stars: A Question of Age

As seen in Subsection 1.4.2, one elegant hypothesis consists of supposing that the young, massive stars observed near the centre of our galaxy have in fact formed further away and then migrated towards Sgr A*. In [11], the authors must require that the density of the cluster is high enough to allow the migration to happen within the lifetime of its most massive components, i.e. a few millions years. Such a cluster should even host an IMBH in order to form and to travel quickly enough to its present position ($\sim$ 0.08 pc from the SMBH). However, as pointed out in [6], none of the standard characteristics of such an IMBH has been yet detected, making its presence rather unlikely.

One possible solution to its riddle could be that the stars in question are actually older that they seem and may have travelled a longer way inwards than what is usually believed. This would be conceivable if those stars hosted a solar mass black hole, swapping the nuclear energy for accretion luminosity, making them live longer provided that the black hole does not swallow them too rapidly.

1.5.2 Newborn Massive Stars in the Galactic Centre

Another use of successful simulations involving accreting black holes in stellar interiors could derive from the ideas presented in [14]: they claim that compact remnants of massive stars (e.g. black hole remnants) could acquire high luminosities by accreting interstellar gas or, more likely, through collision with other large objects. For example, they believe that a $\sim 10\ M_{\odot}$ black hole, when coming accross a red giant, may develop a luminous atmosphere and look like a young and massive star.

These ideas are supported by the fact that recent observations [15] around the Galactic Centre showed the presence of many compact objects, among which accreting neutron stars and black holes.

The two scenarii presented in this Section are the main motivations for our attempt to obtain stable solutions involving accreting black holes inside massive stars. Whether our simulations prove them possible or not, they hopefully will, in any case, bring us a better understanding of the physical phenomena taking place in such extreme situations.

Chapter 2

Theory and Numerical Models

After this historical and conceptual introduction, we will now present the necessary theoretical background to our study in order to provide some useful tools. After detailing some aspects of stellar structure, we will say a few words on the stellar modelling process and the influence of the black hole itself. The second half of the Chapter will be dedicated to numerical questions, and in particular the matching process we propose to implement.

2.1 Stellar Structure

Before we focus our attention on our specific problem implying knowledge about black holes and accretion processes, we ought to develop some tools which will prove useful once we will have to build our stellar model (see Section 2.3). The elements we basically need are the equations of stellar structure and some essential considerations about stellar energy sources and properties.

Thanks to the precise analysis of astronomical observations, one can determine a variety of quantities related to the outer layers of stars, such as luminosity, effective temperature and composition. Concerning their central regions, however, there is no direct way to observe and measure such quantities. We therefore have to deduce the internal structure of stars by creating computer models which are consistent with all known physical laws and which agree with the features observed at their surface. Although our theoretical knowledge of stars and the observations clearly show that they are dynamic objects, we will limit ourselves to considering the simple time-independant (static) case. In the next couple of Subsections, we will briefly derive two elements of stellar structure before presenting the general results used in our research.

2.1.1 The Adiabatic Temperature Gradient

It has been said that radiation dominates as an energy transport mechanism as long as the temperature gradient is not inachevably steep. As soon as a hot bubble of gas can continue to rise rather than to sink back down after being displaced upwards, convection takes place. To define a sensible criterion

between these two regimes, one needs to consider the hydrodynamics conditions that allow such a bubble to travel a certain distance within its surrondings, assuming it expands adiabatically.
After some calculations, we find that the criterion for convection to occur may be elegantly expressed as follows:

$$\frac{d\ln P}{d\ln T} < \frac{\gamma}{\gamma - 1}, \tag{2.1}$$

where $\gamma = \frac{C_P}{C_V}$ is the *heat capacity ratio* or *adiabatic index*, ratio of the heat capacity at constant pressure (C_P) and the heat capacity at constant volume (C_V). For an ideal monatomic gas, $\gamma = 5/3$ and convection will occur in any region of a star where $d\ln P/d\ln T < 2.5$.

To determine the adiabatic temperature gradient, let us consider a hot bubble of gas rising and expanding adiabatically before thermalizing. The way the bubble's temperature changes with radius is given by differentiating the ideal gas law (**??**):

$$\frac{dP}{dr} = -\frac{P}{\mu}\frac{d\mu}{dr} + \frac{P}{\rho}\frac{d\rho}{dr} + \frac{P}{T}\frac{dT}{dr}. \tag{2.2}$$

From the adiabatic gas law, we have $P = K\rho^\gamma$ which may be differentiated as

$$\frac{dP}{dr} = \gamma\frac{P}{\rho}\frac{d\rho}{dr}. \tag{2.3}$$

Combining (2.2) and (2.3) and assuming that μ is constant for simplicity, we obtain the adiabatic temperature gradient

$$\left.\frac{dT}{dr}\right|_{\text{ad}} = \left(1 - \frac{1}{\gamma}\right)\frac{T}{P}\frac{dP}{dr},$$

which, using Eq. (**??**) and the ideal gas law, may be rewritten as

$$\left.\frac{dT}{dr}\right|_{\text{ad}} = -\left(1 - \frac{1}{\gamma}\right)\frac{\mu m_H}{k_B}\frac{GM_r}{r^2}. \tag{2.4}$$

2.1.2 The Rosseland Mean Opacity

Let us begin by recalling the definition of opacity in the context of stellar interior. The energy generated by nuclear reactions is carried out by beams of light which, during their travel out to the surface, come accross stellar material and interact with it in different ways. We simply call *absorption* any event that happens to remove photons from those beams of light; we define the absorption coefficient, or opacity, κ_λ, which quantifies the change in the intensity, dI_λ, of a ray of wavelenght λ as it travels towards the surface through the expression

$$dI_\lambda = -\kappa_\lambda \rho I_\lambda ds, \tag{2.5}$$

where ρ is the density of the gas, I_λ the intensity of the beam and ds the distance travelled. The opacity has units of $\mathrm{m^2\,kg^{-1}}$ and may thus be seen as the cross section for absorbing photons of wavelenght λ per unit mass of the stellar material. Note that the λ subscript implicitly indicates that the opacity is wavelenght-dependant.

By convenience, it is however common to employ an opacity that has been averaged over all wavelenghts to produce a function that depends only on the composition, density and temperature. In our simulations, we use the Rosseland mean opacity which is an harmonic mean giving the greatest contribution to the lowest values of opacity and has a weighting function that depends on the rate at which the blackbody spectrum varies with temperature:

$$\frac{1}{\overline{\kappa}} \equiv \frac{\int_0^\infty \frac{1}{\kappa_\nu}\frac{\partial B_\nu(T)}{\partial T}d\nu}{\int_0^\infty \frac{\partial B_\nu(T)}{\partial T}d\nu}, \tag{2.6}$$

where $B_\nu(T)$, the Planck function, is given by $B_\nu(T) = \frac{2h\nu^3/c^2}{e^{h\nu/k_B T}-1}$. As there is no simple analytical expression for the Rosseland mean opacity, approximation formulae have been developed for the following *partial* opacities which are its components:

- Bound-free absorption opacity, also known as photoionization, occurs when an incident photon has enough energy to ionize an atom by removing an electron; its value is given by

$$\overline{\kappa}_{\rm bf} = 4.34 \times 10^{21}\frac{g_{\rm bf}}{t}Z(1+X)\frac{\rho}{T^{3.5}}\ \mathrm{m^2\ kg^{-1}}, \tag{2.7}$$

  where $g_{\rm bf}$ and t are the Gaunt's and guillotine correction factors, respectivelly, given by $t/g_{\rm bf} = 0.708\,[\rho(1+X)]^{0.2}$.

- Free-free absorption opacity, which is a scattering process, happens when a free electron, passing by an ion, absorbs a photon so that its speed increases; the reverse situation also exists, i.e. when an electron losses energy in the vicinity of an ion by emitting a photon - this is called free-free emission, or *Bremsstrahlung*, and can be expressed by

$$\overline{k}_{\rm ff} = 3.68 \times 10^{18} g_{\rm ff}(1-Z)(1+X)\frac{\rho}{T^{3.5}}\ \mathrm{m^2\ kg^{-1}}, \tag{2.8}$$

  where $g_{\rm ff}$ is a second Gaunt's factor, taken as being equal to 1 in our case.

- Electron scattering opacity occurs, obviously, when a photon in scattered - and not absorbed - by an electron through the processes of Thompson scattering (totally free electron) and Compton or Rayleigh scattering (electron loosely bound to an atomic nucleus). Since the cross sections of these processes are wavelenght-independant, their contribution to the Rosseland mean opacity takes a particularly simple form:

$$\overline{\kappa}_{\rm es} = 0.02(1+X)\ \mathrm{m^2\ kg^{-1}}. \tag{2.9}$$

- $\mathrm{H^-}$ ion photoionization is, as advertised, the ionization of an $\mathrm{H^-}$ ion, which is an hydrogen atom with an extra electron; this process might happen in stellar interiors when the temperature ranges between 3000 K and 6000 K and for densities between 10^{-7} and 10^{-2} kg m^{-3}. The corresponding formula is

$$\overline{\kappa}_{\mathrm{H^-}} = 7.9 \times 10^{-34}(Z/0.02)\rho^{1/2}T^9\ \mathrm{m^2\ kg^{-1}}. \tag{2.10}$$

Introducing and evaluating all these formulae, we finally obtain an usable form for the Rosseland mean opacity that we can compute for various values of temperature and density (Fig. 2.1).

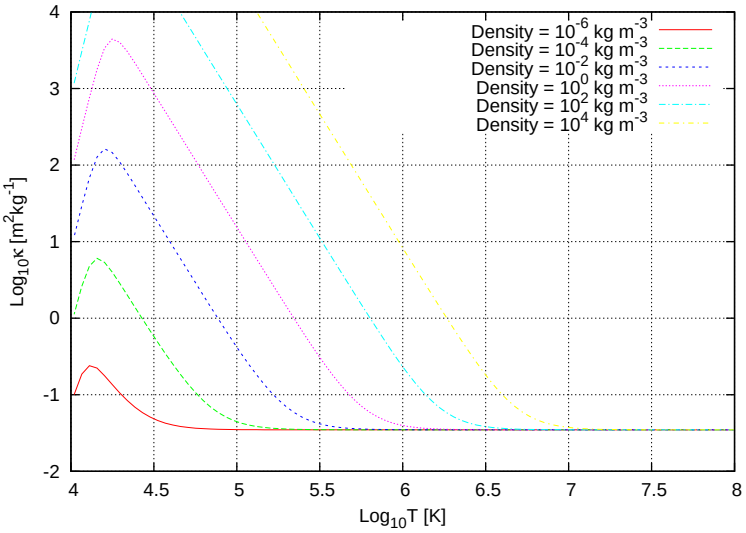

Figure 2.1: Numerical estimate of the Rosseland mean opacity for various densities, for the standard composition computed in our stellar models ($X = 0.74$, $Y = 0.24$).

2.1.3 Stellar Model Building

Besides the couple of theoretical elements presented in the previous Subsections, we use the standard results applicable for stellar structure and stellar nucleosynthesis: the equation of hydrostatic equilibrium (2.12), the equation of mass conservation (2.13), the luminosity gradient equation (2.14), the radiative temperature gradient (2.15) and the equation of state including the contribution due to radiation pressure, given by

$$P = \frac{\rho k_B T}{\mu m_H} + \frac{1}{3} a T^4 \tag{2.11}$$

The basic time-independant stellar structure equations may be summarised as follows:

$$\frac{dP}{dr} = -\frac{G M_r \rho}{r^2} \tag{2.12}$$

$$\frac{dM_r}{dr} = 4\pi r^2 \rho \tag{2.13}$$

$$\frac{dL_r}{dr} = 4\pi r^2 \rho \epsilon \tag{2.14}$$

$$\frac{dT}{dr} = -\frac{3}{4ac}\frac{\overline{\kappa}\rho}{T^3}\frac{L_r}{4\pi r^2} \qquad \text{(radiation)} \tag{2.15}$$

$$= -\left(1 - \frac{1}{\gamma}\right)\frac{\mu m_H}{k_B}\frac{G M_r}{r^2} \qquad \text{(adiabatic convection)} \tag{2.16}$$

In this last equation, we assume that the convective temperature gradient is purely adiabatic and is applied when

$$\frac{d\ln P}{d\ln T} < \frac{\gamma}{\gamma - 1}. \tag{2.17}$$

In order to express the density with quantities provided by the integration, we choose the equation of state (2.11) combining the ideal gas law and the contribution due to the radiation pressure. In Section 2.3, we will explain how we make use of these different expressions in the creation of stable stellar models.

2.2 Influence of the Black Hole

The presence of a very massive object, and in our case of a black hole, in the centre of the star will obviously cause some important changes in its equilibrium. In order to avoid tedious digressions, we decide to focus our attention on the analytical elements that we actually integrate into the numerical models presented in Sections 2.3 and 2.4.
Basically, the influence of the black hole inside a stellar interior concerns two main aspects: (1) the modification of the stellar structure equations, shown in Subsection 2.2.1 and (2) addition of an *initial* luminosity due to the accretion of stellar material by the black hole, discussed in Subsection 2.2.2.

2.2.1 Steady, Spherically Symmetric Accretion

To a certain extend, our case of study may be inspired by [16] where the authors consider a star of mass M accreting spherically symmetrically from a large gas cloud and which is at rest with respect to the gas. This case was first studied by [17], whose results will be used in the next Subsection. Even though many detailed studies have been undertaken since, like in [18, 19, 20] concerning accreting black holes or [21, 22, 23] about other aspects, they mainly refer to this key article when it comes to theoretical bases.

Our intention here is to derive the modified expression for the pressure gradient in order to adapt (2.12). Let us take spherical polar coordinates (r, θ, ϕ) with origin in the centre of the star. Our considerations are independant of θ and ϕ by spherical symmetry and the only component of the gas velocity is radial: $v = v_r$. For a steady flow, the standard continuity equation $\frac{\partial \rho}{\partial t} + \overrightarrow{\nabla} \cdot (\rho \overrightarrow{v}) = 0$ reduces to $\frac{1}{r^2}\frac{d}{dr}(r^2 \rho v) = 0$, which simply integrates to $r^2 \rho v =$ constant, where v is the inwards velocity of the gas. Since ρv is the inwards flux of material, the constant must be related to the accretion rate $\dot{M}$, which is constant too. The relation is given by

$$\dot{M} = 4\pi r^2 \rho v. \tag{2.18}$$

If we now consider the following form of the Euler equation:

$$\rho \frac{\partial \overrightarrow{v}}{\partial t} + \rho(\overrightarrow{v} \cdot \overrightarrow{\nabla})\overrightarrow{v} = -\overrightarrow{\nabla} P + \overrightarrow{f} \tag{2.19}$$

and apply it to our situation where the only contribution to the external force, $\mathbf{f}$, is from gravity and only has the radial component $f_r = -GM\rho/r^2$, we get this quite manageable equation:

$$v\frac{dv}{dr} + \frac{1}{\rho}\frac{dP}{dr} + \frac{GM}{r^2} = 0. \tag{2.20}$$

By reorganizing it, we can isolate the pressure gradient

$$\frac{dP}{dr} = -\frac{GM\rho}{r^2} - \rho v \frac{dv}{dr}. \tag{2.21}$$

Then, using (2.18), we obtain $\frac{dv}{dr} = -\frac{\dot{M}}{4\pi\rho r^2}\left(\frac{2}{r} + \frac{1}{\rho}\frac{d\rho}{dr}\right)$ and may substitute the corresponding term in (2.21) so that we finally get the following expression:

$$\frac{dP}{dr} = -\frac{\rho}{r^2}\left[GM - \left(\frac{\dot{M}}{4\pi\rho r}\right)^2\left(\frac{2}{r} + \frac{1}{\rho}\frac{d\rho}{dr}\right)\right]. \tag{2.22}$$

2.2.2 Accretion Rate and Luminosity

In order to know how to modify the pressure gradient through Eq. (2.22), one needs to determine the accretion rate $\dot{M}$ which appears in it. A most essential work concerning accreting bodies has been done by Herman Bondi around the middle of the previous century; we will base our calculations mainly on his original results.

In the previous work [24, 25, 26, 27], authors studied the case in which a star accreted material while moving through a gas cloud and its accretion rate was limited principally by its relative motion. In all this work, pressure effects were neglected, the argument being that any heat generated would be radiated away rapidly so that the temperature of the gas is always very low.

In [17] though, Bondi investigates spherically symmetrical accretion for a star which is at rest in an infinite cloud of gas. Thus, instead of simplifying the insuperable general problem by neglecting pressure effects as in the previous papers, he chooses the opposite extreme by ignoring the dynamical effects. The problem is defined as follows: a star of mass M is at rest in an infinite cloud of gas, which is also at rest at infinity and whose density ρ_∞ and pressure P_∞ are uniform. The motion of the gas is spherically symmetrical and steady, the increase in mass of the star being ignored so that the field of force is unchanging. The pressure P and the density ρ are related by $\frac{P}{P_\infty} = \left(\frac{\rho}{\rho_\infty}\right)^\gamma$, where γ is a constant satisfying $1 \leqslant \gamma \leqslant \frac{5}{3}$. Using the equation of continuity (2.18), the author analyses the behaviour of different functions implied in the mathematical simplification of the problem and first states that the accretion rate may not exceed the value

$$\dot{M}_{\text{Bondi}} = 4\pi\lambda_c(GM)^2 c_s^{-3}\rho_\infty, \tag{2.23}$$

where $\lambda_c = \left(\frac{1}{2}\right)^{(\gamma+1)/2(\gamma-1)}\left(\frac{5-3\gamma}{4}\right)^{-(5-3\gamma)/2(\gamma-1)}$ and $c_s = \left(\gamma\frac{P_\infty}{\rho_\infty}\right)^{1/2}$, which is the adiabatic sound speed. Since, in the previous work involving the star relative velocity v, the accretion rate was given by $\dot{M} = 2\pi\alpha\,(GM)^2\,v^{-3}\rho_\infty$, Bondi finally conjectures that the formula

$$\dot{M} = 2\pi\,(GM)^2\left(v^2 + c_s^2\right)^{-3/2}\rho_\infty \tag{2.24}$$

is likely to represent the order of magnitude of the accretion rate in the general case, where a star of mass M moves with relative velocity v in an uniform cloud of gas.

2.2.3 Quasi-stars: A Model of Accretion inside Gaseous Envelopes

We now have a better idea of what happens around an accreting object but we still have not said anything specific about our own situation, i.e. an accreting

black hole inside a stellar interior. The analytical model developped in Subsections 2.2.1 and 2.2.2 need to be taken one step further: we must swap the accreting star for a much denser object - a black hole. In the literature, one can find several inspiring examples which could be useful in such a quest: some of them consider actual black holes [28, 29, 30, 31, 32], the others degenerated neutron cores or Thorne-Żytkov objects [33, 34, 35].

All these works have been used in [36] in order to study the structure and evolution of "quasi-stars", accreting black holes embedded within massive hydrostatic gaseous envelopes. Its actual aim is to propose a model for the early growth of supermassive black holes, but some elements of its analytical considerations may be of interest to us. In this article, the authors consider a black hole of mass M_{BH} embedded within an envelope of mass $M_\star \gg M_{BH}$; the luminosity of the quasi-star is generated exclusively by black hole accretion, which adjusts so that the luminosity carried by the convective envelope equals the Eddington limit (see Subsection 2.2.4) for the total mass $M_\star + M_{BH} \backsimeq M_\star$. This implies that the envelope is strongly convective - since the radiation diffusion would not be efficient enough, and its structure resembles an $n = 3$ ($\gamma = 4/3$) polytrope.

The central region of such a polytrope has approximately uniform density (ρ_c), temperature (T_c) and pressure ($P_c = aT_c^4/3$). Using [17] and [29], the authors determine the adiabatic accretion rate

$$\dot{M}_{\text{Bondi}} = \frac{4\pi}{\sqrt{2}} \frac{(GM_{BH})^2 \rho_c}{c_c^3}, \tag{2.25}$$

where $c_c = (\frac{4}{3}\frac{P_c}{\rho_c})^{1/2}$ is the adiabatic sound speed. They write the luminosity as $L_{BH} = \epsilon \dot{M}_{BH} c^2$, where $\epsilon \sim O(0.1)$ is the (here constant) efficiency of energy output and $\dot{M}_{BH}$ is the actual accretion rate. In the absence of an efficient exhaust, such as a jet or evacuated funnel, this energy must be carried beyond the Bondi radius[1] convectively, by the accreting gas itself. Based on [37, 38, 39], they conclude that the accretion rate should be reduced below the Bondi value by a factor of the order $\epsilon^{-1}(c_c/c)^2 \ll 1$ and they adopt the following expression for the accretion luminosity

$$L_{BH} = 4\pi\alpha (GM_{BH})^2 \rho_c^{3/2} P_c^{-1/2}, \tag{2.26}$$

where $\alpha < 1$ accounts for energy sink within the Bondi radius: inefficient convection, presence of outflows, etc.

2.2.4 The Eddington Limit

If we innocently apply Eq. (2.25) and (2.26) to our particular situation, we get very high values for both accretion luminosity and rate. Physical conditions in a stellar interior are indeed very different from the environment usually considered when studying accreting objects: since the black hole is situated in the very heart of the star, temperature, pressure and density reach high values and their influence on the calculation of L_{BH} and $\dot{M}_{BH}$ is dramatic. So dramatic in fact that it does not make sense any more to estimate those values through the same scheme as [36] since they were interested in much bigger gas envelopes than we are, with much lower density and pressure.

[1] The Bondi radius is defined as follows: $R_{\text{Bondi}} = GM_{BH}/c_\infty^2$, where c_∞ is the sound speed in the environment far away from the accreting black hole.

We cannot rely on these approximates because they would provide us with luminosities which would exceed the Eddington luminosity. The latter, also called the Eddington limit, is defined in a star as the point where the gravitational force inwards equals the continuum radiation force outwards - assuming hydrostatic equilibrium and spherical symmetry. It thus corresponds to the maximal luminosity for a given mass. For luminosities exceeding Eddington's, a star would initiate a very intense stellar wind, blowing away its outer layers. In our case, this wind would simply prevent more material from falling into the central black hole.

This happens when the pressure gradient (2.12) equals the radiation pressure gradient given by

$$\frac{dP}{dr} = -\frac{\sigma_T \rho}{m_P c}\frac{L}{4\pi r^2}, \tag{2.27}$$

where σ_T is the Thomson scattering cross section for electron and m_P the mass of the proton. Equaling (2.12) and (2.27), we get the following expression for the Eddington limit

$$L_{Edd} = \frac{4\pi G M m_P c}{\sigma_T} \tag{2.28}$$

$$\approx 1.3 \times 10^{31} \left(\frac{M}{M_\odot}\right) \mathrm{W} \tag{2.29}$$

$$\approx 3.4 \times 10^{4} \left(\frac{M}{M_\odot}\right) L_\odot. \tag{2.30}$$

This constraining equation must be taken into account. However, it is not quite sufficient to directly apply it to our rather tricky situation: the hydrodynamics of accretion onto black holes proves to be complicated mostly because the lack of hard surface in a black hole makes the radiation efficiency, $e = L/\dot{M}c^2$, unkown a priori. Further discussion is needed to understand the accretion flow and its influence on the stellar equilibrium.

2.2.5 Hydrodynamics of Accretion onto Black Holes

Because of the lack of constraints on the accretion rate we just mentionned, we need more information in order to be able to draw the domains of possible solutions involving accreting black holes in gaseous surroundings. In [40], various families of solutions of axisymmetric flows are proposed, which may successfully model our own accretion system.

Considering that spherical accretion onto a black hole generally depends on the parameters $l \equiv L/L_{Edd}$ and $\dot{m} \equiv \dot{M}_{BH}/\dot{M}_{Edd}$, the authors show that, if we require the self-consistency between the gas and the radiation field, only certain combinations of the accretion rate and luminosity are allowed, i.e. a given type of solutions is described by a line on the $(l, \dot{m})$ plane. Three groups of solutions are then discussed: (1) solutions with $\dot{m} \ll 1$; (2) low-temperature solutions with $\dot{m} \gtrsim 0.1$ and (3) high-temperature solutions with $\dot{m} \gtrsim 0.1$. In this review, we will focus our attention on the latter case since it is of greater interest to us.

It has been proved by the authors that high luminosity accretion solutions are possible if the infalling gas can be preheated by outcoming radiation produced at smaller radii; these higher temperature and higher efficiency steady-state solutions exist only for $3 \lesssim \dot{m} \lesssim 100$. In those situations, gas temperature is

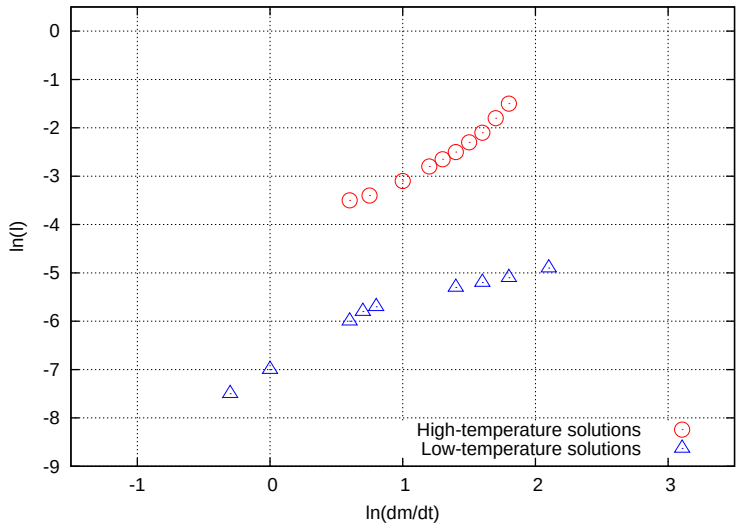

Figure 2.2: Spherical accretion flow solutions in relative luminosity l vs. accretion rate $\dot{m}$ for systems where $\dot{m} \gtrsim 0.1$, for low temperatures (triangles) and high temperatures (circles).

higher that 10^4 K and can reach up to $10^9 \sim 10^{10}$ K. The flow is optically thick to scattering and a process of radiation trapping occurs near the hole. This happens when the diffusion speed of photons is slower than the bulk velocity of the flow so that most of the photons are carried inwards with it. These solutions (see Fig. 2.2, results from [41]) are much more luminous and produce much harder photons than the low-temperature solutions of the same mass accretion rate: typical values are $l \backsimeq 10^{-4} - 10^{-2}$ and $\dot{m} \backsimeq 1 - 10^2$, as predicted. All these spherical accretion systems are still much less efficient than the thin disk accretion, thought to be the most effective accreting process, since their typical value is $e \sim 10^{-4}$. These solutions will be explored in Section 2.4 through our numerical models.

2.3 Numerical Models of Stable Stars

The very first step in the process of elaborating numerical models is to obtain simple stars that are stable and present realistic features. As we want to make sure that we completely control and understand our simulations, we decide to write our own code (in C++), based on other existing programs such as StatStar [29] and ZAMS.FOR [1]. As in these programs, our first objective is to obtain homogeneous zero-age main-sequence (ZAMS) models, i.e. stars whose composition is fixed throughout their interior.

2.3.1 Stellar Structure Code

There are many ways of solving the set of equations summarised in Subsection 2.1.3, but we need to make sure that the one we choose is compatible with the

future developments we intend to bring - including a very massive accreting object at the centre of the stars.

Looking at both programs we were refering to and making our own predictions in terms of applicability, we progressively elaborate a solution which fulfils our needs. The idea is basically to match an outwards and an inwards integrations at some given point in the star.
Its structure may be divided as follows:

1. We choose an initial radius, R_{min}, close enough to the stellar centre, at which we define the initial conditions (considered as the *central* conditions) for an outwards integration; among these conditions, the central pressure and temperature are first guessed but will be able to vary through the application of the matching process (see Subsection 2.3.3).
   The central density is computed through the equation of state (Eq. 2.11) and all the dependant functions, e.g. the nuclear reaction rate or the opacity, are calculated. The set of differential equations is then integrated, using a fourth order Runge-Kutta method, until a given radius, R_{o-i} (the chosen point within the stellar interior where the outwards and inwards integrations should meet), is reached;

2. In parallel, we use a "Surface Function" (see Subsection 2.3.2), with guessed values for the total mass and luminosity of the star, in order to get non-zero values for all the parameters at a given radius, R_{i-s}, very close to the surface. From that point, we can integrate inwards until we reach the radius R_{o-i} previously defined;

3. We now have two sets of different values for pressure, temperature, mass and luminosity at the matching point R_{o-i}; since our objective is to obtain a continuous behaviour for all the significant parameters throughout the interior of the star, we simply apply the matching process which, by slightly varying the different inputs, will try and find the best solution for a given radius.

The set of ordinary differential equations is solved by using a fourth order Runge-Kutta method (often referred to as "RK4"). It is generally considered to provide an excellent balance of power, precision and simplicity to program.

2.3.2 The Surface Function

Our stellar structure code, as most of other existing programs, makes the simplifying assumption that pressure, temperature and density are all zero at the surface of the star. Even if it seems rather reasonable, this assumption implies that we would not be able to integrate inwards starting with these initial conditions, since the gradient for all fundamental physics parameters (see set of equations in Subsection 2.1.3) depend on the density - which equals zero.

In consequence, we need to implement a subroutine which will approximate the inwards integration until a given radius R_{i-s} close to the surface (typically, $R_{i-s} = 0.999\, R_s$), but where the non-zero values for the physical parameters will allow us to perform a numerical integation. Assuming that the interior mass and luminosity are both constant through a small number of surface zones (which is sensible since temperature and density are very low), assuming furthermore

that electron scattering and H^- ion opacities may be neglected in these regions and using the stellar structure equations, it is possible to derive an expression for P depending on T:

$$P = \left(\frac{1}{4.25}\frac{16\pi}{3}\frac{GM_s}{L_s}\frac{ack_B}{A\mu m_H}\right)^{1/2} T^{4.25}, \tag{2.31}$$

where $A = (\overline{\kappa}_{\rm bf} + \overline{\kappa}_{\rm ff})\,\frac{T^{3.5}}{\rho}$. We can now write T in terms of the independant variable r through Eq. (2.15), and, using the ideal gas law and Kramers opacity laws (Eq. (2.7) and (2.8)), we may integrate and get

$$T = GM_s\left(\frac{\mu m_H}{4.25k}\right)\left(\frac{1}{r} - \frac{1}{R_s}\right). \tag{2.32}$$

Those expressions are applicable if we assume that the surface of the star is radiative. In the case that it is convective, a similar procedure can be used and leads to a slightly different equation for the temperature:

$$T = GM_s\left(\frac{\gamma - 1}{\gamma}\right)\left(\frac{\mu m_H}{k_B}\right)\left(\frac{1}{r} - \frac{1}{R_s}\right). \tag{2.33}$$

Assuming that the convection is adiabatic in our simple models, the pressure may then be found using the adiabatic relationship between pressure and density and the ideal gas law.

2.3.3 Defining and Refining the Matching Process

One of the most important elements in our stellar model building is the definition of the matching process that we use to obtain continous solutions between the outwards and inwards integrations. Such a matching process is highly dependent on the structural logic of each program and must be finely tuned to produce coherent results. That is the reason why we think that it is worth briefly describing our approach and some of the issues we came accross.

Let us first show the - rather intuitive - form we use to evaluate the error relative to a given solution. If we compare N parameters at the matching point, then the error is given by

$$\text{error} = \sum_{i=1}^{N}\left(\frac{X_i^{out} - X_i^{in}}{X_i^{out} + X_i^{in}}\right)^2, \tag{2.34}$$

where X_i^{out} and X_i^{in} are the values of the ith parameter, given by the outwards and inwards integrations respectively. The objective of the matching process is of course to reduce this error without being trapped in some fallacious minimum.

Since our intention is, ultimately, to modify the central conditions of the star by putting a black hole in its heart, the design of our matching process must allow such an operation without compromising its stability. Therefore, our first attempt actually consisted of matching the outwards integration with the outputs of the "Surface Function" by varying the central pressure and temperature. However, it proved almost impossible to match them without requiring a ridiculously high precision for the initial conditions.
Analyzing step by step the procedure, we found that this problem was due to a

strong instability in the temperature gradient - a small change in the conditions causing a considerable difference in the final values. In order to solve this point of issue, we tried several methods and algorithms: Markov Chain Monte Carlo, concentric squared domain in the space of solutions, or even scanning large areas of this same space. But in all these cases, the required accuracy was so high that the solutions we got did not make sense any more.

We had to find a way to get rid of this dramatic divergence. The most decisive improvement was made when we decided to set the matching point somewhere within the stellar interior and to perform a double integration towards this point, from the centre and from the surface.
The final solution we opted for is the following:

- We define small perturbations for all the parameters we want to vary (central pressure and temperature, total mass and luminosity);
- Then we add or remove these perturbative values and we test all the possible combinations of parameters;
- The one with the smallest error wins and one step is taken in that direction;
- We stop the matching process when a solution is reached or if the improvement of the error becomes insignificant.

The two graphs shown in Fig. 2.3 illustrate how the matching process works in the case of the temperature profile.

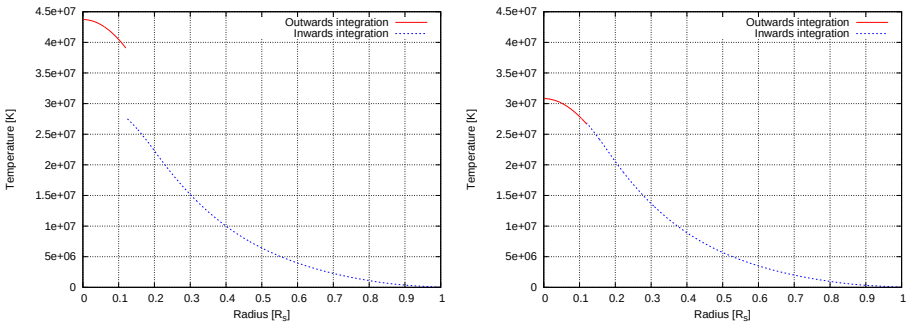

Figure 2.3: Application of the matching process (with a matching point at 0.12 R_s) in the case of the temperature profile for a ZAMS star whose radius $R_s = 4.48\,R_\odot$, initial (left) and final situations (right).

For our first trials, we included only a few terms (e.g. pressure and temperature) in the expression (2.34). But it quickly became evident that we need to be more demanding if we want to ensure a smooth continuity at the matching point. We have thus progressively added new terms in the calcultation of the error so that the actual version of Eq. (2.34) contains all the following elements within the sum: pressure, termperature, mass, luminosity and their first derivative.

2.3.4 Building the Hertzsprung-Russell Diagram

The best way to convince ourselves that the stellar structure code we developed is coherent, is to try and build the Hertzsprung-Russell (HR) diagram for the ZAMS stars we find. The idea is simply to start with a given solution, a solar model for instance, and increase the radius step by step and find a new stable solution for each new radius.

Our results are presented in Fig. 2.4. We start with a stellar solution based on the radius of the Sun ($R_s = 6.955 \times 10^8$ m) and we slowly follow the path towards bigger stars. Three main features may be observed in the graph (as pointed by arrows, in order of increasing luminosities): (1)[Conv./Rad.] the transition between solutions with convective surfaces to those with radiative surfaces, which happens when the CNO cycle becomes significantly efficient compared to the proton-proton chain (in our case, the transition takes place at $M_s \sim 1.3\,M_\odot$); (2)[CNO/PP] this slight bump corresponds to the end of the transition we just discussed, when the CNO cycle has overtaken the proton-proton chain and imposes its behaviour; (3)[Change in B-V] this bend is directly implied by the variation of scale in the determination of the B-V index.

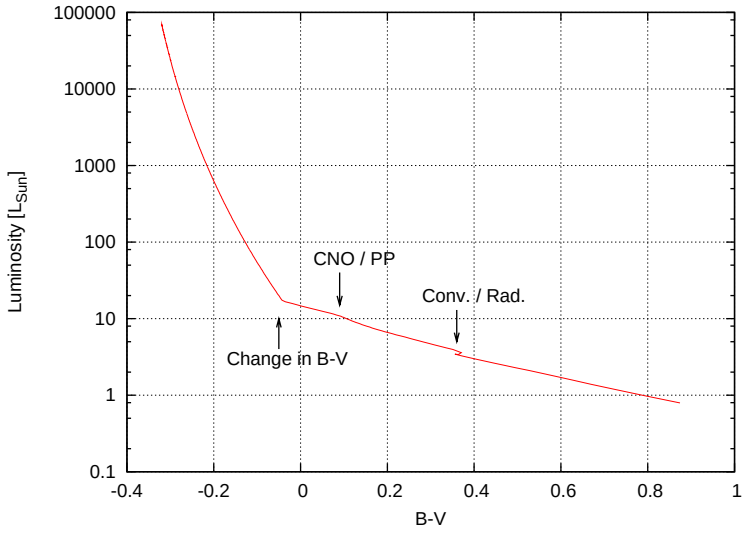

Figure 2.4: Hertzsprung-Russell diagram for ZAMS stars created by the final version of our stellar structure code with a working matching process as described in the Subsection 2.3.3.

The HR diagram we present here may be compared to a standard HR diagram (Fig. 2.5) as usually published in the literature. Our results correspond to the upper zone of the main sequence.

The range of masses where we should find interesting stars for our research lies between 10 and 20 $M_\odot$, according to the results presented in [7]. As an example, we show in Fig. (2.6) the behaviour of the essential physical parameters with regard to the radius, for a 10 $M_\odot$ star obtained with our stellar structure code.

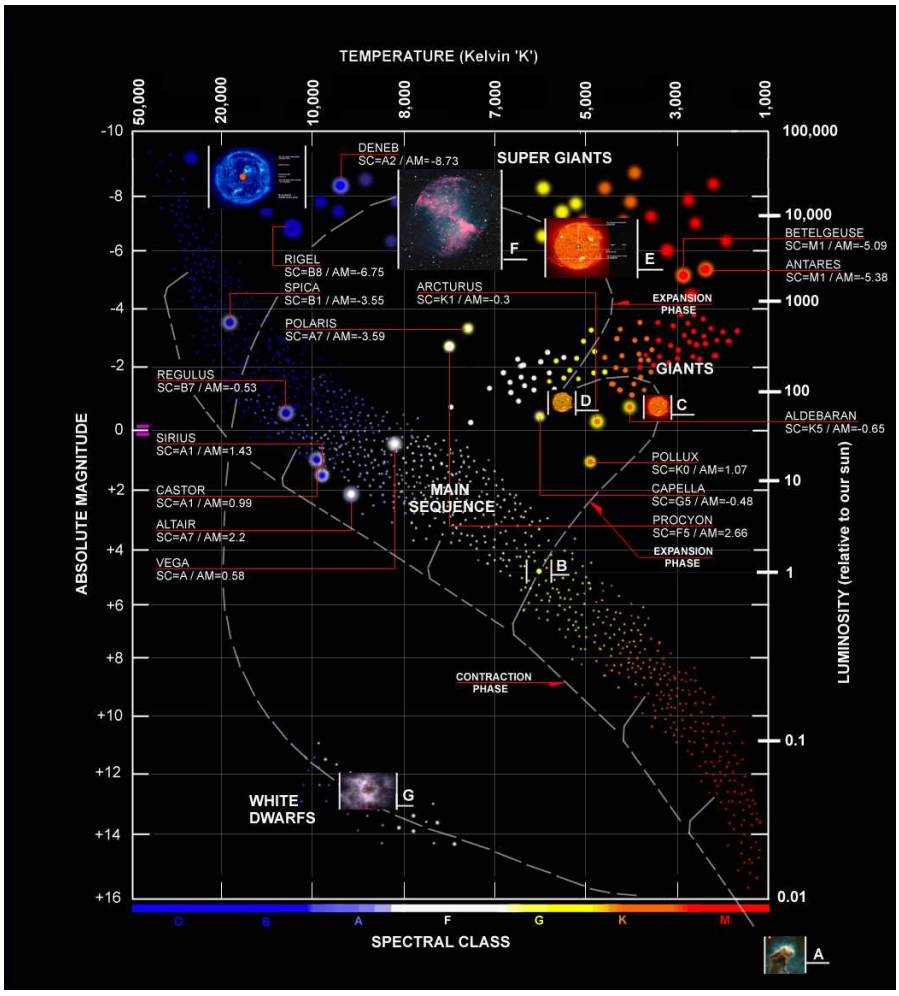

Figure 2.5: Standard Hertzsprung-Russell diagram as commonly shown in the literature. Our simulated results correspond to the upper part of the main sequence. [Credt: OMOS]

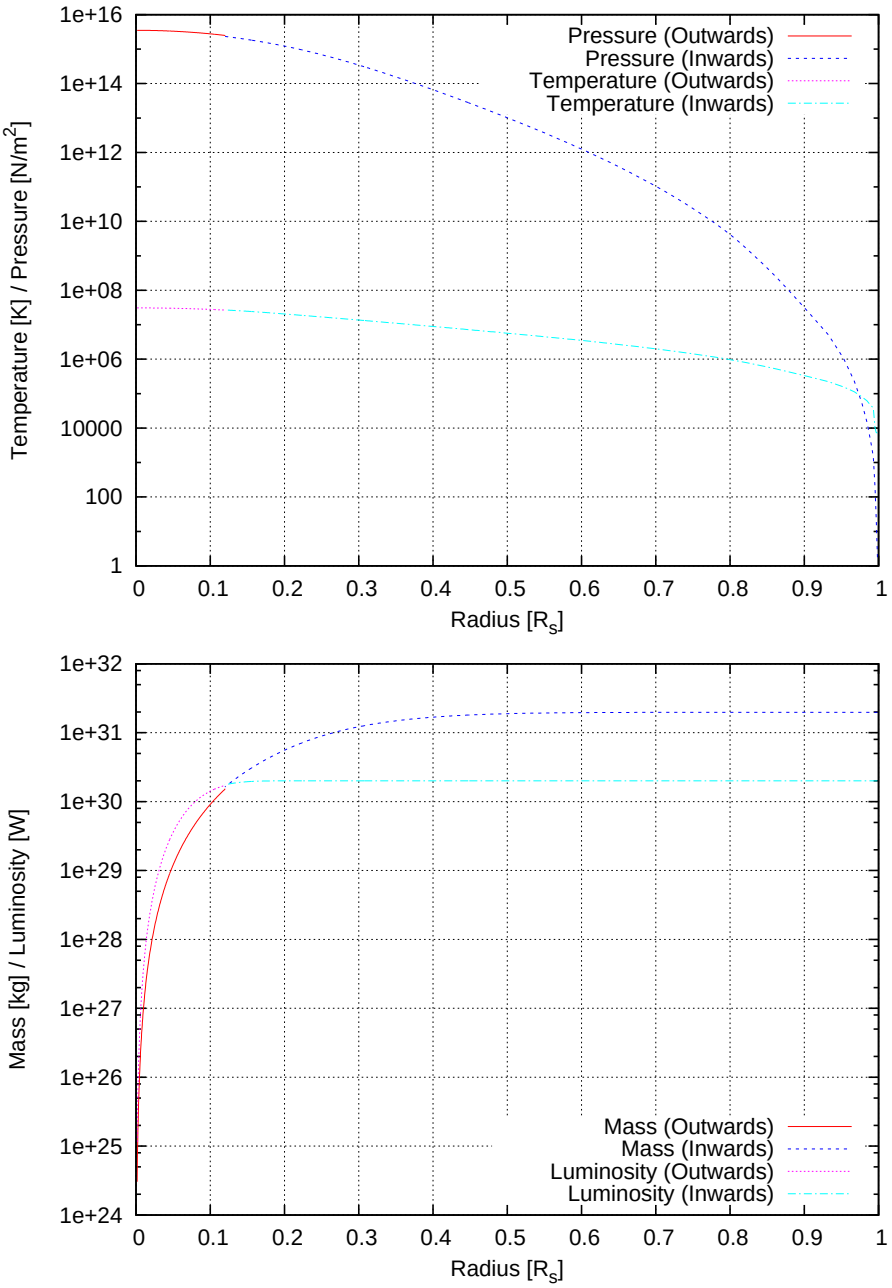

Figure 2.6: Main physical parameters in a typical stellar interior ($10\ M_\odot$ ZAMS star) produced by the code and the matching process described in this Chapter: pressure and temperature (top); mass and luminosity (bottom).

2.4 Including Black Holes in the Stellar Interior

Now that we have a series of stable stars with various radii and masses, we may choose some of them in order to include a black hole in their centre. But what does it actually mean in terms of coding aspects? Since we start our outwards integration with initial conditions for a given radius R_{min}, as explained in Subsection 2.3.1, the first modification is to simply add the mass of the central black hole and the accretion luminosity it is causing, as shown in Fig. (2.7). This change will of course have consequences in the behaviour of all other parameters. In order to master them, we proceed by small perturbations: once we have a stable solution for a tiny black hole, we slightly increase its mass and run the matching process until we find a new satisfactory solution.

The calculation of the accretion luminosity is based on a critic choice according to our discussion in Subsections 2.2.3 and 2.2.4. Since the actual conditions involved in our rather extreme case may cause the luminosity to cross the Eddington limit, we systematically choose the minimum between the values provided by Eq. (2.26) and (2.28).

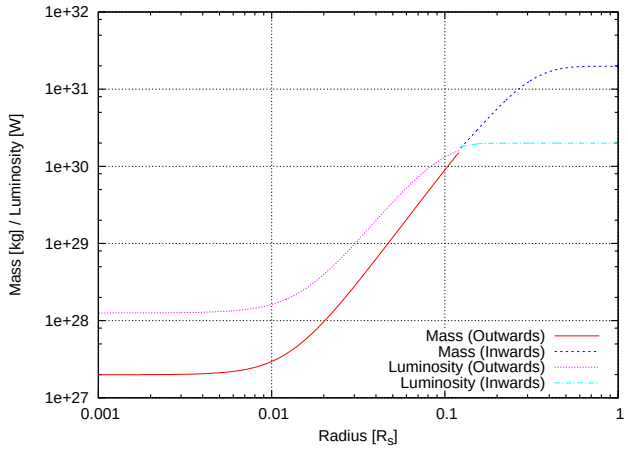

Figure 2.7: Influence in terms of initial mass and luminosity when including a 0.01 $M_\odot$ black hole in the centre of the same 10 $M_\odot$ ZAMS star as presented before. Both parameters are seriously increased at R_{min} while the matching process tries and copes with this new set of conditions.

The other important modification is the change in the equations describing the stellar interior. Because of the accretion, the pressure gradient is indeed modified by the addition of a new term due to the velocity of the infalling material $\rho v \frac{dv}{dr}$. The set of equations is thus composed of Eq. (2.13) to (2.16), plus the expression (2.22) previously derived.

The calculation of the appropriate accretion rate is based either on Bondi's formula (2.23) or on the expression for the Eddington limit, $\dot{M}_{Edd} = L_{Edd}/c^2$, depending on the option presenting the minimal luminosity. In case the Eddington scheme is chosen, coefficients may be added in order to reproduce the set of solutions discussed in Subsection 2.2.5.

The corresponding version of our code, including the matching process and the adaptations for the black hole accretion, is presented in Annexe A.

Chapter 3

Results and Discussion

Due to the structure of our code, we perform series of simulations for stars with given radii following the procedure described in Section 2.4. Including a black hole in a stellar core has, as one could expect, important consequences in terms of hydrostatic equilibrium. One of them is the change in mass occuring as the central black hole slowly increases. This behaviour depends on the initial conditions and particularly on the initial stellar mass considered. In Fig. 3.1, examples of such trends are shown for masses ranging from 5 to 10 $M_{\odot}$.

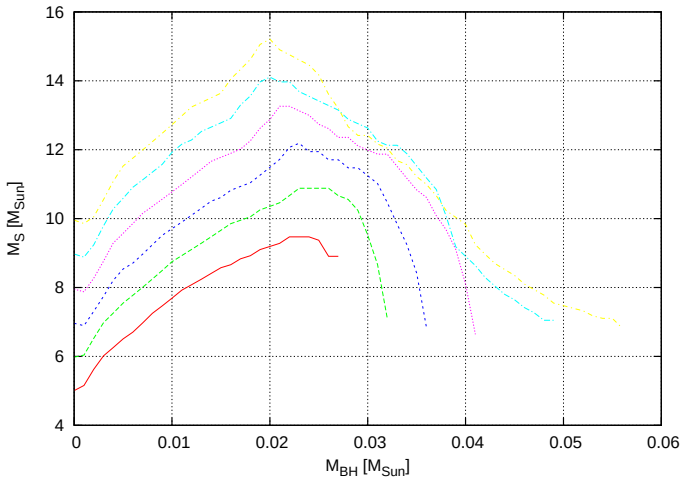

Figure 3.1: Since the algorithm used in our stellar structure code involves fixed radii, the mass of each model of star must vary with the increasing mass of the central black hole to find a new stable solution; from bottom to top: initial M_s = 5, 6, 7, 8, 9 and 10 $M_{\odot}$.

The raw results we get from our simulations are therefore valid for a fixed radius but with varying masses. In Section 3.1, such a set of results will be presented and commented. However, in order to satisfy our astrophysical interests and make more sense in terms of stellar model building, we propose to compile various sets so that we can better apprehend the true influence of an increasing black hole inside a star of constant mass (see Section 3.2).

3.1 Results for a 20 $M_\odot$ Star with Constant Radius

The choice of a 20 $M_\odot$ star follows the considerations proposed in the Introduction and the feeling we got after a few series of tries. Our stellar code underwent some corrections and improvements throughout its application for different cases and the results we show here were produced by its very last version.
The main changes and additions made to the program described in Sections 2.3 and 2.4 are:

- We force the density to always decrease when doing the outwards integration; this condition is indeed essential in order to ensure the stability of the model;
- Negative central and minimal densities are not explicitly treated as impossible, but their related error equals the definitly excluding value of 100;
- In order to guarantee as much as possible the continuity of the convection criterion (see Subsection 2.1.1), the gap between its inwards and outwards values is included in the error calculation.

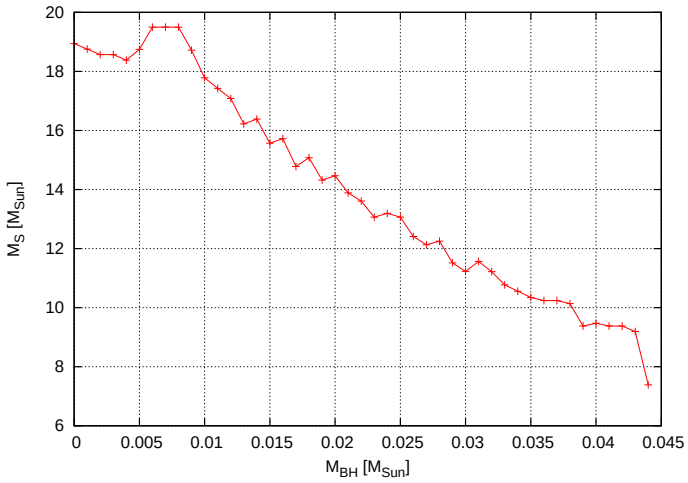

Figure 3.2: The initial mass of the star considered here is about 20 $M_\odot$; then it decreases as the mass of the accreting black hole becomes more important. When the latter reaches 0.044 $M_\odot$ in this case, no more stable solution can be found for the given conditions.

After these few modifications and some other adjustments, we performed several sets of simulations for a model star whose initial mass (i.e. without any black hole in its centre) is about 20 $M_\odot$ and whose radius is 45.56×10^8 m, that is 6.55 $R_\odot$. The step chosen for the increase of the black hole is only $10^{-3}\, M_\odot$ and Fig. 3.2 shows the change in stellar mass with regards to this slow variation.

As we saw in Section 2.2, the presence of the black hole implies significant changes in the initial conditions in terms of mass and luminosity. The consequences are clearly visible: the starting points for mass and luminosity are

directly shifted upwards, and the pressure and temperature undergo a dramatic drop during the first few steps of the outwards integration (detail in Fig. 3.3). This forces the matching process to increase the initial values as well in order to find a new stable solution.

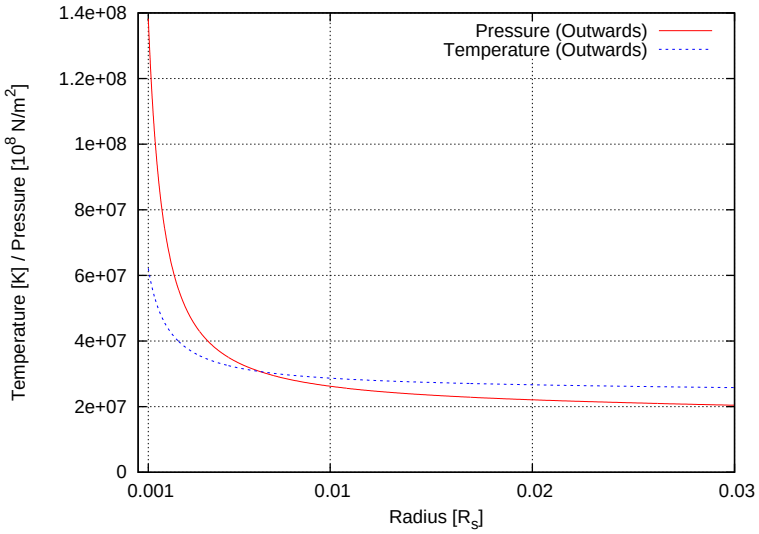

Figure 3.3: Detail of the central zone for pressure and temperature where the sheer slopes may be seen for both parameters.

As a matter of fact, both graphs presented here almost correspond to the *breaking point* beyond which no more satisfactory models can be found. This boundary in the black hole mass is apparently due to the growing gaps that appear in the mass and luminosity profiles. In the present case (using $l = 10^{-1}$ and $\dot{m} = 10^2$), the breaking point is situated at a mass of 0.044 $M_\odot$ for the black hole, assuming a maximal error of $err = 0.3$ (Eq. 2.34).

Following the considerations in [40], we test various combinations of $(l, \dot{m})$ and compare the behaviours of the main physical parameters. Our idea - and secret hope - is that the accretion rate could be large enough to balance the increase of M in Eq. (2.22) so that the drops in pressure and temperature could be reduced, ultimately allowing solutions for bigger black holes. Taking $(l, \dot{m}) = (1, 1)$, the values we actually use in our model are:

$$L_{BH} = 5.03 \times 10^{29} \text{ W and}$$

$$\dot{M}_{BH} = 5.60 \times 10^{12} \text{ kg s}^{-1}.$$

The solution which was found for this configuration ($R_s = 6.55\ R_\odot$ and $M_{BH} = 0.04\ M_\odot$) has a final stellar mass of 9.47 $M_\odot$ and a total luminosity of 2.66×10^{30} W. That means: the accretion luminosity counts for almost one fifth of the total luminosity and, assuming a stable regime, the central black hole would not have enough time - by far - to suck all the stellar material within the lifetime of the star.

These two observations make us think that it should be possible to find combinations of $(l, \dot{m})$ with accretion rates large enough to compensate the increase

in central mass and luminosity, and still not too large so that the majority of the stellar material would not be sucked before a few tens of millions years. This very special zone in the $(l, \dot{m})$ plane would thus correspond to stars able to achieve the scenarii described in Section 1.5.

We endeavour to increase the mass of the accreting black hole as much as we can because we would like to reach the region of a few solar masses where black holes can theoretically form from stellar collapse. However, other possibilities ought to be studied, e.g. the role of primordial black holes [42] around the Galactic Centre. According to [43, 44], the range of masses between 10^{12} and 10^{22} kg may contain smaller black holes that do not evaporate too quickly (through Hawking radiation) and are not necessarily detectable through microlensing. It could be worth exploring this region.

3.2 Compiling Results for a Given Stellar Mass

As explained previously, it makes rather more sense to compare situations with different black hole masses but within a star of constant mass. This is manageable by simply combining sets of results from various configurations having their own fixed radius. We choose a given mass and for each of them, we try and find the stable solution presenting the closest parameter. Fig 3.4 shows the relation of such a constant mass configuration with respect to the increase of the central black hole.

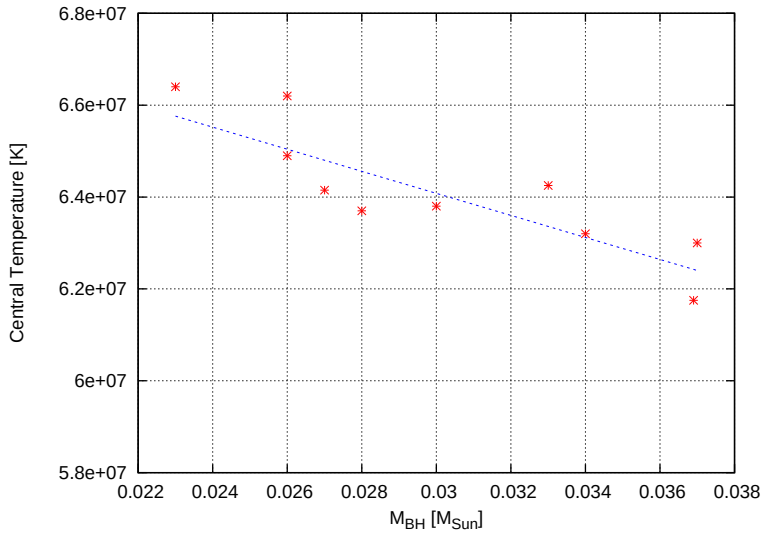

Figure 3.4: With a fixed mass $M_S = 10\ M_\odot$ instead of a fixed radius, other aspects of our research may be investigated, such as the influence of the accreting black hole on the central temperature of the star.

This part of our approach needs deeper investigation before being able to produce truly reliable results. Indeed, the process of choosing and compiling solutions has to be refined if we are concerned about avoiding computing artefacts and subjective comparisons.

3.3 Investigating $(l, \dot{m})$ Combinations with Further Refinements

Having obtained an encouraging set of results with a first version of our simulation code, we undertake to improve it and add some refinements in order to make it more realistic. Most of these refinements are related to the physical consequences of the black hole accreting material in the central regions of the star. Once we will have implemented them and evaluated their impact on the solutions, we will thoroughly explore the $(l, \dot{m})$ parameter space[1]. Our aim will then be to determine the maximal mass the nested black hole can reach and what would be its influence on its host star.

3.3.1 Taking into Account the Infall Velocity

In Subsection 2.2.1, we showed how the pressure gradient is modified by the infall velocity. The new expression for dP/dr was given by Eq. (2.22), deduced from the substitution of the dv/dr term in the expression

$$\frac{dP}{dr} = -\frac{GM\rho}{r^2} - \rho v \frac{dv}{dr}.$$

Modifying the pressure gradient was certainly a necessary step towards a more realistic model, but this might not be sufficient to describe the extreme physical interactions taking place around the central black hole. Indeed, its awesome accretion power, even for smaller values of m_{BH}, creates thermodynamic conditions which completely upset the central equilibrium of the massive star. In the case of radiative transport, we could follow a mean free path approach and determine the effective opacity of the stellar material caused by its fall into the black hole. The stellar hosts we are considering, however, present convective cores due to their extremely high central temperature. Thus we ought to translate the mean free path approach into a convective environment.

When the infalling material reaches a speed comparable to the speed of sound within its surrounding, the efficiency of the energy transport processes is dramatically suppressed. This must be taken into account in the expressions of the convective temperature gradient as well as the luminosity gradient. The radiative temperature gradient, Eq. (2.15), includes the luminosity L_r, which makes it sensitive to its changes already.

In order to model the dramatic change caused by the infall matieral, we propose to modify the gradients in question in the following way:

$$\frac{dL_r}{dr} = 4\pi r^2 \rho \epsilon \, e^{-\left(\frac{v_{infall}}{c_s}\right)^2}, \tag{3.1}$$

$$\frac{dT}{dr} = -\left(1 - \frac{1}{\gamma}\right) \frac{\mu m_H}{k_B} \frac{GM_r}{r^2} \, e^{-\left(\frac{v_{infall}}{c_s}\right)^2}, \tag{3.2}$$

where v_{infall} is the infall velocity of the stellar material

$$v_{infall} = \frac{\dot{M}}{4\pi\rho r^2}$$

[1] Let us remind the reader the $(l, \dot{m})$ are the accretion parameters in Eddington units: $l = L/L_{Edd}$ and $\dot{m} = \dot{M}/\dot{M}_{Edd}$

and c_s is the sound speed, evaluated as

$$c_s = \left(\frac{\partial P}{\partial \rho}\right)^{1/2} = \left(\frac{k_B T}{\mu m_H}\right)^{1/2}.$$

3.3.2 Variable Stellar Radius

One of the main constraints in the progression of our matching process lies in the fixed radius of the host star. For practical numerical reasons, we decided not to include the radial parameter as a free variable alongside the central pressure and temperature, total mass and luminosity of the object. This choice, however, implies certain limitations as the size of the star is not allowed to vary freely, even though such flexbility could lead towards more stable physical configurations.

Since adapting our simulation code would present difficulties such that its complete re-writing would prove easier, we resign ourselves to investigating the possible consequences of a variable radius. Starting from a known solution including a small initial black hole in a 20 $M_\odot$ star, we slightly increase its mass until no statisfactory solution can be found. At this point, we allow the radius to be either decreased (red curve in Fig. 3.5) or increased (blue curve) in order to find a better matching error. The latter is calculated following Eq. (2.34), which means that a value of $err = 10^{-2}$ corresponds to a global incertainty of about 6%, which goes down to about 2% for an error ten times smaller. Since we are refining the matching process, we require here a more constraining precision, going down from $err = 0.3$ (as in Section 3.1) to $err = 10^{-2}$.

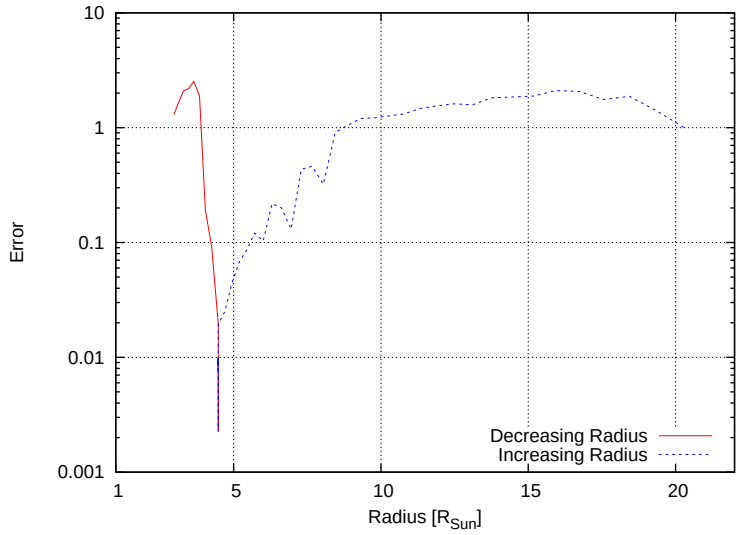

Figure 3.5: Variation of the total error for different models of host stars with accreting black hole, when the radius is allowed to decrease (*red*) or increase (*blue*), from its initial value of $R_s = 4.48\ R_\odot$, in order to find better matching solutions.

The results show that the free variation of the stellar radius does not provide more stable solutions when a critical matching point has been reached. This does not necessary mean that including a free radial parameter in the matching

process would not improve its efficiency. But such added flexibility does not seem to change the physical configuration of the black hole-star system in a favourable way.

3.3.3 Adjusting $(l, \dot{m})$ with Increasing Black Hole Masses

Besides variable radii, the most promising path of research for our study might be a better understanding of the pair $(l, \dot{m})$. This couple of parameters express the luminosity and the accretion rate in units of their Eddington limits (see Subsection 2.2.5). We already experienced how important their relative values prove to be when considering hydrodynamic accretion onto black holes. Our intention is now to further investigate the $(l, \dot{m})$ plane with increasing values for the black hole mass, in order to see whether a black hole of a few solar masses could be successfully nested within a massive star.

Before investigating the $(l, \dot{m})$ plane, it is worth explaining in some detail why we are interested in varying these parameters in the first place. Following the first set of results described in Section 3.1, we came to the conclusion that the increase in central pressure and temperature caused the matching process to stop for m_{BH} equivalent to a few percent of a solar mass. The calculated error could not be reduced to the desired upper limit ($err < 0.01$) because the internal physical configuration was creating a large discrepency in L with respect to the inward integration. It is this battle between (P, T) and L which led to a breaking point around $m_{BH} \approx 0.04\ M_{\odot}$. Fig. 3.6 shows the increase in P and T with respect to the mass of the black hole. Up until $m_{BH} = 0.03$, satisfactory solutions can be found, as the star manages to balance the accretion effects by adapting its internal equilibrium, without departing too much from its external layers. Beyond this point, however, it becomes ever harder for it to cope with the increasing mass and luminosity brought by the black hole, until the gap between outward and inward integrations becomes too wide (Fig. 3.7).

To get a better grasp of how $(l, \dot{m})$ influences the matching process for non-zero black hole masses, we ought to study in some detail the effects caused by their variation. This means that we have to determine how the main physical parameters evolve when increasing or decreasing the luminosity of the black hole or its accretion rate. Starting from a known solution with $m_{BH} = 0.001\ M_{\odot}$, we vary each parameter independently and record the observed behaviour for the central pressure and temperature (Table 5.1).

These results seem to indicate that one should be able to find $(l, \dot{m})$ regimes where the effects on P and T caused by larger m_{BH} are lessened by the those caused by a larger accretion rate and/or dimmer luminosity. Hoping to find these special regimes, we set up to investigate the corresponding parameter space following various methods, among which:

1. Increasing m_{BH} until the matching process reaches its breaking point; we then vary either l or $\dot{m}$ independently until a satisfactory solution is found for the given value of m_{BH} ; we repeat this operation until no more solutions can be discovered, even for extreme values of $(l, \dot{m})$;

2. Increasing m_{BH} in the same way, but alternating variations in l and $\dot{m}$ until $err < 0.01$ again; stopping when reaching the same critical point as for the first method;

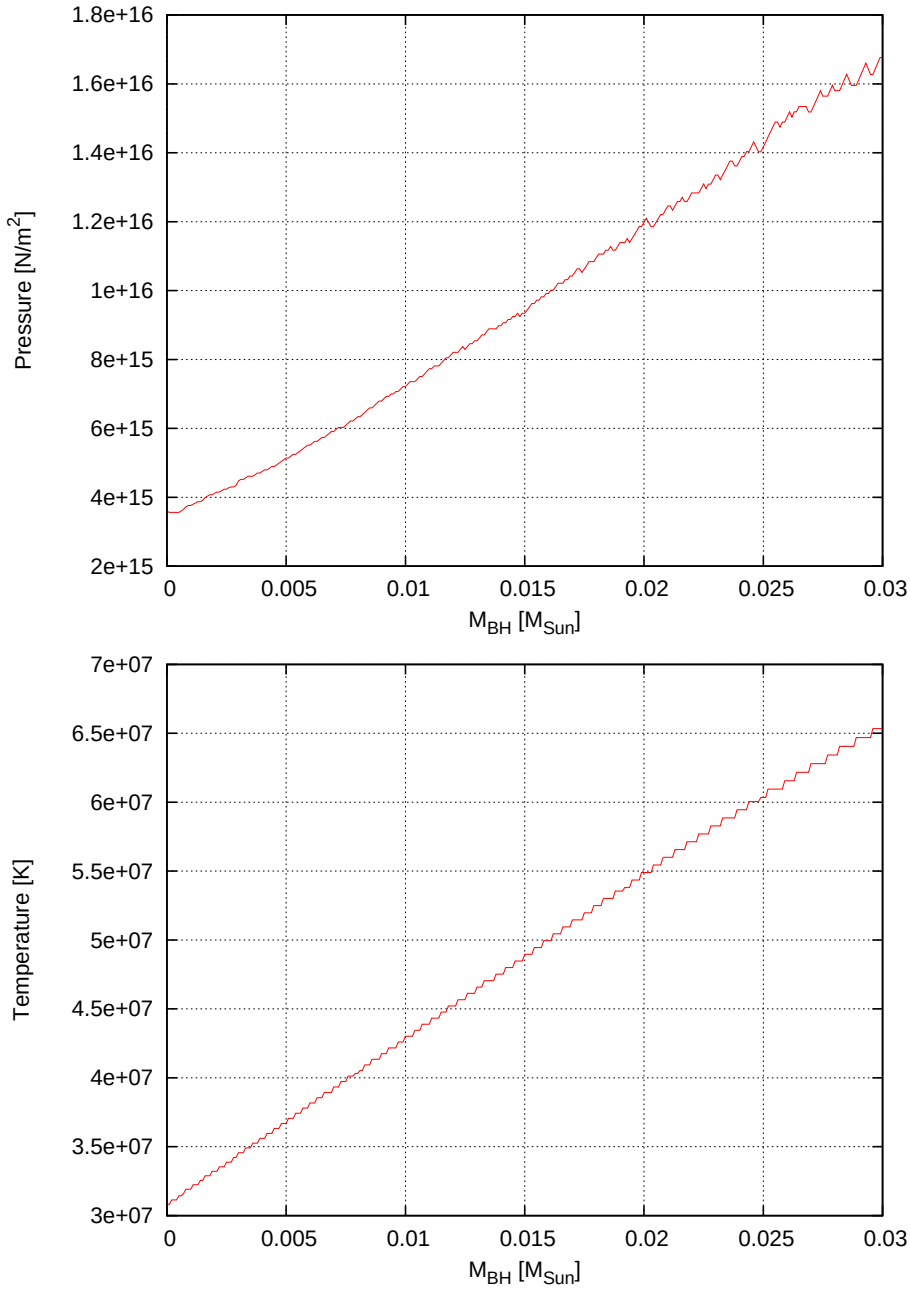

Figure 3.6: Increasing central pressure (above) and central temperature (below) for an increasing black hole mass, until $m_{BH} = 0.03\ M_{\odot}$. The increase in these physical parameters causes the matching process to stop (reasons explained in the text).

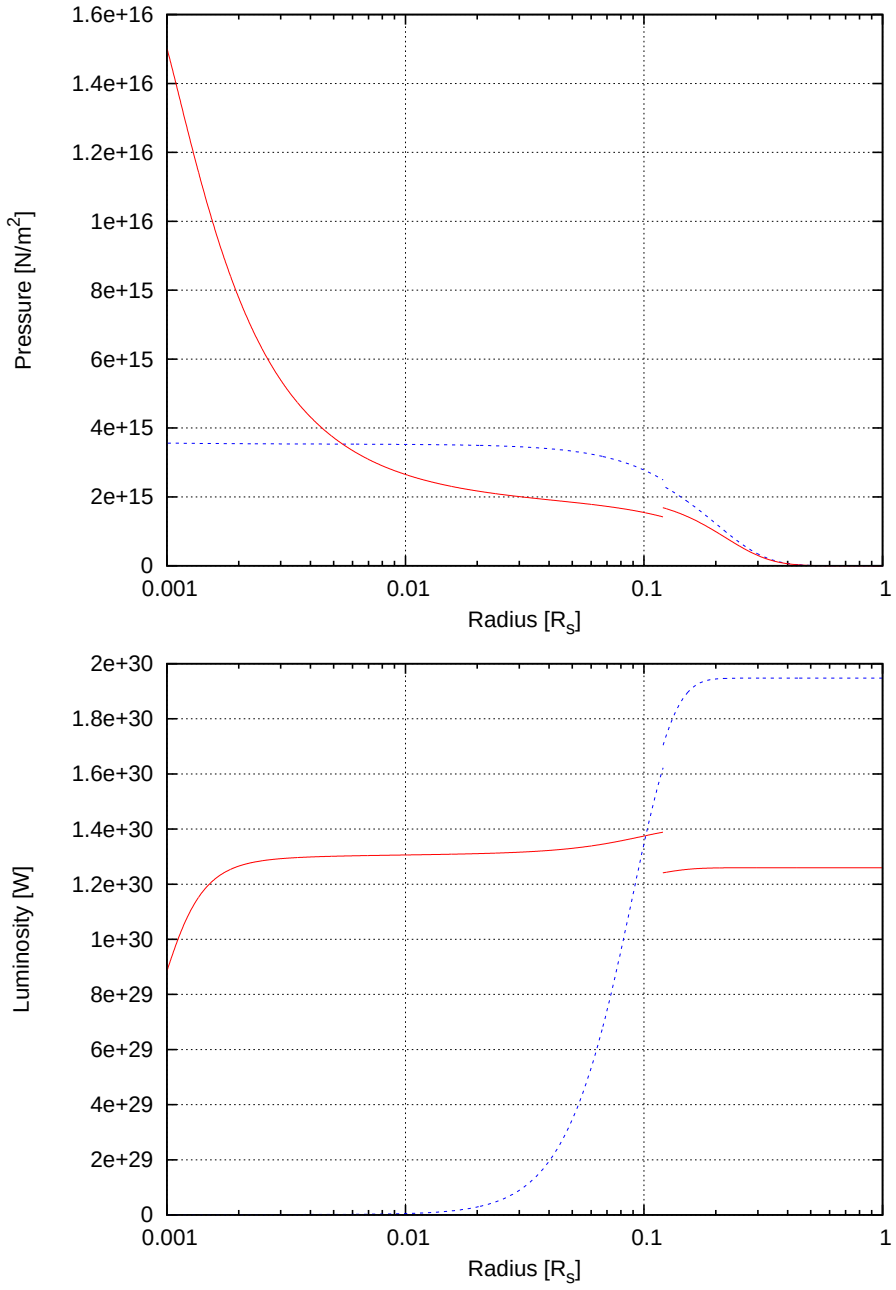

Figure 3.7: Pressure and luminosity profiles for $m_{BH} = 0.0001\ M_\odot$ (*blue*) and $m_{BH} = 0.04\ M_\odot$ (*red*), with $(l, \dot{m}) = (1, 1)$. We are here beyond the *breaking point* ($err \simeq 0.05$) which is a consequence of the increase in central P and T, causing the outward luminosity and density to drift away from their inward values.

Effects Caused on P and T			
Parameter	Variation	Effect on P	Effect on T
m_{BH}	Increase	$\nearrow$	$\nearrow$
	Deacrease	$\searrow$	$\searrow$
$\dot{M}_{BH}$	Increase	$\rightarrow$ or $\searrow$	$\rightarrow$ or $\searrow$
	Decrease	$\rightarrow$ or $\nearrow$	$\rightarrow$ or $\nearrow$
L_{BH}	Increase	-	-
	Decrease	$\searrow$	$\nearrow$

Table 3.1: Observed effects of independently varying m_{BH}, $\dot{M}_{BH}$ and L_{BH}. Allowing l to vary freely changes the effect caused by the variation of $\dot{M}_{BH}$ (second effects shown on the second row), in a way that might compensate the impact of the increasing black hole mass. The simulations with increasing L_{BH} were discarded as non satisfactory.

3. Always increasing the mass of the black hole and varying l and $\dot{m}$ simultaneously until reaching the same critical point;

4. Starting from a known breaking point for a given m_{BH}, varying either l or $\dot{m}$ until the error cannot be reduced anymore, then varying the other parameter until $err < 0.01$; resuming the variation of the first parameter, and repeating this cycle until no more solutions can be found.

These methods had to be developed as it was not possible to include the parameters $(l, \dot{m})$ in the matching process itself without re-writing the entire code.

The variety of results that we obtained following these different approaches shows a consistent pattern: lower l and increasing $\dot{m}$ allows to widen the range of possible black hole masses, but not indefinitely. The effect of the infalling material on the various gradients takes place on rather short distances, compared to the impact of the added mass term m_{BH} and the extra luminosity L_{BH}. The infall velocity is orders of magnitude smaller than the sound speed in general, and very large values of $\dot{m}$ are needed in order to level them. It results from this situation that extremely high accretion rates are required to compensate the black holes effects beyond a few $10^{-2}\ M_{\odot}$. The necessary increase in $\dot{m}$ is actually so dramatic that it quickly reaches non sustainable values for the host star, going beyond a few solar masses per year!

The presence of the central black hole generates very steep gradients for most physical parameters close to the centre of the star. This implies that the matching results strongly depend on the initial radius of integration R_{min}: higher m_{BH} can thus be obtained when starting further away from the event horizon of the black hole. With a value of $R_{min} = 10^{-3}\ R_s$, a mass of $m_{BH} = 0.0367\ M_{\odot}$ can be reached with reasonable values of $(l, \dot{m}) = (0.03, 10^5)$ (see Fig. 3.8 and 3.9). This corresponds to the critical point, as a slight increase of $10^{-4}\ M_{\odot}$ makes the stellar equilibrium tip over the edge. For $m_{BH} = 0.0368\ M_{\odot}$, the accretion parameters must adopt the values of $(l, \dot{m}) = (10^{-3}, 10^{10})$ in order to produce a satisfactory error. This huge accretion rate would correspond to $\dot{M}_{BH} \simeq 8 \times 10^{-4}\ M_{\odot}$, which means that the host star would be sucked in by its nested black hole in a few tens of thousands of years.

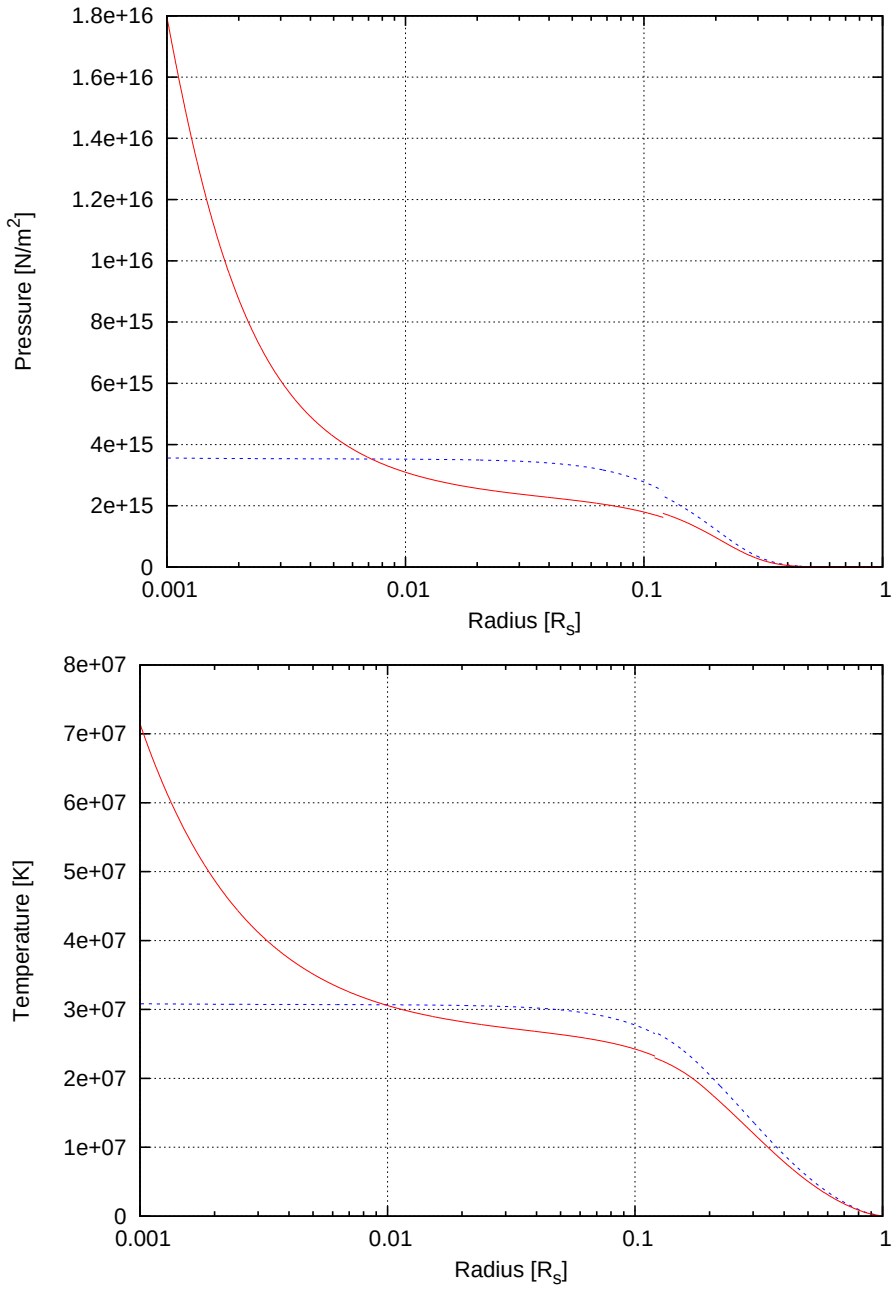

Figure 3.8: Pressure and temperature profiles of a massive star (final mass $M_s = 8.8\ M_\odot$) hosting a black hole of mass $m_{BH} = 10^{-4}\ M_\odot$ and $m_{BH} = 0.0367\ M_\odot$ respectively. The sharp increase in the central values can clearly be seen, but the star manages to balance the accretion effects so that the global error falls below the required precision. The accretion parameters are $(l, \dot{m}) = (0.03, 10^5)$.

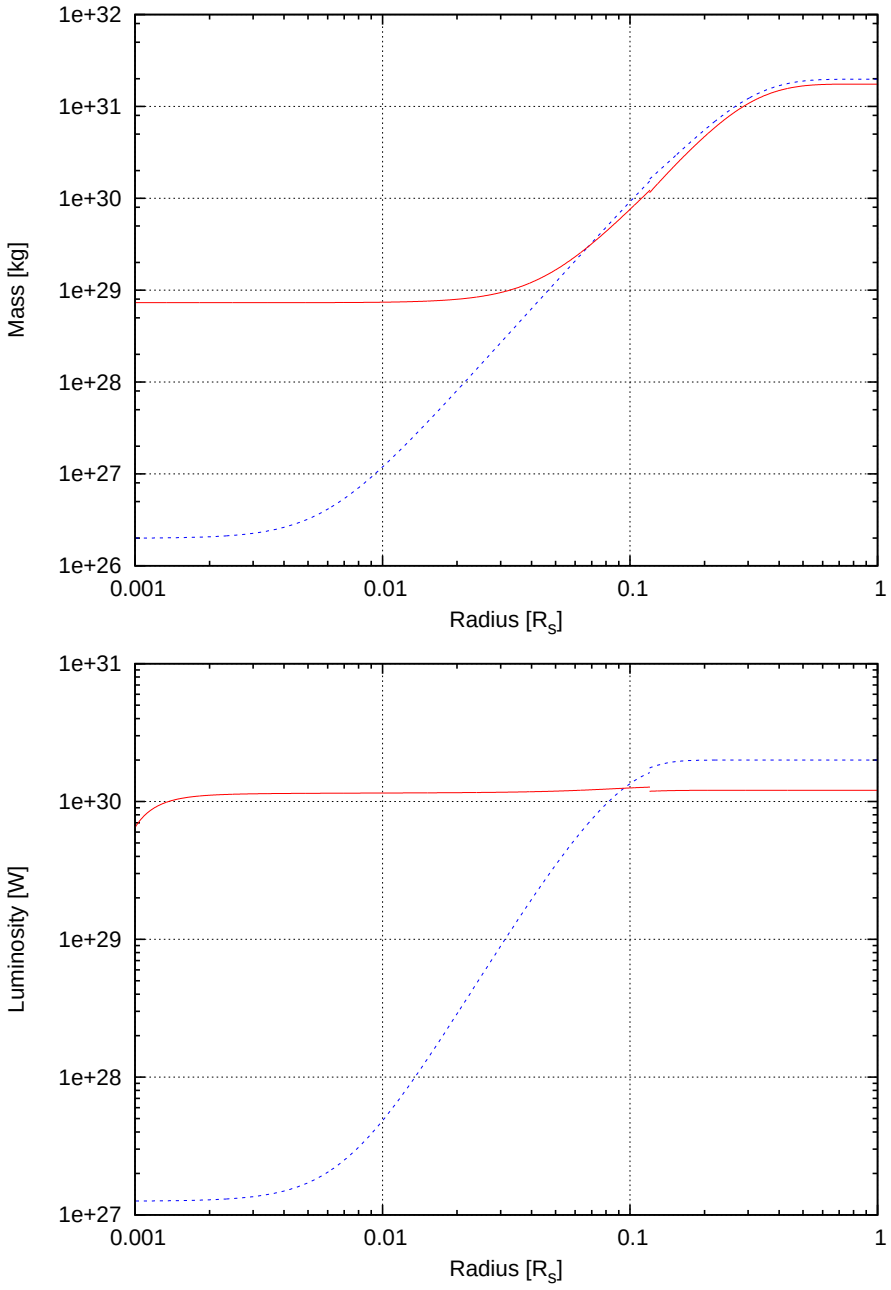

Figure 3.9: Mass and luminosity profiles of a massive star (final mass $M_s = 8.8\ M_\odot$) hosting a black hole of mass $m_{BH} = 10^{-4}\ M_\odot$ and $m_{BH} = 0.0367\ M_\odot$ respectively. The impact of the added mass of the black hole marks a clear discrepency between the two profiles, as does the accretion luminosity generated by its presence. The accretion parameters are $(l, \dot{m}) = (0.03, 10^5)$.

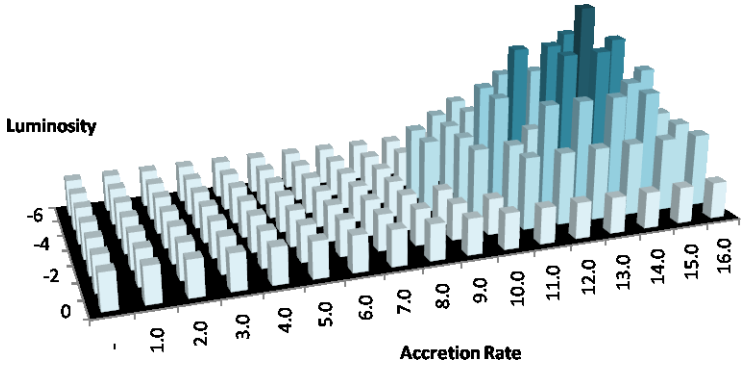

Figure 3.10: Allowed accretion parameters on the $(l, \dot{m})$ parameter space, showing that the range of available options (with $err < 0.01$) shrinks down to only one small area with unsustainable conditions. The axes are expressed in logarithmic values $(\log_{10}(\dot{m}), \log_{10}(l))$ The white-blue bars stand for $m_{BH} = 0.036\ M_\odot$, then a denser blue corresponds to a higher black hole mass: $m_{BH} = 0.0368$ to $0.0371\ M_\odot$ respectively.

It can be shown that extreme values of $(l, \dot{m})$ are needed when the black hole mass passes a certain limit. Indeed, when increasing m_{BH}, the surface of the allowed accretion parameters shrinks until only one point remains. Since this point, in our case, is situated in regions of the parameter space where the accretion conditions would not leave the star undisturbed for long enough (Fig. 3.10), we conclude that the maximal m_{BH} has been reached.

Besides these unsustainable conditions for the star, other physical issues arise when considering an increasingly large accretion rate. When the latter goes beyond $\dot{m} \approx 10^{15}$, the pressure and temperature profiles create large central values for the stellar density, which in turn causes the infall velocity to increase significantly. These conditions provoke a plunge in temperature in the internal layers of the star, which prevent the matching process from finding stable solutions. Similar circumstances have been observed within different paradigms; the black hole mass cannot be increased beyond a certain value, usually a few percent of the solar mass, because of a faulty behaviour of the temperature profile caused by extreme physical conditions close to the accretion zone.

3.4 Summary of Our Results

To sum up, here are the main points of this first part of our research on accreting black holes inside stellar interiors:

- We managed to create realistic stellar models and to find stable solutions when we put an accreting black hole in their centre;
- With the best combinations of $(l, \dot{m}) = (0.1, 10^2)$, the mass of the central black hole can be increased up to $0.044\ M_\odot$ for a $20\ M_\odot$ star, assuming a maximal imprecision of $err = 0.3$. In such cases, the accretion luminosity due to the black hole represents less than one fifth of the total luminosity and the accretion rate times the lifetime of the star is small compared to the total mass;

- With a refined matching process taking into account the effects caused by the infalling material, one is able to improve significantly the required precision up to the percent level ($err = 0.01$). The highest possible black hole mass for a 10 $M_\odot$star lies around the same limit, at $m_{BH} = 0.04\ M_\odot$. This result is obtained with accretion parameters $(l, \dot{m}) = (0.03, 10^{-5})$, which still allow sustainable conditions for the hosting star. For $m_{BH} = 0.035\ M_\odot$, a maximal luminosity of $L_{BH} \approx \frac{1}{3} L_\star$ is atteined, which is still much too small to statisfy the scenarii proposed in Section 1.5
  Results are similar for larger stars, up until about 20 $M_\odot$. The main matching issues arise at the centre of the stellar interior, and the physical conditions in the outer layers influence the process only marginally.

- According to our understanding of the physical processes and our numerical results, we believe that our approach has reached a consistent physical barrier. The mass of the hosted black hole cannot be increased beyond a few percent of a solar mass without requiring life-threatening accretion conditions for the star.

As mentionned throughout the present Chapter, the main issues we have raised are basically related to the control of the pressure and temperature gradients thanks to appropriate combinations of $(l, \dot{m})$. The configurations we have been studying do not seem to bring the expected solutions, but interesting alternatives have been investigated and further research should be undertaken. These points will be briefly discussed in the next Chapter of conclusions.

Chapter 4

Conclusions

4.1 Conclusive Remarks

In this first part of our research, we have been studying accreting black holes nested inside massive stars. Our intention was to investigate a possible alternative explanation for the Paradox of Youth by studying the effects of such an accretion on the burning processes of these stars. The paradox arises from the observation of very young, massive stars at relatively short distances from the centre of our galaxy. According to our understanding of stellar formation and evolution, these B-type stars should not be able to form in the surroundings of the central Super Massive Black Hole, because the tremedous tidal forces it generates would prevent any gas cloud to gravitationally collapse into a protostar. Moreover, given their assumed youth, they should not have had time to travel to this position from more external galactic regions.

However, the latter assumption on their deduced age made us realise that an appropriate change in their luminosity generation processes could provide us with an interesting track towards solving the Paradox of Youth. Our idea was that an embedded black hole, accreting stellar material and emitting part of the total luminosity, would offer a chance to the star of sparing its fuel while keeping its external appearance.

We have shown that it was indeed physically possible to include a small black hole in the centre of a massive star, while preserving the hydro-dynamical equilibrium of the stellar interior. By progessively increasing the mass of the imbedded black hole, we discovered that the extreme accretion conditions prevent the system from finding stable solutions beyond a given value of $m_{BH} \approx 0.04\, M_{\odot}$. In the optimal cases, the maximal accretion luminosity generated by the black hole represents about one third of the total luminosity. Besides the fact that such a black hole could not theoretically be formed from gravitational collapse, the relative gain in luminosity would not allow the massive to travel over much longer galactic distances.

We therefore conclude that including black holes in the centre of massive stars does not provide solutions stable enough to allow sensibly longer inwards journeys from larger galactic distances, which could explain their paradoxical observation in the tremendous tidal field of the central SMBH.

4.2 Further Research and Perspectives

The search for a plausible explanation to the Paradox of Youth has brought people to think about stellar evolution and galactic dynamics in a new, creative way. Our approach did not produce the expected answers, but new tracks have been open and further research should be built on the acquired knowledge.

The method we followed in our investigation was but one particular angle of the problem. Starting from stable stellar solutions, we endeavoured to place an increasingly massive black hole in the centre of the system. Other approaches should be considered, however, specially if one attempts to simulate newborn massive stars created by stellar remnants accreting interstellar gas. Further theoretical considerations are also needed concerning the possible existence of small black holes, with $m_{BH} < M_{\odot}$ and their interaction with galactic objects.

We believe that there is still room for promising research on interactions between black holes and massive stars, which might lead to the discovery of an explanation for the Paradox of Youth.

After considering accreting black holes inside stellar interiors, we will move to slightly less dense objects and study the accretion that occurs onto neutron stars. Our main objective, in the second part of this thesis, will be to analyse the capture of Dark Matter onto such stars. Based on previous work [45, 57], we indeed believe that these objects can be used to set constaints on its parameter space and give us clues about the properties of Dark Matter particles. We will develop the necessary analytical tools and, using some of the techniques implemented so far, we will build numerical models in order to study the fate of such configurations and look for observable consequences.

Bibliography

[1] C. J. Hanser, S. D. Kawaler, and V. Trimble, *Stellar Interiors: Physical Principles, Structure and Evolution*. 2nd ed., 2004.

[2] B. W. Carroll and D. A. Ostlie, *An Introduction to Modern Astrophysics*. 2nd (international) ed., 2007.

[3] A. J. Cannon and E. C. Pickering, "Classification of 1,688 southern stars by means of their spectra," *Annals of Harvard College Observatory*, vol. 56, pp. 115–164, 1912.

[4] J. Michell, "O the Means of Discovering the Distance, Magnitude, &c. of the Fixed Stars, in Consequence of the Diminution of the Velocity of Their Light, in Case Such a Diminution Should be Found to Take Place in any of Them, and Such Other Data Should be Procured from Observations, as Would be Farther Necessary for That Purpose. by the Rev. John Michell, B. D. F. R. S. I a Letter to Henry Cavendish, Esq. F. R. S. and a. S.," *Royal Society of London Philosophical Transactions Series I*, vol. 74, pp. 35–57, 1784.

[5] K. Schwarzschild, "On the Gravitational Field of a Mass Point According to Einstein's Theory," *Abh. Konigl. Preuss. Akad. Wissenschaften Jahre 1906,92, Berlin,1907*, pp. 189–196, 1916.

[6] R. Schoedel, A. Eckart, C. Iserlohe, R. Genzel, and T. Ott, "A Black Hole in the Galactic Center Complex IRS 13E?," 2005. cite arxiv:astro-ph/0504474.

[7] A. M. Ghez, G. Duchene, K. Matthews, S. D. Hornstein, A. Tanner, J. Larkin, M. Morris, E. E. Becklin, S. Salim, T. Kremenek, D. Thompson, B. T. Soifer, G. Neugebauer, and I. McLean, "The First Measurement of Spectral Lines in a Short-Period Star Bound to the Galaxy's Central Black Hole: A Paradox of Youth," 2003. cite arxiv:astro-ph/0302299.

[8] Y. Levin and A. M. Beloborodov, "Stellar disk in the Galactic Center – a remnant of a dense accretion disk?," 2003. cite arxiv:astro-ph/0303436.

[9] R. Genzel, C. Pichon, A. Eckart, O. E. Gerhard, and T. Ott, "Stellar Dynamics in the Galactic Centre: Proper Motions and Anisotropy," 2000. cite arxiv:astro-ph/0001428.

[10] P. Artymowicz, D. N. C. Lin, and E. J. Wampler, "Star trapping and metallicity enrichment in quasars and active galactic nuclei," *ApJ*, vol. 409, pp. 592–603, June 1993.

[11] J. R. Lu, A. M. Ghez, S. D. Hornstein, M. Morris, and E. E. Becklin, "IRS 16SW - A New Comoving Group of Young Stars in the Central Parsec of the Milky Way," 2005. cite arxiv:astro-ph/0504276.

[12] O. Gerhard, "The Galactic Center He I Stars: Remains of a Dissolved Young Cluster?," 2000. cite arxiv:astro-ph/0005096.

[13] S. S. Kim and M. Morris, "Dynamical Friction on Star Clusters near the Galactic Center," 2003. cite arxiv:astro-ph/0307271.

[14] M. Morris, "Massive star formation near the Galactic Center and the fate of the stellar remnants," *ApJ*, vol. 408, pp. 496–506, May 1993.

[15] M. P. Muno, F. E. Bauer, R. M. Bandyopadhyay, and Q. D. Wang, "A Chandra Catalog of X-ray Sources in the Central 150 pc of the Galaxy," 2006. [arxiv:astro-ph/0601627].

[16] A. R. King, D. J. Raine, and J. Frank, *Accretion Power in Astrophysics*. 2nd ed., 1992.

[17] H. Bondi, "On spherically symmetrical accretion," *MNRAS*, vol. 112, pp. 195–+, 1952.

[18] K. M. Chang and J. P. Ostriker, "Standing shocks in accretion flows onto black holes," *ApJ*, vol. 288, pp. 428–437, January 1985.

[19] L. Titarchuk, A. Mastichiadis, and N. D. Kylafis, "Spherical accretion onto neutron stars and black holes," 1996.

[20] S. Silich, G. Tenorio-Tagle, and F. Hueyotl-Zahuantitla, "Spherically-symmetric Accretion onto a Black Hole at the Center of a Young Stellar Cluster," 2008.

[21] L. Mestel, "The influence of stellar radiation on the rate of accretion," *MNRAS*, vol. 114, pp. 437–+, 1954.

[22] R. C. Cannon, "Massive Thorne-Zytkow Objects - Structure and Nucleosynthesis," *MNRAS*, vol. 263, pp. 817–+, August 1993.

[23] R. Edgar, "A review of Bondi-Hoyle-Lyttleton accretion," *New Astronomy Review*, vol. 48, pp. 843–859, September 2004.

[24] F. Hoyle and R. A. Lyttleton, "The effect of interstellar matter on climatic variation," in *Proceedings of the Cambridge Philosophical Society*, vol. 35 of *Proceedings of the Cambridge Philosophical Society*, pp. 405–+, 1939.

[25] F. Hoyle and R. A. Lyttleton, "On the accretion of interstellar matter by stars," *Mathematical Proceedings of the Cambridge Philosophical Society*, vol. 36, pp. 325–+, 1940.

[26] F. Hoyle and R. A. Lyttleton, "On the physical aspects of accretion by stars," *Mathematical Proceedings of the Cambridge Philosophical Society*, vol. 36, pp. 424–+, 1940.

[27] H. Bondi and F. Hoyle, "On the mechanism of accretion by stars," *MNRAS*, vol. 104, pp. 273–+, 1944.

[28] D. L. Gilden and J. C. Wheeler, "Time-dependent, optically thick accretion onto a black hole," *ApJ*, vol. 239, pp. 705–711, July 1980.

[29] R. A. Flammang, "Stationary spherical accretion into black holes. II - Theory of optically thick accretion," *MNRAS*, vol. 199, pp. 833–867, June 1982.

[30] P. Vitello, "Optically thick, time-dependent spherical accretion onto a black hole. I - Equations and numerical methods," *ApJ*, vol. 284, pp. 394–406, September 1984.

[31] C. Bambi, D. Spolyar, A. D. Dolgov, K. Freese, and M. Volonteri, "Implications of primordial black holes on the first stars and the origin of the super–massive black holes," 2008. cite arxiv:0812.0585.

[32] J. A. Regan and M. G. Haehnelt, "Pathways to massive black holes and compact star clusters in pre-galactic dark matter haloes with virial temperatures $>$ 10000k," 2008. cite arxiv:0810.2802.

[33] K. S. Thorne and A. N. Zytkow, "Stars with degenerate neutron cores. I - Structure of equilibrium models," *ApJ*, vol. 212, pp. 832–858, March 1977.

[34] C. Eich, M. E. Zimmermann, K. S. Thorne, and A. N. Zytkow, "Giant and supergiant stars with degenerate neutron cores," *ApJ*, vol. 346, pp. 277–283, November 1989.

[35] R. C. Cannon, P. P. Eggleton, A. N. Zytkow, and P. Podsiadlowski, "The structure and evolution of Thorne-Zytkow objects," *ApJ*, vol. 386, pp. 206–214, February 1992.

[36] M. C. Begelman, E. M. Rossi, and P. J. Armitage, "Quasistars: Accreting black holes inside massive envelopes," 2007.

[37] A. Gruzinov, "The Rate of Turbulent Spherical Accretion," 1998. cite arxiv:astro-ph/9809265.

[38] R. D. Blandford and M. C. Begelman, "On the Fate of Gas Accreting at a Low Rate onto a Black Hole," 1998. cite arxiv:astro-ph/9809083.

[39] E. Quataert and A. Gruzinov, "Convection-Dominated Accretion Flows," 1999. cite arxiv:astro-ph/9912440.

[40] M.-G. Park and J. P. Ostriker, "Hydrodynamics of Accretion onto Black Holes," 1998. cite arxiv:astro-ph/9811048.

[41] L. Nobili, R. Turolla, and L. Zampieri, "Spherical accretion onto black holes - A complete analysis of stationary solutions," *ApJ*, vol. 383, pp. 250–262, December 1991.

[42] A. Drake, "Primordial Black Holes and Structure Formation," *APS Meeting Abstracts*, pp. 1004P–+, October 2006.

[43] M. A. Abramowicz, J. K. Becker, P. L. Biermann, A. Garzilli, F. Johansson, and L. Qian, "No observational constraints from hypothetical collisions of hypothetical dark halo primordial black holes with galactic objects," 2008. cite arxiv:0810.3140.

[44] J. K. Becker, M. A. Abramowicz, and P. L. Biermann, "On the detectability of primordial black holes in the Galaxy," 2009. cite arxiv:0905.3078.

[45] G. Bertone and M. Fairbairn, "Compact Stars as Dark Matter Probes," 2007. cite arxiv:0709.1485.

[46] C. Kouvaris, "Wimp annihilation and cooling of neutron stars," 2007. cite arxiv:0708.2362.

Part II

Neutron Stars as Dark Matter Probes

Chapter 5

Introduction

In our current understanding of the Universe, non neagligible parts remain obscure despite all scientific endeavours to cast light on them. The most significant of them bear rather revealing names: Dark Matter and Dark Energy. Although being the main components of the energy density in the Universe, these dark entities have been bewildering researchers for decades without any substantial sign of giving away their secrets.

In this part of our thesis, we will focus our attention on Dark Matter (DM), whereas the last part will deal with alternative models to Dark Energy. Our intention is to evaluate the pertinence of a new astrophysical indirect detection method for Dark Matter. We plan to use a particular type of astrophysical objects, namely neutron stars, to capture DM and hopefully learn something about it by looking at the observable consequences of its capture. After setting the general background in this introduction, we present analytical considerations in Chapter 6. The results are then distributed in Sections 7.1 and 7.2 depending on the assumed nature of DM. Conclusions follow in the final Chapter 8.

5.1 Cosmological Background

The historical and scientific context in which we develop our argumentation presents several features which we find useful to detail here.

We believe that we live in an expanding Universe which started with a space-time singularity called the "Big Bang" and that its evolution is best described by the so-called *Standard Cosmological Model*, which we briefly summarise below. Dark Matter is an essential component of this model; in Subsection 5.1.3, we present the particular type of DM we will be considering.

5.1.1 Standard Cosmological Model

A large amount of combined works has been necessary to reach the consensual theoretical model known as the Standard Cosmological Model (e.g. [1, 2, 3]). Replacing the Steady State theory [4, 5], it is now widely accepted as the simplest cosmological model which is in general agreement with observational data. Its appealing apparence comes from this very simplicity and from the fact that it provides a plausible explanation to several cosmological questions: large scale

structures in the Universe, shape and origin of the Cosmic Microwave Background (CMB) radiation, abundances of light elements, accelerated expansion of the Universe, etc.

Arguably the most significant characteristics of the Standard Cosmological Model result from the Copernican principle which states that the location of the observer cannot be considered as special in any way: on large enough scale, our Universe is isotropic and homogeneous. The model is based on the Friedmann-Lemaître-Robertson-Walker (FLRW) metric

$$ds^2 = -c^2dt^2 + a(t)^2\left(\frac{dr^2}{1-kr^2} + r^2\left(d\theta^2 + sin^2\theta d\phi^2\right)\right), \tag{5.1}$$

which is an exact solution of Einstein's field equations of General Relativity

$$R_{\mu\nu} - \frac{1}{2}Rg_{\mu\nu} + \Lambda g_{\mu\nu} = \frac{8\pi G}{c^4}T_{\mu\nu}. \tag{5.2}$$

The model describes the evolution of the observable Universe with the Friedmann equations

$$H^2 = \left(\frac{\dot{a}}{a}\right)^2 = \frac{8\pi G}{3}\rho - \frac{kc^2}{a^2} + \frac{\Lambda c^2}{3}, \tag{5.3}$$

$$\frac{\ddot{a}}{a} = -\frac{4\pi G}{3}\left(\rho + \frac{3p}{c^2}\right) + \frac{\Lambda c^2}{3}. \tag{5.4}$$

A flat geometry is assumed, which means that $k = 0$ in the previous Eq. (5.1) and (5.3). In these conditions, the Universe will expand forever and its expansion, through the term Λ, is accelerating. Indeed, Λ stands for the cosmological constant which is currently associated with **Dark Energy** that explains the current accelerating expansion of space against the effects of gravity. As the details concerning Dark Energy are more relevant to the third part of our research, we choose to present them in Section 9.1. Let us simply admit here that there exists, throughout the Universe, a repulsive force with negative pressure which acts on large scales by pushing apart distant objects, causing them to appear dimmer than they should.

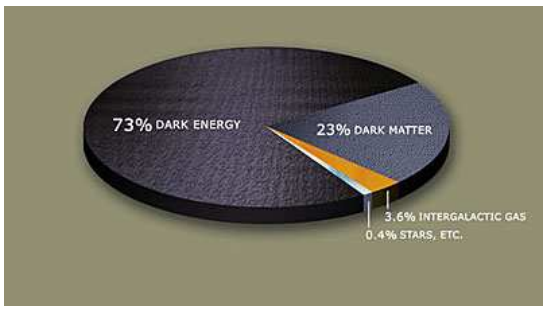

Figure 5.1: Distribution of the energy density in the Universe: Dark Energy and Dark Matter make up about 96% of the total; stars, intergalactic gas, neutrinos and heavy elements account for only 4% all together.

Dark Matter is a form of invisible matter which is detectable only through its gravitational effects. It was first postulated by Fritz Zwicky in 1933 [6] to

account for evidence of 'missing mass' in the orbital velocities of galaxies in clusters. Cosmological observation tell us that DM cannot be made of baryons [7] and that it must interact with ordinary matter rather feebly. The form of Dark Matter considered in the Standard Cosmological Model is **Cold Dark Matter** (CDM), which is a massive and non-relativistic type of DM. Besides this, it is usually described as being non-baryonic, dissipationless (no cooling by radiation photons) and collisionless. CDM is estimated to account for about 23% of the total mass-energy density in the whole Universe (noted $\Omega_{\mathrm{DM}} \approx 0.23$, with $\Omega_{\mathrm{DM}} = \rho_{\mathrm{DM}}/\rho_c$, where ρ_{DM} is the DM density and ρ_c is the critical density[1]), whereas Dark Energy would constitute no less than about 73% of it ($\Omega_\Lambda \approx 0.73$). All observable matter and energy is contained in the remaining few percent (Fig. 5.1). The Standard Cosmological Model is often refered to as ΛCDM because of its two main components.

5.1.2 Evidences for Dark Matter

There are evidences for the existence of Dark Matter at several different scales in the Universe [8]. In the following paragraphs, we will briefly discuss them in order to give the reader an idea of the degree of scientific conviction surrounding the necessity for DM.

Galactic Rotation Curves

The most famous, and arguably most convincing, evidence for the existence of DM on galactic scales is provided by the observation of the movement of stars and gas in galaxies. Back in the 1950s [9], circular velocities have been measured in order to draw the rotation curve of galaxies, i.e. the speed of their constituents with respect to their distance to the Galactic Centre.

Newtonian dynamics predicts the circular velocity to be

$$v(r) = \sqrt{\frac{GM(r)}{r}},$$

where $M(r) = 4\pi \int \rho(r) r^2 dr$, with $\rho(r)$ being the mass density profile. If we assume that visible matter is the only sort of matter present in the galaxy, then the velocities should fall like $1/\sqrt{r}$ beyond the optical disk. However, this expected spin is not observed; instead, an approximately constant value is measured at large distances from the centre. This fact implies the existence of a halo of invisible matter with mass $M(r) \propto r$ and density $\rho(r) \propto 1/r^2$.

Although there is a consensus about the shape of DM halos at large distances, it is still unclear whether DM distribution presents cuspy or smoother profiles near the central region. We further discuss this issue in Section 6.5.

Galaxy Clusters and Gravitational Lensing

Historically, the first hint for the existence of Dark Matter came from the observation of a cluster of galaxies. As mentioned previously, this was the work of Franz Zwicky back in the 1930s [6]. From measuring the velocity dispersion of galaxies in the Coma Cluster, he inferred a mass-to-light ratio of around 400 solar masses per solar luminosity, which is two orders of magnitude higher than

[1] Cf. footnote in Subsection 6.6.2.

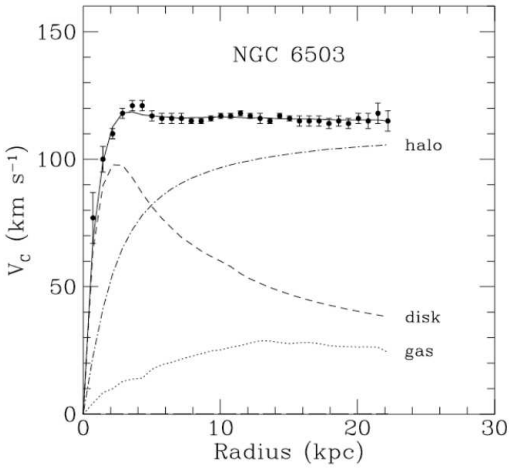

Figure 5.2: Rotation curve of the galaxy NGC 6503. The dotted lines correspond to the components mentioned on the graph [13].

in the solar neighbourhood. More recent estimates [10, 11, 12] give a consistent value of $\Omega_{\mathrm{DM}} \approx 0.2 - 0.3$ on cluster scales.

One way of measuring the mass of a cluster of galaxies relies on gravitational lensing. Thanks to Einstein's theory of General Relativity, we know that light propagates along geodesics and thus follows curved lines when passing near very heavy objects surrounded by intense gravitational fields. Distance objects situated behing a massive cluster of galaxies would have their image distorted. Analysing this distortion allows us to infer the shape of the potential well generated by the cluster and thus deduce its mass [14] (Fig. 5.3).

The Bullet Cluster

The Bullet Cluster (1E 0657-56) is arguably the most striking evidence for the existence of Dark Matter. Discovered in 1995 [15] and first observed by the Chandra X-ray Observatory in 2000, this estonishing object consists of two colliding clusters of galaxies. A detailed analysis [16] revealed that the cluster is undergoing a high-velocity merger made evident by the heated gas emitting X-ray. Because it interacts electromagnetically, the gas in both clusters is drastically slowed down, whereas most stars of their galaxies passed right through, only gravitationally slowed, effectively collisionless.

A weak lensing[2] mapping of the area, however, shows that a large though invisible part of the cluster mass has the same collisionless behaviour as the galaxies (Fig. 5.4). The authors soon identified it as Dark Matter and could benefit from the particular configuration of the cluster in order to put limits on its self-interacting cross section. The Bullet Cluster provides evidence against some of the most popular versions of Modified Newtonian Dynamics (MOND) since they predict that the lensing would be expected to follow the baryonic matter, i.e. the hot X-ray emitting gas.

[2] Weak lensing is a type of gravitational lensing which involves very subtle distortions of the background sources, requiring a statistical analysis over a large number of them. The lensing effect appears as a preferred stretching of the background objects in a particular direction.

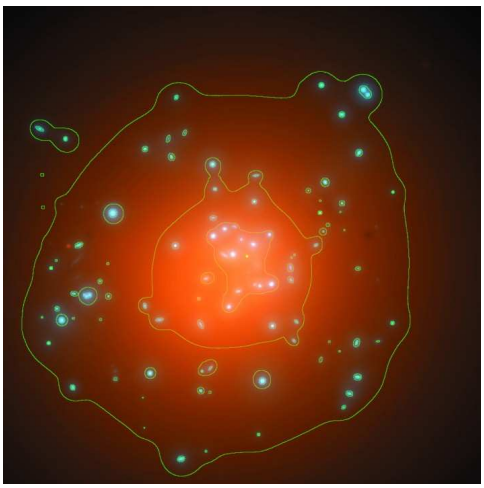

Figure 5.3: Reconstructed total mass density in the cluster CL 0024+1654 [14] based on a parametric inversion of the associated gravitational lens. DM is shown in orange; mass associated with visible galaxies in blue. If we exclude mass concentrations centered on them, more than 98% of the remaining mass is represented by a smooth concentration of DM centered near the brightest cluster of galaxies.

Cosmic Microwave Background Radiation

Despite the compelling evidences for the existence of Dark Matter at the scale of galaxies and galaxy clusters, it proves much harder to determine the *total* amount of DM in the Universe. At this cosmological scale, scientists can however rely on a resourceful ally: the Cosmic Microwave Background (CMB) radiation [18, 19].

The CMB is a thermal radiation characterised by a black body spectrum at a temperature of 2.73 K and which fills the entire Universe almost uniformly (Fig. 5.5). It was serendipitously discovered by Amercian radio astronomers Arno Penzias and Robert Wilson [20] in 1964 and has been thoroughly used since as an incredibly rich source of information about the early ages of the cosmos. According to the Big Bang model, the early Universe was made up of a very hot and dense plasma where all particles were frenetically interacting, preventing the photons from propagating freely. As it expanded and cooled down, protons found favorable to combine with electrons in order to form neutral atoms. This recombination happened approximately 380,000 years after the Big Bang, when the temperature was around 3000 K. It was quickly followed by the decoupling of matter and radiation, causing the Universe to become transparent to radiation. The CMB corresponds to the measurement of this very first radiation which comes from a spherical surface called the *surface of last scattering*.

Detailed observations of the CMB, e.g. by the Wilkinson Microwave Anisotropy Probe (WMAP) [8], can provide stringent constraints on cosmological parameters, and on the abundances of baryons and matter in the Universe in particular. Ever refined data showed that the CMB, although extremely isotropic, present temperature anisotropies. WMAP's measurements played a key role in establishing the current Standard Cosmological Model (ΛCDM, see Subsection

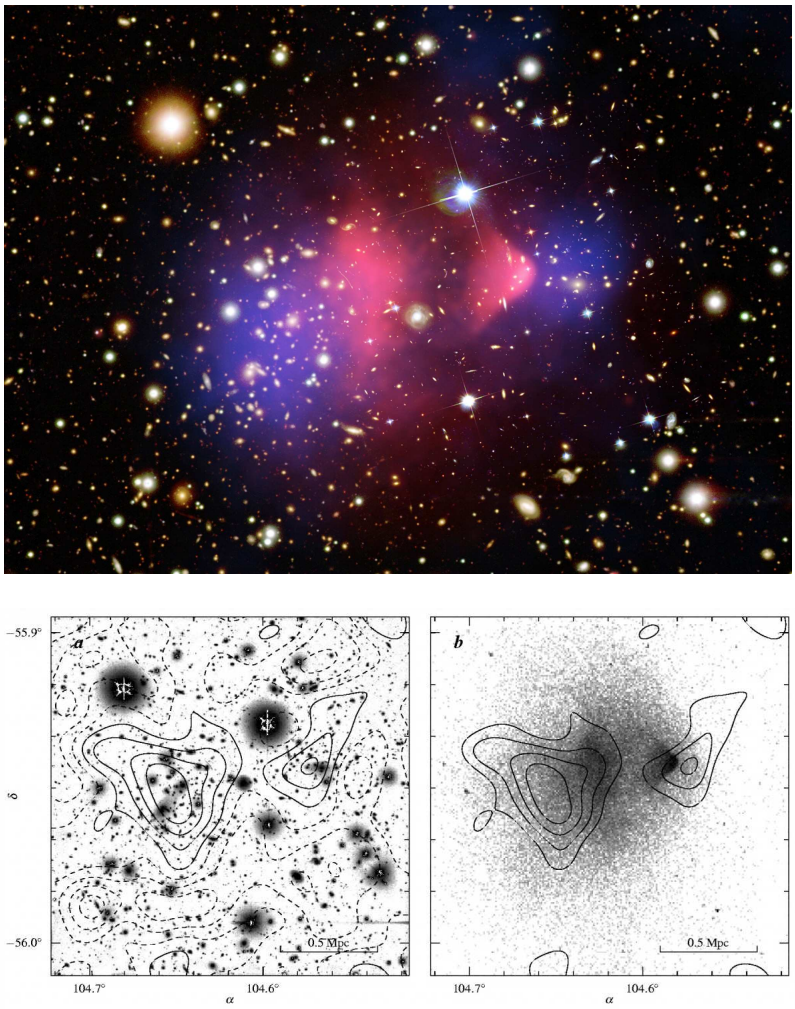

Figure 5.4: ***Top:*** Composite image of the Bullet Cluster: the galaxies are shown in the optical image data; the hot X-ray emitting gas is shown in red; and the blue hues represent the distribution of Dark Matter as inferred from the weak lensing map. The clear separation of gas clouds and DM is considered direct evidence that DM exists.
Bottom: Overlay of the weak lensing mass contours on the optical image of the Bullet Cluster (*left*) and on its X-ray image (*right*), clearly showing that the gas bullet lags behing the DM subcluster.
[Credit: NASA/CXC/CfA [16] and NASA/STScI+ESO WFI/Magellan/U. Arizona [17]]

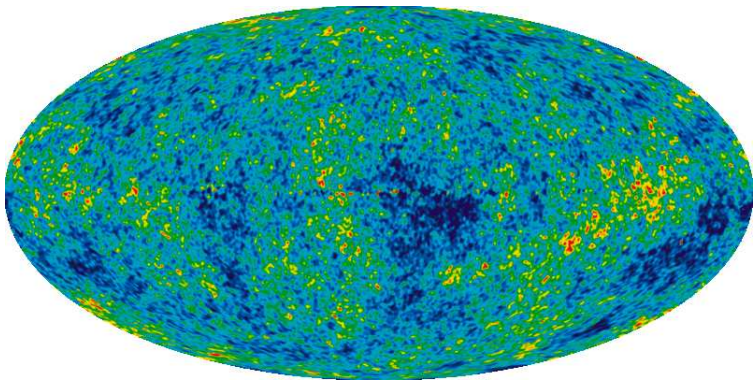

Figure 5.5: Temperature fluctuations of the Cosmic Microwave Background (CMB) radiation, over the celestial sphere, as measured by WMAP 7-year [8]. The range of colours represents the very small discrepancies (of the order of 10^{-5}) from the average temperature of 2.726 K.
[Credit: NASA/WMAP]

5.1.1), characterised by density fluctuations which were seeded by a Gaussian, adiabatic, nearly scale invariant process. Through a relatively complex methodolgy (e.g. [22]), one can extract information about the principal cosmological parameters from CMB anisotropy maps. The objective is to fit the data and their peaks with a cosmological model based on a fixed number of parameters. Among them are the baryon density and the Dark Matter density; their respective values have been estimated by WMAP 7-year data only to be

$$\Omega_b \approx 0.0449 \pm 0.0028 \text{ and } \Omega_{\text{DM}} \approx 0.222 \pm 0.026.$$

Taking into account CMB experiments focused on smaller scales (e.g. [?, ?]) and other cosmological and astrophysical constraints, these values change slightly to become [8]

$$\Omega_b \approx 0.0455 \pm 0.0028 \text{ and } \Omega_{\text{DM}} \approx 0.228 \pm 0.027.$$

But the important thing is to realise that the baryon density Ω_b obtained here is consistent with predictions from Big Bang nucleosynthesis [23] and that a large part of the matter content in the Universe is indeed made of Dark Matter.

5.1.3 Weakly Interacting Massive Particles

One of the most favoured candidate for CDM are Weakly Interacting Massive Particles (WIMPs) [24]. These hypothetical particles, close to neutrinos in many ways except their much higher mass, could solve many astrophysical and cosmological puzzles thanks to their predicted characteristics:

- They interact only through gravity and the weak nuclear force, or at least with interaction cross sections smaller than the weak scale;
- Their mass is much larger than standard particles, of the order of 10 to 1000 GeV[3] typically.

[3] An electron volt, or eV, is a unit of energy equal to approximately 1.602×10^{-19} J. By mass-energy equivalence, the electron volt is also a unit of mass: 1 GeV/c^2 = 1.783×10^{-27}kg. A proton has a mass of $m_{proton} = 0.938$ GeV/c^2, or simply 0.938 GeV in natural units.

Because they interact very little with ordinary matter, WIMPs prove extremely hard to detect. They are, however, the most studied DM candidates and can be found in many particle physics theories because they happen to naturally have the correct relic density and to be detectable using many different techniques. In the following paragraphs, we will discuss their production process and explain the implications for their detection.

Production Process

At the beginning of its evolution, the Universe was very dense and extremely hot, causing all particles to be in thermal equilibrium, and DM particles among them. As it cooled down, its temperature T fell below the value corresponding to the mass of the DM particle m_χ. If we assume that WIMPs are stable and co-annihilate, their number density n_χ would then become Boltzmann suppressed and drop exponentially as $e^{-m_\chi/T}$. They would eventually vanish if the Universe was not expanding at the same time, preventing them from finding each other. When the Universe becomes so large that the DM particles cannot co-annihilate any more, they *freeze out* and their number asymptotically approaches their constant thermal relic density. The density evolution of the WIMPs can be determined precisely using the Boltzmann equation

$$\frac{dn_\chi}{dt} + 3Hn_\chi = -\langle\sigma v\rangle \left(n_\chi^2 - n_{\chi\mathrm{eq}}^2\right),$$

where H is the Hubble parameter, i.e. the expansion rate of the Universe, $\langle\sigma v\rangle$ is the thermally averaged cross section for two WIMPs to annihilate into ordinary particles, and $n_{\chi\mathrm{eq}}$ is the DM number density in thermal equilibrium. The term Hn_χ accounts for dilution from expansion; the n_χ^2 arises from processes $\chi\,\chi \rightarrow$ SM SM which annihilate DM particles (where SM denotes Standard Model particles); and the $n_{\chi\mathrm{eq}}^2$ arises from the reverse processes SM SM $\rightarrow \chi\,\chi$ which create DM particles. The freeze out happens when $n_\chi\langle\sigma v\rangle \approx H$, so we have

$$n_f \sim (m_\chi T_f)^{3/2} e^{-m_\chi/T_f} \sim \frac{T_f^2}{M_{\mathrm{Pl}}\langle\sigma v\rangle} \tag{5.5}$$

where $M_{\mathrm{Pl}} \approx 1.22\times10^{19}\ \mathrm{GeV/c^2}$ is the Planck mass and the subscripts f denote quantities at freeze out. The ratio $x_f \equiv m_\chi/T_f$ appears in the exponential. It is, therefore, highly insensitive to the properties of Dark Matter and may be treated as a constant. The thermal relic density is then

$$\Omega_\chi = \frac{m_\chi n_0}{\rho_c} = \frac{m_\chi T_0^3}{\rho_c}\frac{n_0}{T_0^3} \sim \frac{m_\chi T_0^3}{\rho_c}\frac{n_f}{T_f^3} \sim \frac{x_f T_0^3}{\rho_c M_{\mathrm{Pl}}}\langle\sigma v\rangle^{-1} \tag{5.6}$$

where ρ_{crit} corresponds to the average energy density required for a flat Universe, $\rho_{crit} = 3c^2H_0^2/8\pi G$; the subscripts 0 denote present day quantities. The value of the relic density today can be approximated by

$$\Omega_\chi h^2 \approx \frac{3\times10^{-27}\mathrm{cm^3 s^{-1}}}{\langle\sigma v\rangle}, \tag{5.7}$$

where h is defined by the equation $H = 100\cdot h$ km s^{-1}Mpc^{-1}. Thus, the value of the cosmological parameter does not depend on the Dark Matter mass but is mainly determined by the value of its cross section. The remarkable fact is that

the annihilation cross section $\langle \sigma v \rangle$ for any thermally created particle turns out to be what would be predicted for particles with electroweak scale interactions. So WIMPs would be convincing candidates for Dark Matter as they could easily account for the necessary 23% of the total energy density of the Universe.

Implications for Detection

The WIMP paradigm described above is known as the 'WIMP miracle' and, besides providing a model-independant motivation for DM at the weak scale, it gives some strong indications on how Dark Matter might be detected. We know that WIMPs have to co-annihilate in order to reach the observed relic density; from this annihilation other particles are produced. Assuming that these new particles belong to the Standard Model, one can deduce that the necessity of $\chi\,\chi \rightarrow$ SM SM interactions suggests the following promising strategies for DM detection:

- Direct detection: Dark Matter can scatter off of normal matter through $\chi\,\mathrm{SM} \rightarrow \chi\,\mathrm{SM}$ interactions. Given the expected weak interaction scale of the WIMP-SM particle scattering, DM particles should deposit a measurable amount of energy in an appropriately sensitive detector. If events are indeed observed, they would have to be analysed to determine the nature of the responsible interaction - hopefully enabling an identification of the WIMPs. Conversly, a null observation can be used to improve current limits on the DM particles interaction cross section.

- Indirect detection: since they co-annihilated in the early Universe, there is no reason why WIMPs should not continue doing so at the present time. We hope that products of these $\chi\,\chi \rightarrow$ SM SM interactions may be detected. Particularly interesting situations might rise from the capture of DM by stars or very dense objects, like neutron stars and white dwarves. DM particles would be gravitationally focused into these objects, then captured through collisions with their constituing atoms, and annihilate with each other. The resulting annihilation signal would be greatly enhanced compared to annihilation rates of WIMPs in the very diluted halo of Dark Matter.

- Particle colliders: DM particles may be produced at particle colliders like the LHC at CERN through SM SM $\rightarrow \chi\,\chi$ interactions. Such events would not be detectable *per se*, but could be deduced from the interpretation of related production mechanisms where other SM particles would be created along DM particles: SM SM $\rightarrow \chi\,\chi +$ other SM. These events are observable and provide signature of Dark Matter at colliders.

We do not know how much of Dark Matter is made of WIMPs, but they certainly cannot have an enery density larger than the observed Ω_{DM}. Cosmology therefore provides upper bounds on interaction rates (Fig. 5.6). This fact provides highly motivated targets for a diverse array of experimental searches that may be able to detect WIMPs and constrain their properties. In the present study, we propose to use neutron stars in order to capture DM particles and look for observable consequences.

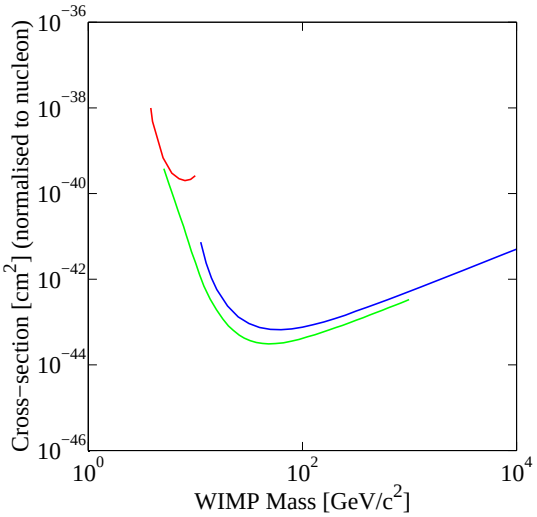

Figure 5.6: Upper bounds on spin-independant WIMP-nucleon cross section as determined by the Cryogenic Dark Matter Search (CDMS) experiment [25] in blue, the (CoGeNT) experiment [26] in red, and the XENON100 experiment [27] in green.
[Plot created with DM Tools Limit Plot Generator [28]]

5.1.4 Asymmetric Dark Matter

A particular class of models for Dark Matter proposes a simple explanation to the fact that the DM density is of the same order of magnitude than the baryon density in the Universe, $\rho_{DM} \sim \rho_{\text{baryon}}$: there is a particle-antiparticle asymmetry for Dark Matter [29, 30, 31] which is related to the baryon-lepton asymmetry. The baryon-lepton asymmetry is thought to be generated by a 'baryogenesis' mechanism, which is part of a strongly supported paradigm in standard cosmology. This asymmetry, occuring in the early Universe, could be transfered to Dark Matter by interactions in equilibrium. In these models, the DM relic density would not be set by its thermal freeze-out, but by the baryon asymmetry.

The asymmetric DM paradigm expects the relation $n_{DM} \sim n_B$, which implies $\Omega_{DM} \sim (m_{DM}/m_B)\Omega_B$. This means that, in order to obtain the appropriate abundance, the mass of the DM particle is situated between $m_{DM} = 5$ GeV and 10 GeV, depending on the model considered. DM particles in this range would provide an explanation for the DAMA results [32, 33]. Since other experiments have higher energy thresholds, particles with masses around 10 GeV may be detected by DAMA while remaining unseen in other cases [34, 35].

5.2 Basics of Neutron Stars

The denser astrophysical objects are, the more likely they are to capture DM particles. Since we are interested in the effects that such capture might produce on the objects themselves, we naturally look for the ones presenting the highest densities. They must, however, present characteristics which can be studied and

which will show observable changes under the effects caused by DM accretion. Given these constraints, among the best candidates are certainly neutron stars (Fig. 5.7).

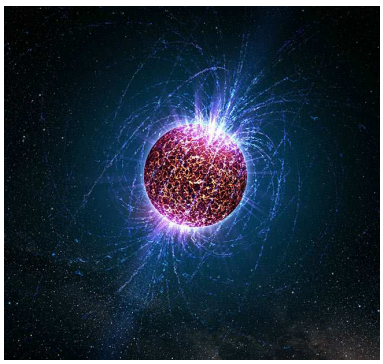

Figure 5.7: Artistic view of a neutron star. [Credit: Casey Reed]

Being composed almost entirely of neutrons, neutron stars are extremely dense and, initially, very hot stellar remnants which are supported against further collapse thanks to the Pauli exclusion principle. In the standard model of stellar evolution (Fig. 5.8), they can result from the gravitational collapse of a massive star (4 to 10 $M_\odot$) during a Type II/Ib/Ic supernova event. Their typical mass lies between 1.35 and 2.0 $M_\odot$ [36], squizzed into a radius of about 10 km. The resulting central densities can reach 2.7×10^{17} kg/m^3 [37], i.e. beyond nuclear saturation density!

During their main sequence evolution, massive stars, unlike the Sun, possess the mass required to fuse heavy elements, until reaching the situation where a core of iron is produced. Nuclear fusion of iron does not generate any net energy, so only electron degeneracy pressure prevents it from collapsing. But when the iron core reaches its Chandrasekhar limit, the mass above which electron degeneracy pressure in the star's core is insufficient to balance the star's own gravitational self-attraction, it imploses until *neutron* degeneracy pressure stops the collapse, causing the implosion to bounce outward - forming the supernova explosion.

In Section 6.4, we propose a more complete discussion of the physical parameters describing neutron stars, with a special attention to the delicate question of their equation of state. So we will limit ourselves here and simply add a succinct explanation concerning a way of estimating the age of neutron stars.

5.2.1 Estimating the Age of a Neutron Star

During their formation process, neutron stars keep most of their angular momentum, and, since their size is drastically reduced during gravitational collapse, their rotation speed might be very high. In some cases, a beam of electromagnetic radiation is emitted along the magnetic axis of the neutron star and spins along with the rotation of the star, then called a *pulsar* (for pulsating star). The source of the power of this radiation may come from the loss of rotational energy of the star, the accretion of matter from a companion in a binary system or the decay of an extremely strong magnetic field (*magnetars*).

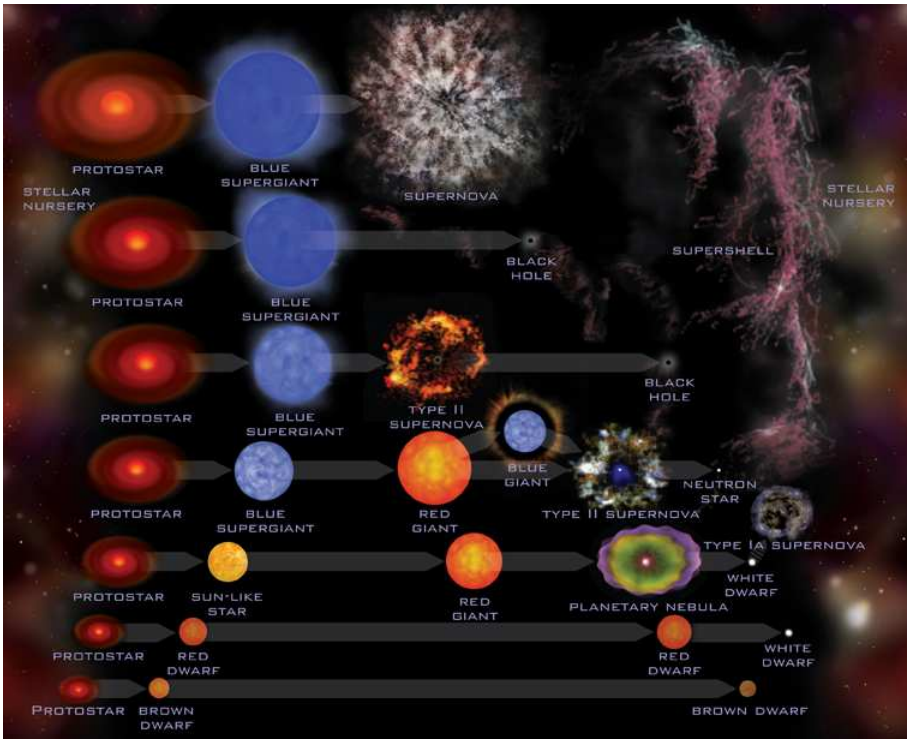

Figure 5.8: Standard model for stellar evolution, for different protostar masses. Neutron stars can be the result of a Type II supernova.
[Credit: NASA/Chandra/Harvard]

The observed periods of these astrophysical pulses range from 1.4 milliseconds to 8.5 seconds [38]. It is believed that the pulsar mechanism usually turnes off when the spin period of the pulsar reaches a lower speed. This "death line" occurs after 10-100 millions years, which means that only 1% of all the neutron stars in our Universe still pulsate.

The interesting aspect about pulsating neutron stars is that one can use the extreme regularity of their pulsation to estimate their age. It can be shown[4] that the product of the period P and its time derivative, $P\dot{P}$, is a constant through time. Using this information and integrating over the pulsar's lifetime τ gives

$$\int_{P_0}^{P} PdP = \int_0^{\tau} (P\dot{P})dt = P\dot{P}\int_0^{\tau} dt$$

since $P\dot{P}$ is assumed to be constant over time. So we obtain

$$\frac{P^2 - P_0^2}{2} = P\dot{P}\tau.$$

If $P_0^2 \ll P^2$, the characteristic age of the pulsar simply is

$$\tau \equiv \frac{P}{2\dot{P}}. \tag{5.8}$$

The characteristic age provides an approximate measure of a pulsar's true age, and the calculation is reasonably valid under three assumptions[5]: 1. as already assumed, $P_0 \ll P$; 2. there is no magnetic field decay; 3. the magnetic braking can be approximated by the energy loss a spinning dipolar magnet would experience in a perfect vacuum. This last point implies that the braking index n in the expression $\dot{\Omega} = -K\Omega^n$ describing the frequency evolution, is equal to 3. The more complete formula would explicitly include this index as well as the initial spin period P_0 as follows

$$\tau = \frac{P}{(n-1)\dot{P}} - \frac{P_0}{(n-1)\dot{P}_0}.$$

These considerations will be most useful in order to understand the implications of Section 7.1.2.

5.3 How to Use Neutron Stars to Probe DM?

The WIMP scenario has gained favour because such particles would fall out of equilibrium with the rest of the plasma at such a temperature that their relic abundance today would be approximately correct to explain the astronomical observations. Such a scenario also predicts a direct detection signal due to the recoil of atoms which are hit by Dark Matter particles, recoils which are being searched for at several purpose built experiments (e.g. [40, 39, 41]). We also expect to see signals from the self-annihilation of WIMP Dark Matter in regions of the galaxy where the density is large, although there are many uncertainties with regards to the magnitude of this signal. Neither of these signals has yet

[4] http://www.cv.nrao.edu/course/astr534/Pulsars.html
[5] http://astronomy.swin.edu.au/cosmos/P/Pulsar+Characteristic+Age

been detected although international efforts to find such signals are intensifying to coincide with the opening of the LHC which also may create WIMP Dark Matter particles.

Since we only understand the thermal history of the Universe back to the start of nucleosynthesis, we cannot say with any surety whether or not the WIMP scenario makes sense. Furthermore there are many other scenarios of Dark Matter which involve much more massive particles or particles which cannot annihilate with themselves [42, 43, 44, 45, 46]. There is roughly 5-7 times the amount of Dark Matter in the Universe by mass relative to baryonic matter. This ratio is rather close to one, a mystery which is only solved within the WIMP framework by a happy coincidence. The closeness of these numbers has led some researchers to suggest that, like baryons, Dark Matter also possesses a conserved charge and there is an asymmetry in this charge in the Universe. If the two asymmetries are related then one would require the Dark Matter mass to be approximately 5-7 times the mass of a nucleon. This intriguing possibility would be consistent with the controversial DAMA experiment [47] and the slight hint of anomalous noise in the CoGeNT experiment [48]. Such a Dark Matter candidate could also have interesting implications for solar physics [49].

Since any constraints on the nature of the mass and cross section of Dark Matter particles are interesting, in this study we will consider both of these paradigms and see whether or not it is possible to obtain any new constraints from a new angle - namely by considering the capture of Dark Matter by neutron stars.

The accretion of Dark Matter onto stellar objects has been considered by various groups looking at both stars [50, 51, 52, 53, 54, 55] and compact objects [56, 57, 58]. In particular, the structure and the ultimate fate of neutron stars which accrete non-annihilating Dark Matter has been discussed before [59, 60, 61, 62].

Our aim is to consider the accretion of Dark Matter onto neutron stars in greater detail in order to examine whether or not it would ever be possible to either observe the heating of a neutron star due to Dark Matter annihilation within the object, or the collapse of a neutron star which accretes non-annihilating Dark Matter.

In the next Chapter we will outline our estimate for the accretion rate of Dark Matter onto a neutron star. Then we will explain which densities we will be assuming for Dark Matter in the Milky Way. We will then go on to work out how hot we can expect a neutron star to get simply due to the accretion of Dark Matter and compare this with observations. Finally we will look at whether it is at all sensible to imagine a situation where the accretion of non-annihilating Dark Matter onto a neutron star would give rise to its subsequent collapse, before concluding.

Chapter 6

Theory and Numerical Models

In this Chapter, we will calculate the rate at which DM particles will accrete onto neutron stars. This re-introduction of the formalism is essentially the same as the existing literature. Where our analysis differs to previous studies is the inclusion of General Relativity (GR) effects in the calculation of the escape velocity. The total capture rate depends on the density of target nuclei and the escape velocity, quantities which both vary throughout the star and will be addressed in the present Chapter. Another essential parameter, the galactic density of Dark Matter, will be discussed in Section 6.5.

6.1 Capture Rate of Dark Matter onto Neutron Stars

The expression which needs to be calculated is the following [65]:

$$C = 4\pi \int_0^{R_\star} r^2 \frac{dC(r)}{dV} dr. \tag{6.1}$$

where the capture rate for a given radius is given by

$$\begin{aligned} \frac{dC(r)}{dV} &= \left(\frac{6}{\pi}\right)^{1/2} \sigma_0 A_n^4 \frac{\rho_\star}{M_n} \frac{\rho_\chi}{m_\chi} \frac{v^2(r)}{\bar{v}^2} \frac{\bar{v}}{2\eta A^2} \\ &\times \left\{ \left(A_+ A_- - \frac{1}{2} \right) \left[\chi(-\eta, \eta) - \chi(A_-, A_+) \right] \right. \\ &\left. + \frac{1}{2} A_+ e^{-A_-^2} - \frac{1}{2} A_- e^{-A_+^2} - \eta e^{-\eta^2} \right\} \end{aligned} \tag{6.2}$$

and the various functions within this expression are

$$A^2 = \frac{3v^2(r)\mu}{2\bar{v}^2\mu_-^2},\ A_\pm = A \pm \eta,\ \eta = \sqrt{\frac{3v_\star^2}{2\bar{v}^2}},$$

$$\chi(a,b) = \int_a^b e^{-y^2} dy = \frac{\sqrt{\pi}}{2} \left[\mathrm{erf}(b) - \mathrm{erf}(a) \right],$$

$$\mu = m_\chi/M_n,\ \mu_- = (\mu - 1)/2.$$

In the above, m_χ is the mass of the DM particle, ρ_χ is the ambient DM mass density, A_n is the atomic number of the neutron star nuclei, M_n is the nucleus mass, $\bar{v}$ is the DM velocity dispersion, $v_\star$ is the star's velocity with respect to the zero point of the DM velocity distribution and $v(r)$ is the escape velocity at a given radius r inside the neutron star (see below); subscript $\star$ refers to the neutron star quantities.

The velocity dispersion $\bar{v}$ is chosen as being constant throughout the galaxy. This is a rather simplistic approximation, especially at small galactic radii where the presence of the central Supermassive Black Hole (SMBH) should cause the velocity dispersion to increase dramatically. The consequences of this will be discussed in Section 7.1.

For neutron stars it is important to note that there is a maximum effective cross section - the sum of all the cross sections of all the nuclei in the object cannot exceed the total surface area of the star since this is obviously an absolute upper limit on the total cross section of the object. Because of this, cross sections in excess of $\sigma_0^{\max} = 2 \times 10^{-45}$ cm^2 will not increase the probability of capture. We will take this into account in what follows.

6.2 Inelastic Dark Matter

One of the ideas which has become a popular explanation of the DAMA results is the idea of inelastic Dark Matter where Dark Matter is some kind of composite, excitable state which can undergo inelastic collisions by some of the collision energy in a given encounter going into knocking the particle into an excited state [63]. This means that there is a minimum and a maximum energy exchange which can take place for a given initial velocity Dark Matter particle scattering off a particular nucleon [64]. In particular it makes the energy exchange required for capture to be less since not all of that energy goes back into elastically back-scattering the impinging Dark Matter particle up to an escaping orbit. Constraints on the capture of Dark Matter onto white dwarves become particularly interesting in such scenarios [58].

In some sense, what we have written below will include the effects of inelastic Dark Matter since the motivation for such models comes from trying to explain data from experiments like DAMA so that the effective cross section needs to be relatively large $\sim 10^{-41}$ cm^2. For such large cross sections, as we have explained above, the neutron star will become opaque for cross sections above about $\sigma_0^{\max} = 2 \times 10^{-45}$ cm^2. The details of the inelastic scattering will not be important since any kind of energy exchange once these particles have been accelerated by gravity as they fall to the surface of the neutron star will dwarf the kind of resonance energies associated with inelastic Dark Matter models invoked to explain the anomalous direct detection experiments. For this reason, the following conclusions should be read as to include the case of inelastic Dark Matter.

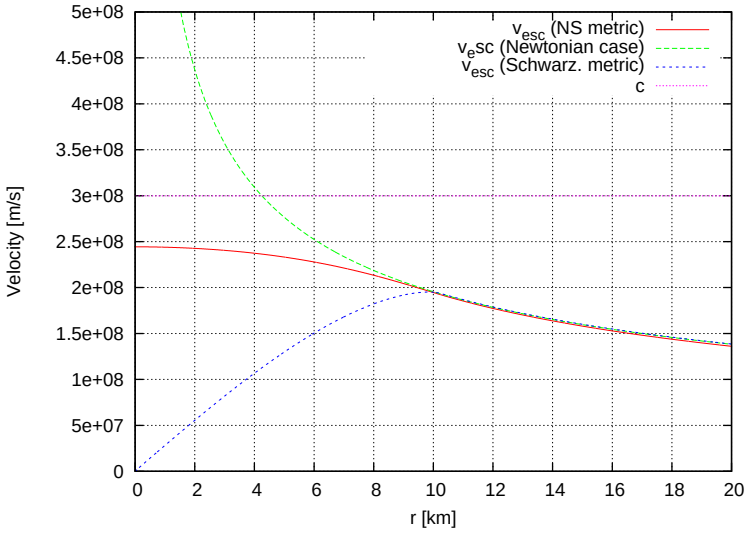

Figure 6.1: Comparison of escape velocities calculated with various methods (see legend). Considering the specific metric describing neutron stars is necessary in order to obtain realistic values close to the stellar centre.

6.3 Neutron Star Escape Velocity

The quantities in Eq. (6.2) have various origins - $\bar{v}$ and ρ_χ depend upon the distribution of Dark Matter in the galaxy and we will discuss them later. The calculation of the escape velocity is more complicated - in a normal star we can simply use Newtonian gravity but if we were to apply the same simple equations to a neutron star we would obtain superluminal escape velocities suggesting the star is unstable. This is of course due to the fact that neutron stars are relativistic objects and we need to take into account GR effects to calculate the escape velocity properly.

The space-time geometry inside a static, spherical fluid star is

$$ds^2 = -e^{2\Phi}dt^2 + \left(1 - \frac{2M(r)}{r}\right)^{-1} dr^2 + r^2 d\Omega^2, \tag{6.3}$$

where $M(r) = 4\pi \int_0^r \rho(r')r'^2 dr'$ and Φ is determined by solutions of

$$\frac{d\Phi}{dr} = \frac{GM(r)/c^2 + 4\pi G r^3 P(r)/c^4}{r\left[r - 2\frac{GM(r)}{c^2}\right]} \tag{6.4}$$

where P is the pressure inside the star. Following the usual Lagrange method of calculating the escape velocity we find that

$$v_{esc}^2 = \frac{1}{\left(1 - \frac{2GM(r)}{rc^2}\right)\left(\frac{d\tau}{dr}\right)^2 + \frac{1}{c^2}} = c^2\left(1 - e^{2\Phi}\right). \tag{6.5}$$

6.4 Neutron Star Physical Parameters

In order to solve equations (6.2) and (6.5), we need to know the neutron star physical parameters, i.e. obtain the density $\rho(r)$ and pressure $P(r)$ as a function of the radius. Assuming that the object we are studying can be considered as a spherically symmetric body of isotropic material in static gravitational equilibrium, we can rely on the Tolman-Oppenheimer-Volkoff equation, which constrains such structure in the context of GR.

When combining this equation with an equation of state relating density to pressure, one completely determines the structure of the neutron star. The non-relativistic limit is found when neglecting the terms of order $1/c^2$ and corresponds to the Newtonian hydrostatic equation.

6.4.1 Tolman-Oppenheimer-Volkoff Equation

The Tolman-Oppenheimer-Volkoff equation is the GR version of the equation of stellar structure [66, 67]:

$$\frac{dP}{dr} = -\frac{G}{r^2}\left[\rho(r) + \frac{P(r)}{c^2}\right]\left[M(r) + 4\pi r^3 \frac{P(r)}{c^2}\right]\left[1 - \frac{2GM(r)}{c^2 r}\right]^{-1}, \tag{6.6}$$

$$\frac{dM}{dr} = 4\pi r^2 \rho(r). \tag{6.7}$$

It is derived by solving Einstein equations for a general time-invariant, spherically symmetric metric. For a solution to the Tolman-Oppenheimer-Volkoff equation, the metric will take the form

$$ds^2 = e^{\nu(r)}c^2dt^2 - \left(1 - 2GM(r)/rc^2\right)^{-1} dr^2 - r^2\left(d\theta^2 + sin^2\theta d\phi^2\right).$$

Since we use this equation to model a bounded sphere of material in the vacuum of space, the two following boundary conditions should be imposed:

$$P(r) = 0 \text{ and } e^{\nu(r)} = 1 - GM(r)/rc^2.$$

This second condition ensures that, at the boundary, the metric is continuous with the Schwarzschild metric, which is the unique static spherically symmetric solution to the vaccum field equations:

$$ds^2 = \left(1 - 2GM_0/rc^2\right)c^2dt^2 - \left(1 - GM_0/rc^2\right)^{-1} dr^2 - r^2\left(d\theta^2 + sin^2\theta d\phi^2\right),$$

which can be rewritten as

$$c^2dt^2 = e^{\nu(r)}c^2dt^2 - e^{\lambda(r)}dr^2 - r^2d\theta^2 - r^2sin^2\theta d\phi^2. \tag{6.8}$$

We integrate Eq. (6.6) and (6.7) outwards for different central pressures. The initial condition for $\Phi(r = 0)$ is chosen so that its value at the surface of the star matches its solution at large radii $\Phi(r > R_{\rm NS}) = \frac{1}{2}\ln(1 - 2GM/rc^2)$. We then vary the central pressure in order to find the maximal mass one can obtain in the given conditions.

i	a_i	i	a_i	i	a_i
1	6.22	7	17.24	13	9.3
2	6.121	8	1.065	14	14.19
3	0.006004	9	6.54	15	23.73
4	0.16345	10	11.8421	16	-1.508
5	6.5	11	-22.003	17	1.79
6	11.844	12	1.5552	18	15.13

Table 6.1: Parameters for the FPS fit.

6.4.2 Equations of State

As an equation of state (EOS) for the neutron star matter, we consider the unified model developed by Pandharipande & Ravenhall [69, 70] which is based on the Friedmann-Pandharipande-Skyrme (FPS) EOS (Fig. 6.2). For non-rotating configurations, they have parametrized the pressure as function of the density in the following way

$$\begin{aligned}\zeta &= \frac{a_1 + a_2\xi + a_3\xi^3}{1 + a_4\xi} f_0\left(a_5(\xi - a_6)\right) + (a_7 + a_8\xi) f_0\left(a_9(a_{10} - \xi)\right) \\ &\quad + (a_{11} + a_{12}\xi) f_0\left(a_{13}(a_{14} - \xi)\right) + (a_{15} + a_{16}\xi) f_0\left(a_{17}(a_{18} - \xi)\right) \quad (6.9)\end{aligned}$$

where $\xi = log(\rho/\mathrm{g\ cm^{-3}})$, $\zeta = log(P/\mathrm{dyn\ cm^{-2}})$ and the a_i coefficients are given in Table (8.1).

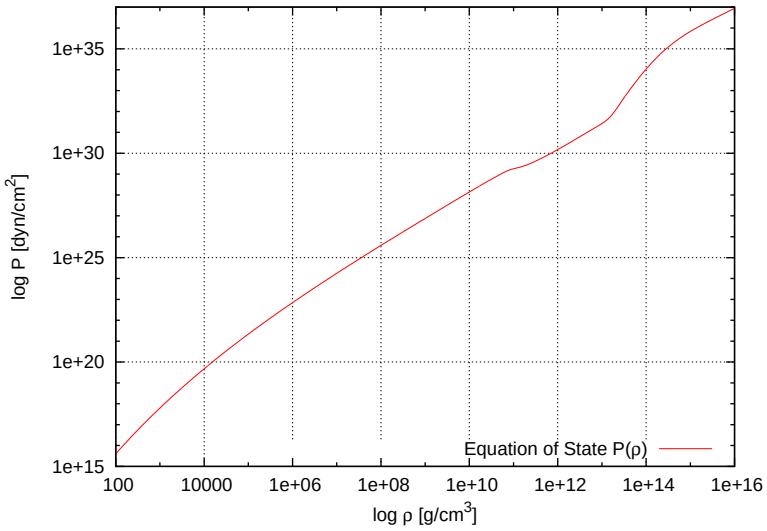

Figure 6.2: FPS parametric model for the neutron star equation of state for non-rotational configurations.

We then simply pick a typical solution which gives a profile apparently shared by the majority of neutron stars [71]: $M_{NS} = 1.44\ M_\odot$, $R_{NS} = 10.6$ km, $\rho_{\mathrm{NS}}^{\mathrm{central}} = 1.4 \times 10^{18}$ kg/m^3 (Fig. 6.3).

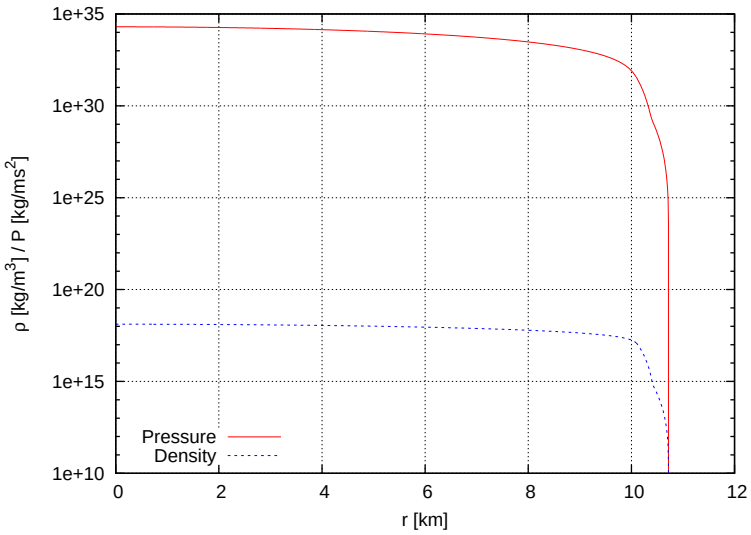

Figure 6.3: Physical parameters for a standard neutron star of mass $M_{NS} = 1.44\ M_{\odot}$.

Once the structure of the neutron star including the escape velocity has been obtained in this way we are half way to being able to calculate the capture rate by integrating equation (6.2). In principle this is not a full calculation because while we are calculating the escape velocity as a function of radius in a way which makes sense, we are not then looking at the effect that curved geodesics will have on the capture rate. Nevertheless, we believe that the capture rate calculated with the machinery presented here will be accurate within a factor of a few. This is an appropriate level of accuracy for this work.

We also need to make some assumption about the expected density of Dark Matter in the galaxy, which is what we will do in the next Section.

6.5 Galactic Density of Dark Matter

One of the essential parameters in the expression of the capture rate (Eq. (6.1) and (6.2)) is ρ_χ, the DM density. Its value varies with respect to the galactic radius, being much higher at small distances from the centre of the Milky Way and progressively decreasing to reach $\rho_\chi \approx 0.3$ GeV/cm^3 in the vicinity of our Solar System (see Section 6.6). In the following paragraphs, we will list existing models for DM density distribution and explain our own choice for the present study.

6.5.1 Existing Models for DM Density Distribution

In order to obtain realistic values for the capture rate of DM onto the neutron star, we ought to know how Dark Matter is distributed throughout the galaxy. Our knowledge is however limited, and many different density profiles have been suggested. The most common of them are the following (Fig. 6.4):

- Navarro-Frenk-White (NFW) profile [72], predicted by N-body simula-

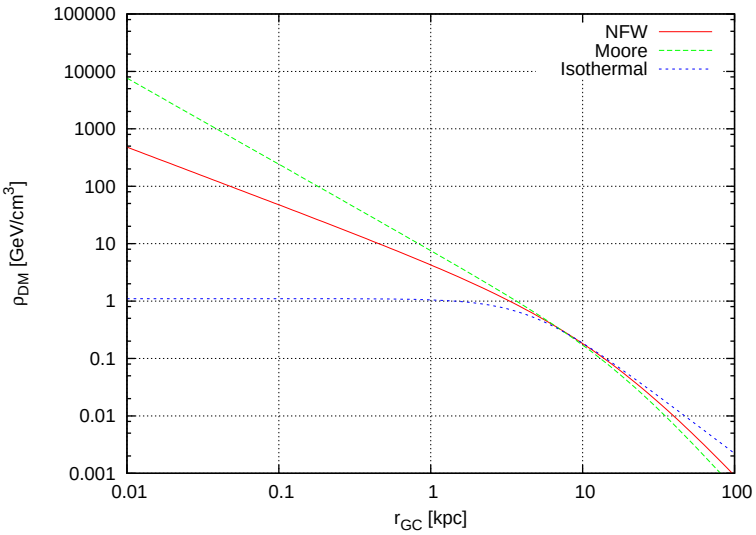

Figure 6.4: Comparison of different DM density profiles, normalized at 0.3 Gev/cm^3 at 8 kpc (corresponding to the location of the Solar System in the Milky Way).

tions, is the most commonly used model for DM halos. The radial distribution is given by the expression:

$$\rho(r) = \frac{\rho_0}{\frac{r}{R_s}\left(1+\frac{r}{R_s}\right)^2},$$

where the values of ρ_0 and R_s, the *scale radius*, may vary depending on the characteristics of each DM halo.
The NFW profile presents a divergent (infinite) central density, but gives a good approximation for collisionless DM particles.

- Moore's profile [73, 74], obtained from higher resolution numerical simulations of DM halos, ressembles the previous profile:

$$\rho(r) = \frac{\rho_0}{\left(\frac{r}{R_s}\right)^{1.5}\left(1+\left(\frac{r}{R_s}\right)^{1.5}\right)},$$

but presents a steeper asymptotic slope, $\rho(r) \propto r^{-1.5}$, and a sharper turnover than that found by lower resolution studies.

- Pseudo-isothermal profile (e.g. [75]), considering an isothermal sphere with a central core, is represented by the following functional form:

$$\rho(r) = \frac{\rho_0}{1+\left(\frac{r}{R_c}\right)^2},$$

where ρ_0 is the central density and R_c is the core radius.

- Time-dependant DM profiles with central spikes [76], which come from the evolution of the DM distribution on sub-parsec scales when integrating the time-dependant Fokker-Planck equation, including effects of self-annihilation, scattering of DM by stars and capture in the central SMBH. Studying models with very high densities, or 'spikes', near the black hole. the authors found order-of-magnitude enhanced densities compared with spike-free models (e.g. $\rho_{\mathrm{DM}}(10^{-4}\ \mathrm{pc}) = 1.2 \times 10^{12}\ \mathrm{GeV/cm^3}$).

6.5.2 Einasto Profiles

In the present approach, we choose to use Einasto profiles of the form

$$\rho(r) = \rho_{-2} e^{-\frac{2}{\alpha}\left[\left(\frac{r}{r_{-2}}\right)^{\alpha}-1\right]},$$

where ρ_{-2} is the DM density at galactic radius r_{-2} where the logarithmic gradient $d\ln\rho/d\ln r = -2$ and α is a parameter describing the degree of curvature of the profile. Jaan Einasto introduced this model in 1963 in order to describe how the density ρ of a spherical stellar system varies with distance r from its centre, but it has been used since then to study many types of system, among which Dark Matter halos. Its basic form is given by $\rho(r) \propto \exp(-Ar^{\alpha})$, where the parameter α controls the degree of curvature of the profile. This law may be thought of as a generalisation of a power law, $\rho \propto r^{-N}$, but with a non constant slope on a log-log plot.

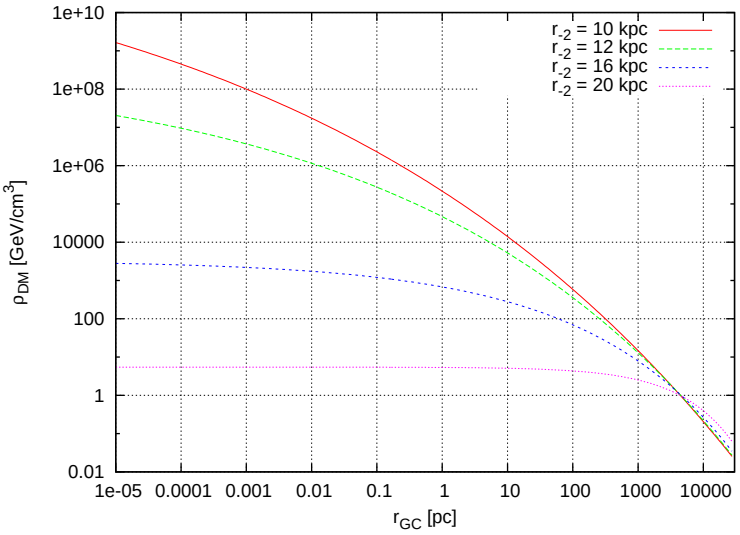

Figure 6.5: Einasto DM density profiles for four different sets of parameters: $(r_{-2}, \alpha) = (10\ \mathrm{kpc}, 0.06)$, $(12\ \mathrm{kpc}, 0.09)$, $(16\ \mathrm{kpc}, 0.19)$ and $(20\ \mathrm{kpc}, 0.53)$.

We choose these profiles because they describe well DM halos of various sizes which appear in N-body simulations [77]. The other advantage is the absence of divergence near the Galactic Centre, which will prove decisive in our situation since we will have to deal with rather small values of galactic radii, at sub-parsec scale.

Several recent studies have estimated the local density of Dark Matter in some detail [78, 79, 80]. We do not go to such lengths and adopt a simpler method, simply ensuring that the enclosed mass at the location of the Sun

$$M_{\rm MW}(R_\odot) = \int_0^{R_\odot} 4\pi r^2 \rho(r) dr$$

yields the correct Keplerian velocity

$$v_{\rm kepl.}(R_\odot) = (G M_{\rm MW}(R)/R_\odot)^{1/2} = 220 \text{ km s}^{-1},$$

where $R_\odot$ is the galactic radius of the Sun. Although it neglects baryons, this gives a reasonable density in line with other methods and gives us a density of 0.3-0.5 GeV cm^{-3} of Dark Matter at the solar radius. One then obtains a 1-parameter set of solutions in α with the corresponding values of r_{-2}, which lie between 10 and 30 kpc (see Fig. 6.5). Note that N-body simulations typically yield values of $\alpha \sim 0.15 - 0.19$ for Milky Way size halos [81]. We will allow a bit more freedom to adopt steeper profiles since we have not explicitly taken into account the effect of baryonic contraction in this work[1] [83, 84].

We will assume that the velocity dispersion of Dark Matter is 200 km s^{-1}. Sometimes it will be smaller and sometimes larger than this depending on the detailed dynamics of the Dark Matter halo and this is a poorly understood subject [85]. We will attempt to model the effect of varying velocity dispersion in Section 7.1.

6.6 Local Dark Matter Density

In order to make sensible predictions, it is essential to determine precisely the amount of Dark Matter that is supposed to be around our Solar System. The local DM density, indeed, fixes the flux of DM particles through which celestial bodies like the Earth and the Sun go. It thus strongly affects, on the one hand, the experimental predictions related to the observation of astrophysical objects. On the other hand, as the DM flux governs the intensity of possible interactions in DM direct and indirect detectors, these experiments crucially depend on the local DM density too.

Determining the local density of Dark Matter represents quite a challenge as it relies on the quality of the observational data and of the theoretical model used to explain them. The former has improved in the recent years, and the combination of the following dynamical constraints [79] should provide us with a fairly accurate idea of the DM density:

1. the total mass of our Galaxy has to be around 10^{12} solar masses [86, 87, 88];
2. the rotation speed of the Solar System constrains the total mass inside the solar orbit;
3. the Hipparcos satellite measured the movements of local stars [89] which determine the gravitational potentiel and thus the total matter density at the position of the Sun;

[1] There is some evidence that baryonic matter in galaxies contracts by a factor of 10 in radius during galaxy formation [82]. This infall could perturb the underlying Dark Matter distribution, pulling it inward and thus creating a much denser central region.

4. the surface density of the visible matter at the same position [90];
5. the surface density of the total matter at the same position [89, 91, 92];
6. the shape of the rotation curve within the galactic disc [93];
7. and the velocity distribution above the galactic disc [88].

The astronomical constraints are consistent with a galactic model for matter density consisting of three components: a central bulge, a disk and an extended DM halo. The usual method to determine the local DM density is to parametrize both luminous and Dark Matter density distributions, and to use dynamical constraints in order to model the mass distribution of our galaxy. These two steps are described in the following Subsections, together with the latest values of the local DM density.

6.6.1 Parametrisation of the Density Distributions

The matter density in galaxies, and in the Milky Way in particular, is assumed to be made of a luminous part, i.e. the standard matter interacting electromagnetically with light, and an invisible part, detectable only through its gravitational effect - Dark Matter. In the case of a spiral galaxy, the former can be split into a galactic disc and a galactic bulge. The parametrisation of the density distribution of the bulge takes the following form [94]:

$$\rho_b(r,z) = \rho_b \left(\frac{m}{r_{0,b}}\right)^{-\gamma_b} \left(1+\frac{\bar{r}}{r_{0,b}}\right)^{\gamma_b-\beta_b} \exp\left(-\frac{\bar{r}^2}{r_t^2}\right), \tag{6.10}$$

$$\bar{r}^2 = \sqrt{x^2+y^2+(z/q_b)^2},$$

where, for a good description of the rotation curve near the Galactic Centre, the different parameters are found to be

γ_b	β_b	q_b	r_t	$r_{0,b}$	ρ_b
1.6	1.6	0.61	0.6	0.7	360 GeV cm^{-3}

Table 6.2: Values for the parametrisation of the density distribution (bulge).

The parametrisation of the disc is usually expressed as an exponentially decreasing density distribution [95]

$$\rho_d(r,z) = \rho_d \exp(-r/r_d) \exp(-z/z_d), \tag{6.11}$$

where ρ_d is the central density of the galactic disc, r_d and z_d act as scale parameters in the radial and vertical direction respectively. As the central density is unknown, ρ_d is kept as a free parameter. The scale radius can be taken to be $r_d = 2.3 \pm 0.6$ kpc [96], and the scale height $z_d \approx 320$ kpc [97]. This parametrisation leads to a mass of the galactic bulge of about $1.1 \times 10^{10}\ M_\odot$ and a mass of the galactic disc of about $6 \times 10^{10}\ M_\odot$.

The density profile of the Dark Matter halo is believed to be well fitted by the universal function

$$\rho_\chi = \rho_{\odot,\mathrm{DM}} \left(\frac{\bar{r}}{r_\odot}\right)^{-\gamma} \left[\frac{1+\left(\frac{\bar{r}}{a}\right)^\alpha}{1+\left(\frac{r_\odot}{a}\right)^\alpha}\right]^{\frac{\gamma-\beta}{\alpha}}, \qquad (6.12)$$

$$\bar{r} = \sqrt{x^2 + \frac{y^2}{\epsilon_{xy}^2} + \frac{z^2}{\epsilon_z^2}},$$

where a is the scale radius fixing the distance at which the slope of the density profile changes (based on numerical N-body simulations [98]), ϵ_{xy} and ϵ_z are the eccentricities of the DM halo perpendicular to the galactic plan (often taken to be equal to 1 for axisymmetrical halos) and $r_\odot$ is the distance between the Solar System of the centre of our galaxy. The parameter $\rho_{\odot,\mathrm{DM}}$ is the DM density at the galactic radius of the Sun. The parameters denoted by Greek letters characterize the radial behaviour of the density distribution, allowing three different trends depending on the value of the ratio $\bar{r}/a$. Table 6.3 shows the set of values for the first two profiles discussed in Subsection 6.5.1.

Profile	α	β	γ	a [kpc]	Reference
NFW	1.0	3.0	1.0	20.0	Navarro *et al.* (1997) [98]
Moore	1.5	3.0	1.5	30.0	Moore *et al.* (1999) [99]

Table 6.3: Values for the parametrisation of two typical density distributions of the Dark Matter halo.

6.6.2 Application of Dynamical Constraints

Once the parametrisation of the density distributions are set, constraints must be applied in order to determine the value of the different parameters involved. The mass model of the Milky Way is primarily constrained by the following elements: the total mass of the galaxy, the rotation velocity of the Sun $v(r_\odot)$ and the local matter density $\rho_{\mathrm{tot}}(r_\odot)$.

The **total mass of the Milky Way** is usually measured via the kinematics of distant halo tracer stars of satellite galaxies. As its slowly decreasing density profile has a theoretically infinite extension, the *virial radius* is conventionally chosen as an arbitrary final value. Tihs is the radius at which the total enclosed mass is equal to the mass of a homogeneous sphere with a constant density 200 times higher that the critical density of the Universe[2]. Using a simple parametrisation of the potential and measurements of the radial velocities of globular clusters and satellite galaxies leads to a total mass of $M_{\mathrm{tot}} = 1.9^{+3.6}_{-1.7} \cdot 10^{12}\ M_\odot$ [86], which is compatible with the approximate based on tracer stars $M_{\mathrm{tot}} = 2.5^{+0.5}_{-1.0} \cdot 10^{12}\ M_\odot$ [100]. Because of their steeper density fall-off at large distances, NFW profiles yield a lower total mass. Combining a large sample of stars from SDSS and N-body simulations, Xue *et al.* [88] found

$$M_{\mathrm{tot}} = 4.0 \pm 0.7 \cdot 10^{11}\ M_\odot.$$

[2] In a FLRW Universe, the critical density is obtained by setting Λ and the spatial curvature to zero in the Friedmann equation 5.3: $\rho_c = 3H^2/8\pi G$.

The best determination and normalization of the **rotation velocity** at the Sun position is derived from the Oort constants which are defined as [95, 101]

$$A = -\frac{1}{2}\left[\frac{dv}{dr}|_{r_\odot} - \frac{v(r_\odot)}{r_\odot}\right] \approx 14.4 \pm 1.2 \text{ km s}^{-1}\text{kpc}^{-1},$$

$$B = -\frac{1}{2}\left[\frac{dv}{dr}|_{r_\odot} + \frac{v(r_\odot)}{r_\odot}\right] \approx -12.0 \pm 2.8 \text{ km s}^{-1}\text{kpc}^{-1}.$$

Using the proper motion of the central black hole Sgr A*, the combination of these constants can be precisely determined [102]

$$A - B = \frac{v(r_\odot)}{r_\odot} = 29.45 \pm 0.15 \text{ km s}^{-1}\text{kpc}^{-1},$$

which gives a rotation velocity of the Sun of

$$v(r_\odot) = 244 \pm 10 \text{ km s}^{-1},$$

considering a galactic radius of $r_\odot = 8.33 \pm 0.35$ kpc [103].

The third main constraint on the mass model of the Milky Way is the total **local mass density** $\rho_{\odot,\text{tot}}$, also called Oort limit. Its calculation is derived from the star count as a function of their height above the disc, through the local gravitational potential which is proportional to the mass in the plane of the galaxy. Based on the precise measurements from the Hipparcos satellite, the value of the local mass density, including visible matter as well as Dark Matter, is found to be [89]

$$\rho_{\odot,\text{tot}} = 0.102 \pm 0.010 \; M_\odot\text{pc}^{-3}.$$

The three most important constraints described here allow one to model the mass distribution of the Milky Way. If the shapes of the DM distribution and the visible matter were known, one would actually have 3 constraints with only two variables, ρ_{visible} and ρ_{DM}. They indeed suffice to quantify M_{tot}, $v(r_\odot)$ and $\rho_{\odot,\text{tot}}$ in the following way: $v^2(r_\odot) = v^2_{\text{visible}} + v^2_{\text{DM}}$, where the velocities are proportional to the respective density; for a given halo, M_{tot} is given by the integration of the densities and the Oort limit is of course $\rho_{\odot,\text{tot}} = \rho_{\text{visible}} + \rho_{\text{DM}}$. But there is no certainty about the exact shapes of the density distributions, and essential parameters cannot be fixed, e.g. the eccentricity and concentration of the DM halo, the scale length of the disc and the mass ratio between the bar and the bulge of the galaxy.

6.6.3 Latest Values of the Local DM Density

Given the free parameters and constraints discussed above, a χ^2 minimization is undertaken in order to find the set of parameters best describing the data. The local Dark Matter density found through this process will depend on the cosmological model used and the assumptions made. Table 6.4 shows fit results for different NFW profiles [79]; the resulting local DM densities are plotted on Fig. 6.6.

The astronomical constraints described above are consistent with a mass model of the Milky Way consisting of a central bulge, a disc and an extended Dark Matter halo. The local DM density, as shown in Fig. 6.6, should lie

Nr	$\rho_{\odot,\mathrm{DM}}$ [GeV cm^{-3}]	a [kpc]	ρ_d [GeV cm^{-3}]	$\rho_{\odot,\mathrm{tot}}$ [$M_\odot$pc^{-3}]	M_{tot} [$M_\odot$]
1	0.32 ± 0.05	10	88.3 ± 19.8	0.094	$6.5 \cdot 10^{11}$
2	0.27 ± 0.06	15	113.1 ± 17.1	0.096	$7.4 \cdot 10^{11}$
3	0.23 ± 0.05	20	128.7 ± 69.8	0.097	$8.3 \cdot 10^{11}$
4	0.32 ± 0.04	10.8 ± 3.4	91.0 ± 8.0	0.095	$6.7 \cdot 10^{11}$
5	0.35 ± 0.06	14.9 ± 4.8	89.5 ± 8.2	0.094	$9.8 \cdot 10^{11}$
6	0.39 ± 0.05	20.4 ± 4.5	88.1 ± 8.7	0.094	$1.49 \cdot 10^{12}$
7	0.41 ± 0.05	25.2 ± 4.6	87.3 ± 8.9	0.094	$1.98 \cdot 10^{12}$

Table 6.4: Results of the local Dark Matter density fitting process for different NFW profiles. The parameters are described in the text and units are given in square brackets. The first three fits were performed for fixed values of a, whereas profiles 4 to 7 have a constant value for the disc scale length of $r_d = 2.5$. The rotation velocity of the Sun is $v(r_\odot) = 244.5$ km s^{-1} for the first two profiles, and then it is equal to 244.4 km s^{-1}.

between 0.2 and 0.4 GeV cm^{-3}, with strong correlations between the parameters, specially $\rho_{\odot,\mathrm{DM}}$ and M_{tot}. For non-spherical halos, these values can be enhanced by 20%, and, if dark discs are considered, densities up tp 0.7 GeV cm^{-3} can easily be reached.

In the case of an Einasto profile, which we are considering in this study, the best estimate of the local DM density including the flattening of the dark halo due to the inclusion of baryons, is [104]

$$\rho_{\odot,\mathrm{DM}} = 0.466 \pm 0.033(\mathrm{stat}) \pm 0.077(\mathrm{syst})\ \mathrm{GeV\ cm^{-3}},$$

where the first uncertainty accounts for the statistical errors, and the second one for the systematic errors introduced by the lack of knowledge about the shape of the dark halo and its reaction to galaxy formation.

6.7 Annihilating Dark Matter

Now that we have the neutron star density and escape velocity profiles and models for the density of Dark Matter in the Milky Way, we can calculate how much Dark Matter will be captured using equation (6.2). The result as a function of radius for the four different density profiles can be seen in Fig. 6.7.

6.7.1 Annihilation of Dark Matter and Injection of Energy

We next need to analyse what happens to Dark Matter once it has been captured. In order to do this, we base our calculations on Kouvaris's work [57], adapting the formulae to our situation when necessary. For most cases of interest where the scattering cross sections are not microscopically small, one can show that the captured WIMPs will thermalise relatively quickly, forming a roughly Maxwell-Boltzmann distribution in velocity and distance around the centre of the neutron star. If the particle we consider is an ordinary WIMP which can annihilate with itself it will do so at a rate determined by the self-annihilation cross section and the density of Dark Matter in the star. Following

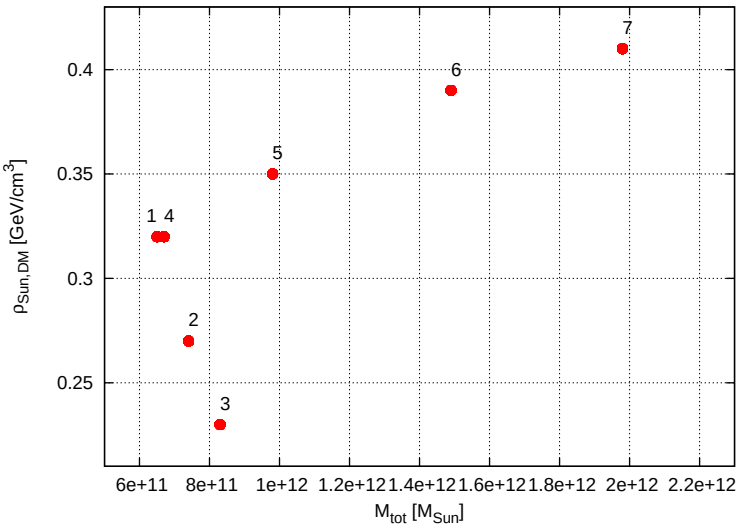

Figure 6.6: Local Dark Matter densities $\rho_{\odot,\mathrm{DM}}$ as a function of the total galactic mass M_{tot} for the different sets of parameters listed in Table 6.4.

Kouvaris' argument, we assume that in most interesting situations (where the self-annihilation cross section corresponds to that required for a good relic abundance), the annihilation rate reaches the accretion rate (Fig. 6.7) within around 10 million years, which is also approximately the time where the DM annihilation begins to affect the temperature of the neutron star.

6.7.2 Cooling of the Neutron Star

While some energy will be lost to neutrinos, the energy generated by the annihilation of most Dark Matter candidates is carried in the main by leptons, quarks and photons. We therefore neglect that part lost to neutrinos and assume that all the annihilation mass energy goes into heating the neutron star.

Since all the dominant cooling processes involved in this situation scale with some positive power of the temperature except for the WIMP annihilation emissivity, the latter will dominate at some point in the life of the star.

The cooling of the neutron star is given by the following differential equation:

$$\frac{dT}{dt} = \frac{-\epsilon_\nu - \epsilon_\gamma + \epsilon_{\mathrm{DM}}}{c_V}, \tag{6.13}$$

where c_V is the heat capacity of the star. ϵ_{DM} is the emissivity (released energy per volume per time) produced by the annihilation of the DM when the latter saturates and is given by $\epsilon_{\mathrm{DM}} = 3Cm_\chi/4\pi R^3$. ϵ_ν is the emissivity due to the modified Urca process, which makes the neutron star lose energy through neutrino emission by converting protons and electrons to neutrons and vice versa, and is given by [105]

$$\epsilon_\nu = (1.2 \times 10^3 \mathrm{J\,m^{-3}s^{-1}}) \left(\frac{n}{n_0}\right)^{2/3} \left(\frac{T}{10^7 \mathrm{K}}\right)^8 \tag{6.14}$$

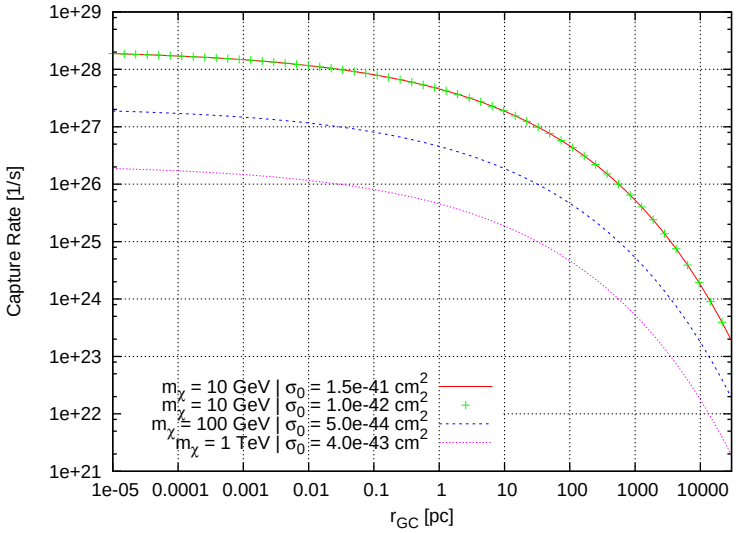

Figure 6.7: Dark matter accretion rates vs. galactic radius for four different configurations of Dark Matter (cf. legend in figure) and with $(r_{-2}, \alpha) = (16\ \text{kpc}, 0.19)$. The merging of the two first cases is due to the fact that we take into account the limiting geometrical cross section of the neutron star surface.

(where n is the baryon density in the star and $n_0 = 0.17\,\text{fm}^{-3}$ the baryon density in nuclear matter). Finally, ϵ_γ accounts for the effective emissivity in photons measured in energy over volume and time and is given by

$$\epsilon_\gamma = \frac{L_\gamma}{(4/3)\pi R^3} \simeq 1.56 \times 10^{13} \left(\frac{T}{10^8 \text{K}}\right)^{2.2} \text{J m}^{-3}\text{s}^{-1}, \tag{6.15}$$

where L_γ simply is the rate of heat loss from the surface of the neutron star: $L_\gamma = 4\pi R^2 \sigma T^4_{\text{surface}}$ (with σ the Stefan-Boltzmann constant).

6.7.3 Change in Outward Appearance

The DM heats the neutron star at a constant rate which will dominate any other thermal process at late times. Note that, since when the DM particles annihilate their equilibrium density corresponds to a negligible fraction of the total mass, we have neglected the contribution of the WIMPs to the specific heat.

In order to determine the thermal evolution of the star through its internal and surface temperatures, we solve numerically the differential equation (6.13). As the temperature at interesting times (i.e. beyond 10^6 years when the star starts to cool down) is reasonably insensitive to the initial conditions, we arbitrarily set $T(t = 0) = 10^9$ K. Since we are interested in the changes occuring in the outward appearance of the star, we ought to know what happens in its visible part, namely its *envelope*, which is defined as the layer extending from the *photosphere* (the upper-most layer where the emitted spectrum is determined), down to a boundary radius r_b such that the luminosity in the envelope equals the total surface luminosity of the star.

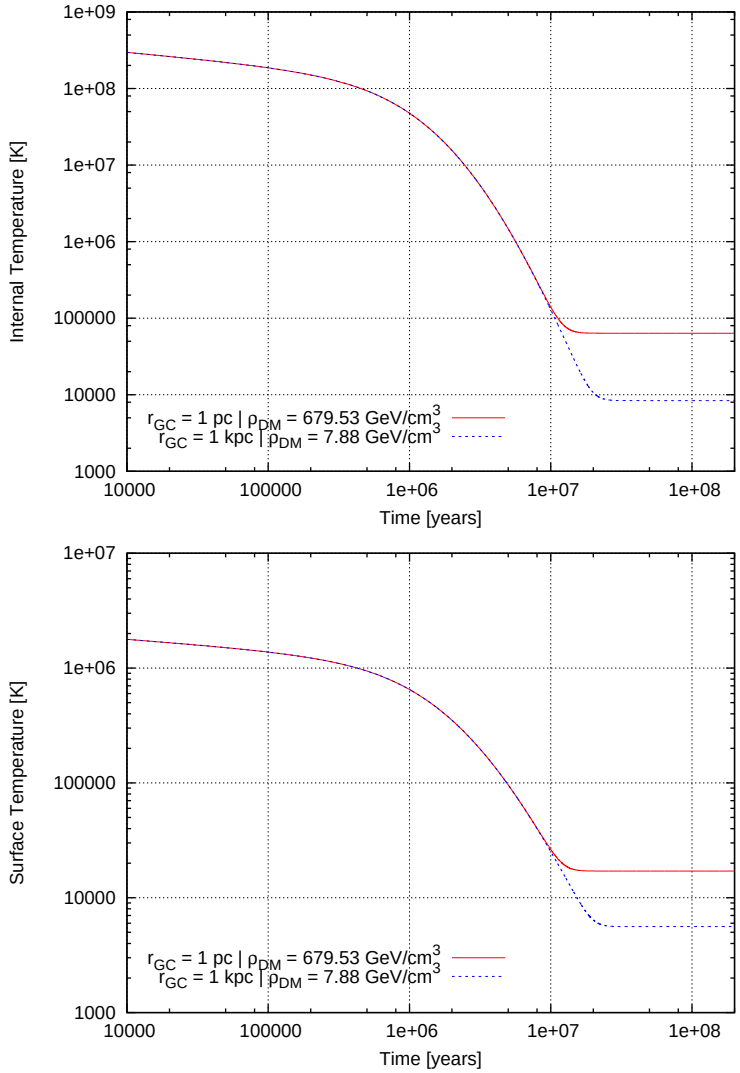

Figure 6.8: Evolution of the internal (above) and surface temperatures of a 1.44 $M_\odot$ neutron star situated at two different galactic radii. In the present case, $m_\chi = 10$ GeV, $\sigma_0 = 1.5 \times 10^{-41}$ cm^2 and $(r_{-2}, \alpha) = (16\ \text{kpc}, 0.19)$.

Neutron Stars Surface Temperature

The thermal structure of neutron stars is determined by the Tolman-Oppenheimer-Volkoff equation of hydrostatic equilibrium, Eq. (6.6), and the energy transport equation, which is given by [106, 107]

$$\frac{d}{dr}\left(Te^{\Phi}\right) = -\frac{3}{16\sigma}\frac{\kappa\rho}{T^3}\frac{L}{4\pi r^2}e^{\Phi}\left(1-\frac{2GM}{rc^2}\right)^{-1/2}, \tag{6.16}$$

where ρ is the mass-energy density, r the Schwarzschild radial coordinate and $M(r) = \int_0^r 4\pi r^2 \rho(r) dr$ the enclosed gravitational mass. T is the temperature,

κ the total opacity of the matter, L the luminosity due to the thermal conduction and radiation, σ the Stefan-Boltzman constant and e^{Φ} the redshift factor, defined by Eq. (6.4) and which is equal to $\left(1-2GM/rc^2\right)^{1/2}$ outside the star.

Surface Temperature Approximation

In [106], the authors develop detailed calculations and careful simplifications in order to finally produce a simple analytical relationship between the surface temperature T_s and the internal temperature T. Choosing appropriate ranges of values for the different parameters, they find the following expression to fit their results:

$$T = 1.288\left(\frac{T_{s6}^4}{g_{s12}}\right)^{0.455}, \tag{6.17}$$

where g_{s12} is the surface gravity on the neutron star $g_s = GM_{\rm NS}/R_{\rm NS}^2$ measured in 10^{12} m/s^2. This can be expressed as [108, 109] :

$$T_{\rm s} = (0.87\times 10^6\,{\rm K})\left(\frac{g_s}{10^{12}\,{\rm m/s^2}}\right)^{1/4}\left(\frac{T}{10^8\,{\rm K}}\right)^{0.55}.$$

We can see that $T_s \propto T^{1/2}$ and $T_s \approx 10^6$ K when $T \approx 10^8$ K. This relation shows that the dependence of the envelope structure on $M_{\rm NS}$ and $R_{\rm NS}$ is entirely contained in g_s. $T_s/g_{s12}^{1/4}$ being independent of these two parameters, the use of generic envelope models is possible.

6.8 Notes on Numercial Models

A large part of the numerical models developed for this part of our research is based on our previous work on black hole accretion (Part I). The integration process is implemented as a standard fourth order Runge-Kutta method, adapted for a set of interdependent ordinary differential equations.

6.8.1 Determining Einasto Profiles Parameters

One critical point in the developement of our simulation code is the calculation of the Einasto profiles as defined in Subsection 6.5.2. Throughout our study, we will be using the series of predefined DM density distributions shown in Fig. 6.5, each with a different set of parameters in order to measure the impact on the results.

In order to determine the set of parameters $(r_{-2}, \rho_{-2}, \alpha)$ defining each density profile through

$$\rho(r) = \rho_{-2}e^{-\frac{2}{\alpha}\left[\left(\frac{r}{r_{-2}}\right)^{\alpha}-1\right]},$$

we implemented the following procedure:

1. Choose a value for r_{-2} and make an initial guess for the value of α;
2. Integrate $\int_0^{r_\odot} e^{-\frac{2}{\alpha}\left[\left(\frac{r}{r_{-2}}\right)^{\alpha}-1\right]}$ and figure out what value of ρ_{-2} would yield the same mass of the Milky Way

$$M_{\rm MW}(r_{GC,\odot}) = r_{GC,\odot}v_{\rm Kep}^2/G - M_{\rm b}(r_{GC,\odot}),$$

where $r_{GC,\odot}$ is the galactic radius of the Sun, $v_{\rm Kep} = 220$ km/s is the Keplerian velocity at the position of the Solar System and $M_b(r_{GC,\odot}) = 4.533e \times 10^{10}\ M_\odot$ (see below) is the baryonic mass enclosed within $r_{GC,\odot}$;

3. Integrate $\int_0^{r_{200}} \rho(r)dr$, where r_{200} is the galactic radius where the average enclosed density equals 200 times the critical density $\rho_c = 3H^2/8\pi G$ (see footnote in 6.6.2), and compare the result to the total mass of the Milky Way $M_{\rm MW} = 1.5 \times 10^{12}\ M_\odot$ [110];

4. If the mass values are similar, then we have found a consistent set of parameters $(r_{-2}, \rho_{-2}, \alpha)$. Otherwise, the value of α is modified and we start again from point 2.

The whole procedure is repeated for different values of r_{-2}. Table 6.5 shows the results obtains for 10 Mpc $< r_{-2} <$ 20 Mpc.

r_{-2}	ρ_{-2}	α	r_{-2}	ρ_{-2}	α
10	0.20397	0.06476	16	0.107900	0.193500
11	0.17223	0.07444	17	0.105770	0.240850
12	0.15133	0.09083	18	0.106828	0.302788
13	0.13430	0.10758	19	0.111165	0.388305
14	0.12158	0.12868	20	0.124023	0.528610
15	0.11340	0.15701			

Table 6.5: Sets of parameters $(r_{-2}, \rho_{-2}, \alpha)$ determining different Einasto profiles for the DM density distribution in the Milky Way.

The calculation of the enclosed baryonic mass $M_b(r_{GC})$, used in the second step of the procedure described above, is based on the combination of the spherical density of the bulge and the surface density of the galactic disk. These densities are given by [111]

$$\rho_{\rm Bulge}(r) = \rho_\lambda \left(\frac{r}{\lambda}\right)^\gamma e^{1-r/\lambda},$$

where $\rho_\lambda = \rho_{\rm Bulge}(r = \lambda)$ which is adjusted numerically so that

$$\int_0^{r=30\ {\rm kpc}} 4\pi r^2 \rho_{\rm Bulge}(r)dr = M_b^{\rm Theoretical} = 1.3 \times 10^{10}\ M_\odot,$$

and

$$\sigma_{\rm Disk}(r) = \frac{cM_{\rm Disk}^\infty}{2\pi(c^2 + r^2)^{3/2}},$$

where $M_{\rm Disk}^\infty$ is the theoretical total mass of the galactic disk. In order to match observations of the Milky Way, the following parameters are chosen: $\gamma = 1.85$, $\lambda = 1$ kpc, $c = 5$ kpc and $M_{\rm Disk}^\infty = 6.5 \times 10^{10}\ M_\odot$.

The two components of the total mass

$$M_b(r_{GC}) = M_b^{\rm Bulge}(r_{GC}) + M_b^{\rm Disk}(r_{GC})$$

are obtained by integrating the corresponding densities along the radial coordinate

$$M_b^{\text{Bulge}}(r_{GC}) = \int_0^{r_{GC}} 4\pi r^2 \rho_{\text{Bulge}}(r) dr,$$

$$M_b^{\text{Disk}}(r_{GC}) = \int_0^{r_{GC}} 2\pi r \sigma_{\text{Disk}}(r) dr.$$

The resulting total baryonic mass of the Milky Way is presented in Fig. 6.9. The initial constant value near the Galactic Centre is due to the presence of the SMBH of mass $M_{\text{SMBH}} = 3.7 \times 10^6\ M_\odot$ (cf. Section 1.3). The value we will be considering in our simulations for the baryonic mass at the radius of Solar System is

$$M_b(r_{GC,\odot}) = 4.533 \times 10^{10}\ M_\odot.$$

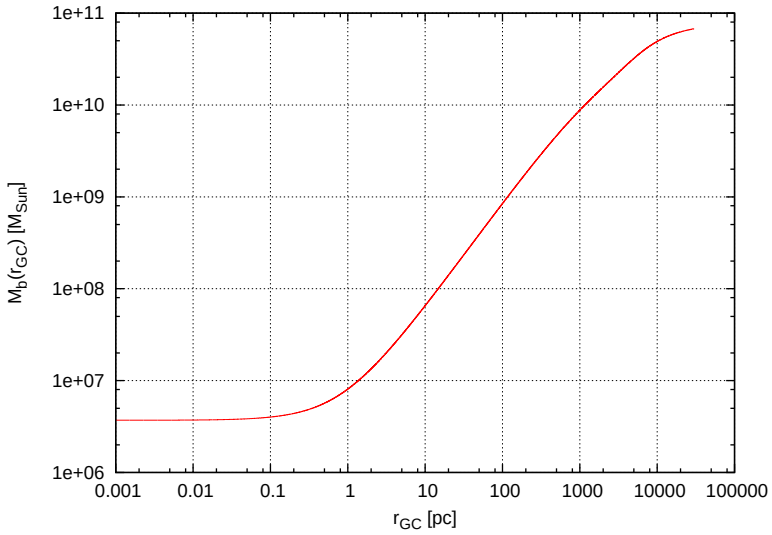

Figure 6.9: Total baryonic mass M_b in the Milky Way as a function of the galactic radius r_{GC}. The constant value at small distances corresponds to the presence of the SMBH of $3.7 \times 10^6\ M_\odot$.

Chapter 7

Results and Discussion

In this Chapter, we will present two series of results: first on annihilating Dark Matter, with possible observable consequences; then on non-annihilating Dark Matter, with corresponding constraints on its parameter space. Confrontation with observational data and further theoretical interpretations will be added in the respective parts.

7.1 Results for Annihilating Dark Matter

Changing the position of the neutron star in the galaxy changes the accretion rate of Dark Matter which in turn changes the temperature of the neutron star due to internal Dark Matter annihilation.

Since we are working with a 1-parameter set of density profiles, our predictions will be model-dependent. However, knowing the discrepancy between the different DM density distributions gives us a relatively good picture of the whole space of possibilities and since many relations involved in the process are linearly related to the density parameter, the reader can scale our results up or down as required.

For every pair of parameters (r_{-2}, α) defining an Einasto profile which matches our given constraints, we define the properties ($m_{\rm DM}$,σ_0) of the DM particle we want to probe; we then calculate the capture rate for our standard neutron star and we finally apply the temperature gradient given by Eq. (6.13) in order to find the final internal and surface temperatures. In Fig. 6.8, we present an example of our results, with $m_\chi = 10$ GeV and $\sigma_0 = 1.5 \times 10^{-41}$ cm^2.

As previously mentioned in Section 6.1, we decided to use a constant velocity dispersion in our simulations for the sake of clarity. Near the Galactic Centre, however, the velocity dispersion increases significantly due to the presence of the central SMBH (Fig. 7.1). The results shown here are deduced from the static radial Jeans equation

$$\frac{1}{\rho}\frac{\partial}{\partial r}\left(\rho\sigma_R^2\right) + 2\frac{\beta\sigma_R^2}{r} = -\frac{GM(r)}{r^2},$$

using $\sigma^2 = 2\sigma_T^2 + \sigma_R^2$ as the three dimensional velocity dispersion and σ_R and σ_T as the one dimensional velocity dispersions in the radial and tangential directions

(assuming a spherically symmetric DM distribution so that $\sigma_\theta = \sigma_\phi = \sigma_T$); $\beta = 1 - \sigma_T^2/\sigma_R^2$ is the anisotropy parameter. We use the relationship

$$\beta = -0.31 - 0.295\gamma$$

which comes from a rough fit to the regular line in the $\beta - \gamma$ plane found in figure 11 of the paper [112].
$M(r)$ is given by the sum $M(r) = M_{Baryons}(r) + M_{DM}(r)$, where the latter is simply integrated from the DM density profile and the former is obtained by considering standard baryonic density distributions in our galaxy. We assume the presence of a SMBH of mass $3.7 \times 10^6\ M_\odot$ and total masses at a galactic radius of 30 kpc for the bulge and the disk of respectively $1.3 \times 10^{10}\ M_\odot$ and $6.5 \times 10^{10} M_\odot$.

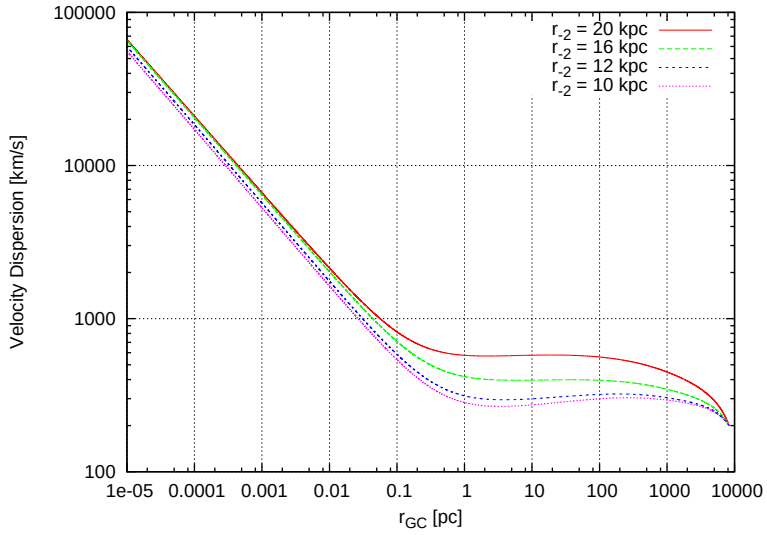

Figure 7.1: Velocity dispersions with respect to the galactic radius for the four different Einasto DM density profiles considered in the present article.

The capture rate depends in a non trivial way on this quantity, basically decreasing for larger values of the velocity dispersion. The emissivity due to DM annihilation will follow the same general trend, leading to lower final surface temperatures of the neutron star (Fig. 7.2).

We would like to point out however that this is not the only possible way of calculating the velocity dispersion of Dark Matter. In particular, it has been noted in N-body simulations that the pseudo-phase space density $\rho/\sigma^3 \propto r^{-1.875}$ [113] which is very close to the value obtained in spherical infall calculations [114]. If we assume that this relation is true, then the velocity dispersion falls towards the centre of the galaxy, even in the presence of baryonic contraction. However, we shall present temperature results for the velocity dispersion which is calculated using the Jeans equation so as to be conservative.

Using the method described before, we calculate the final temperatures of our neutron star at different galactic radii, starting with $r_{\rm GC} = 10^{-5}$ pc and going outwards through the halo up to a radius of 50 kpc. For every DM

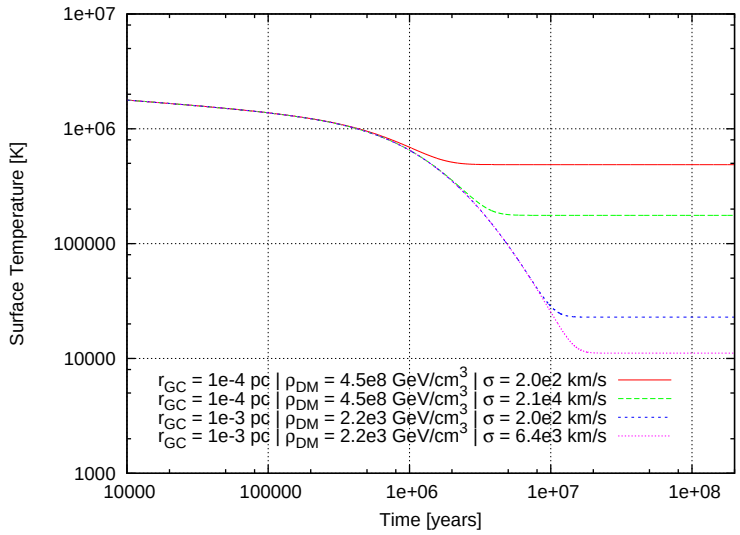

Figure 7.2: Evolution of the surface temperature of a $1.44\ M_{\odot}$ neutron star situated at two different galactic radii. The plot is for Dark Matter with a mass $m_{\chi} = 10$ GeV and a scattering cross section of $\sigma_0 = 1.5 \times 10^{-41}$ cm^2. We compare here the approximate constant velocity dispersion ($\sigma \equiv \bar{v} = 200$ km/s) with the effective velocity dispersion deduced from the static radial Jeans equation.

density profile and for every type of DM particle, we get a specific curve. As we said, however, the relation between the various sets of solutions is rather straightforward, since the temperature gradient varies as: $dT/dt \propto Cm_{\chi}$. Note that the results obtained so far do not depend much on m_{χ} since $C \propto 1/m_{\chi}$. For non-relativistic accretion the dependence on the mass might be more pronounced since the kinematics of individual collisions would depend on the ratio between the nucleon mass and the Dark Matter particle. For the case of neutron stars however any such dependency will be suppressed since the kinetic energy of the Dark Matter particle will be much larger and any small recoil in the neutron star will result in the particle being captured.

In the most favourable cases in terms of DM properties and distribution, the highest surface temperatures one can possibly obtain lie around 10^6 K near the Galactic Centre (Fig. 7.3).

7.1.1 Density Profiles with Central Spikes

In all our calculations so far we have been considering straightforward Einasto profiles without taking too much care about the complex astrophysical phenomena occurring near the Galactic Centre on a sub-parsec scale. The formation of a super massive black hole is thought to enhance the density in this central region [115] and this combined with effects such as self-annihilation, gravitational scattering of DM particles by stars and capture in the supermassive black hole must be included if one wishes to obtain a more realistic picture of this central region.

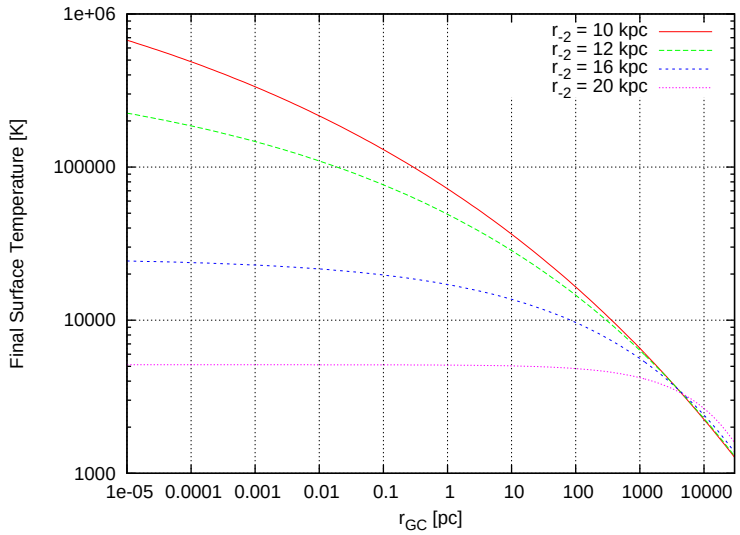

Figure 7.3: Final surface temperature of the neutron star (at late times) for different DM density distributions, with $m_\chi = 10$ GeV and $\sigma_0 = 1.5 \times 10^{-41}$ cm^2.

It is interesting to evaluate the possible consequences of considering much higher DM densities at small radii. To do so, we take as a benchmark the density profiles presented in [76] and we extract a few values in order to determine the evolution of the surface temperature (Fig. 7.4). One can observe that, in the most extreme situations, the neutron star manages to keep its surface temperature well above 10^6 K at late times if it is situated at less than one thousandth of a parsec from the central black hole. Since there have been a large number of compact objects observed by the Chandra X-ray telescope in this central region [116], this might prove interesting in the future.

7.1.2 Observational Situation

It is a challenge for astronomers to observe the thermal emission from neutron stars due to their very small surface area and luminosity. Rather than attempting to provide a complete review of this complicated subject we will mention a couple of examples of relatively cool neutron stars which have been observed.

Confrontation with Two Observed Pulsars

Pulsar PSR J0108-1431 is a nearby pulsar located between 100 and 200 pc from the Solar System. The spin down age suggests that this object is older than 10^8 years so that its surface will have had a long time to cool. Indeed, observations suggest that the surface temperature is a very low $T_{eff} < 9 \times 10^4$ K if the distance is 200 pc or $T_{eff} < 5 \times 10^4$ K if the pulsar is located at a distance of 130 pc [117]. Comparison with Fig. 6.8 shows that even this very low temperature is too high to betray underlying heating by Dark Matter, probably by around an order of magnitude.

Pulsar PSR J0437-4715 is a much older object with a spin down age of

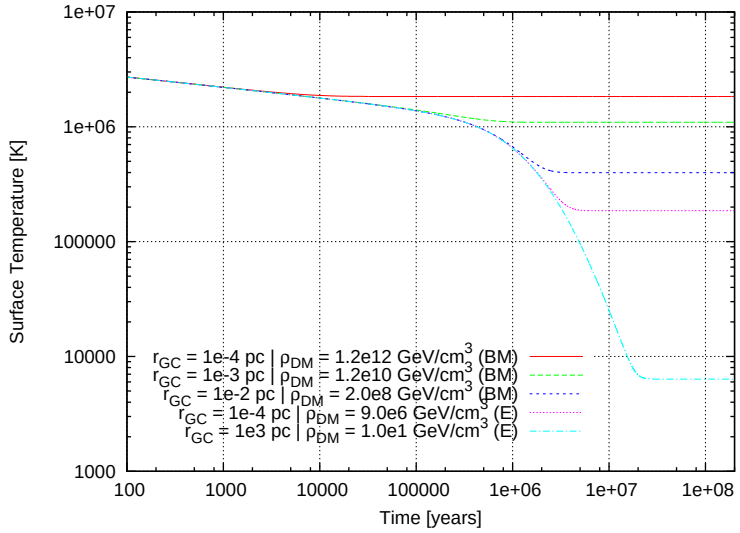

Figure 7.4: Evolution of the surface temperature of a $1.44\ M_\odot$ neutron star situated at various galactic radii (cf. legend in figure). The plot is for Dark Matter with a mass $m_\chi = 10$ GeV and a scattering cross section of $\sigma_0 = 1.5 \times 10^{-41}$ cm^2. The DM densities are deduced from two models: profiles obtained by Bertone & Merritt in [76] (BM) and Einasto profiles (E).

nearly 5 Gyr, yet its surface temperature is slightly higher than that of J0108-1431 [117]. It seems to be challenging to explain this relatively high surface temperature (for its age) and it has been suggested that the explanation may lie in internal heating [118]. Unfortunately, it does not seem that this internal heating comes from Dark Matter since in order for this to be the case we would require a density of Dark Matter much larger than what is expected in this region of the galaxy (PSR J0437-4715 lies only about 130 pc from the Solar System). Also, if we were to explain the temperature of this object using Dark Matter, we would also expect a similar temperature for PSR J0108-1431.

Further Observations

If it were possible to extend observations in the future to lower temperatures and we were able to find a neutron star with a temperature $\sim 10^4$ K, then the situation would become much more interesting. A temperature of 10^4 K is about as low as could be possible for the very oldest neutron stars which exist. If such a low temperature neutron star was observed this would tell us that any combination of Dark Matter density and cross section which predicts a temperature higher than this at the solar radius in the galaxy is ruled out.

As we have shown, we can expect higher temperatures for neutron stars which lie at the centre of the galaxy because of the larger accretion rates in that region. It is however difficult to see into the centre of the galaxy. In fact the very centre is obscured by dust [136] and as we move upwards in frequency through the electromagnetic spectrum, we find the centre of the galaxy becomes invisible in the infra-red, only to return into view in the X-ray part of the spectrum. Since this rules out the possibility of viewing objects with temperatures less than many

millions of degrees, the observational situation becomes more complicated (not to mention the three orders of magnitude drop in luminosity relative to local neutron stars simply due to distance). We may be able to see a very hot neutron star lying at the Galactic Centre, but it would be necessary to find some reliable way of dating the object to a relatively high precision in order to establish that this heating is anomalous and caused by Dark Matter.

From these considerations, it is clear that the conclusion largely depends on the assumptions made about the DM distribution in the Milky Way. Nevertheless, there is a small hope that the most extreme configurations might be tested through observations.

Therefore, our chances of using neutron stars as Dark Matter probes through the method described above are non-zero but limited. There exists however an alternative way of benefiting from the high accretion power of these very dense objects if we assume that DM particles do not co-annihilate with each other.

7.2 Non-Annihilating Dark Matter

We have been studying so far the consequences of accreting co-annihilating Dark Matter particles onto neutron stars. Assuming co-annihilation properties is however a restriction, though motivated by theoretical arguments. That is why, in the present Section, we propose to widen our perspectives by analysing the consequences of accreting non-annihilating DM particles onto the same objects.

After a short presentation of the characteristics of non-annihilating Dark Matter, we will discuss two expected outcomes (in Section 7.2.2) and describe the possible observational consequences.

7.2.1 Non-Annihilating Dark Matter Candidates

There exist several models where Dark Matter does not annihilate with itself. Such situation could arise if DM is for example made of fermions, but there would not exist the corresponding antifermions; or DM could consist of bosons characterised by one sign of an additive conserved quantum number, but without trace of the particle having the opposite sign. Within the following paragraphs, some of these alternative models are briefly depicted.

Technibaryons

Modelled on quantum chromodynamics[1], technicolor theories [119] belong to the class of physical models beyond the Standard Model. Their aim is to address electroweak symmetry breaking in order to account for a mechanism that provides mass to elementary particles. It has been shown [120, 121, 122, 123] that models can be successfully built in which particular bound states of technifermions, known as technibaryons, are stable enough to survive the evolution of the Universe. These baryons naturally appear in technicolor theories which are not ruled out by the electroweak precision measurements [124, 125, 126, 127], and represent convincing Dark Matter candidates.

[1] Being an important part of the Standard Model of particle physics, quantum chromodynamics (QCD) is a theory of the strong interaction (or *color* force); it describes the interactions of the quarks and gluons forming hadrons such as the neutron and the proton.

The type of technicolor theory determines the range of the technibayon's mass: in the case of a low-scale theory (i.e. if the decay constant is much smaller than the electroweak scale $F \ll F_{\mathrm{EW}}$), its mass should not be higher than a few TeV; otherwise, it could be much heavier. As a DM candidate, the technibaryon has to be electrically neutral and satisfy constraints on its abundance. Given the limits imposed by other experiments on the DM-nucleon cross section, it may have to be electroweak neutral as well. The early type of technicolor DM candidates may prove hard to produce at the CERN's Large Hadron Collider (LHC), but a new, lighter type has been suggested [128, 129], which could be more easily accessible.

Mirror Dark Matter

The idea of a "mirror" world appeared in particle physics when parity violation[2] became a conceptual issue. It was first proposed in the 1950s in order to solve the $\tau - \theta$ puzzle [130] and was later more thoroughly formulated [131] in order to restore parity symmetry in nature. Mirror particles are identical to standard particles, except in the fact that their interactions are right-handed. This property allows for a restoration of the apparently broken symmetry, provided that a mirror particle exists for every ordinary one. The parity symmetry remains broken, however, if the masses of the corresponding particles differ.

Mirror particles interact among themselves in the same way as ordinary particles, but would reveal their presence around normal matter only through gravity and very weak interactions. That is the reason why they have been suggested as candidates for the inferred Dark Matter in the Universe [132, 133, 134].

Mirror Dark Matter could have to required density profile in order to account for the flat rotation curve observed in galaxies (see Subsection 5.1.2). If we assume that the halo of DM surrounding a galaxy is mainly made of a spherically symmetric self gravitating gas in hydrostatic equilibrium, its distribution will obey [135]

$$\frac{dP}{dr} = -\rho g(r), \tag{7.1}$$

where P is the pressure and $g(r)$ is the local acceleration at a radius r. For a dilute gas, the pressure is related to the mass density, ρ, via $P = \rho T/(\mu M_p)$, where μM_p is the average mass of the particles in the gas (M_p being the proton mass). The local acceleration can be simply expressed in terms of the energy density:

$$g(r) = \frac{G}{r^2}\int_o^r \rho 4\pi r'^2 dr', \tag{7.2}$$

where G is the gravitational constant.

The solution of Eq. (7.1) and (7.2) is $\rho \propto 1/r^2$:

$$\rho = \frac{\lambda}{r^2},$$

$$T = G\lambda 2\pi\mu M_p.$$

[2] Elementary particles respect rotation and translation symmetries, but not symmetry caused by mirror reflection (known as P-symmetry or parity), through weak interactions.

The rotational velocity at a radial coordinate r , $v_{rot}(r)$, can be obtained from $v_{rot}^2/r = g(r)$, which implies:

$$v_{rot}^2(r) = \frac{G}{r}\int_0^r \rho 4\pi r'^2 dr' = G\lambda 4\pi,$$

which corresponds to the expected asymptotically flat rotation curve.

7.2.2 Constraints on the $\sigma_0 - m_\chi$ Plan

In the search for Dark Matter, the absence of detection in an experimental set up does not necessarily mean absence of information concerning the DM particles. Indeed, knowing the experimental conditions and the theoretical assumptions made, it is possible to interprete a null detection as an additional piece of knowledge about the DM properties.

The common way to translate this knowledge is through the mapping of the parameter space showing the possible DM particle-nucleon scattering cross section, σ_0, with respect to the mass of the DM particle, m_χ. On this $\sigma_0 - m_\chi$ plan, the experimental limit set by the absence of detection will be drawn as a line delimiting the lower border of an exclusion zone, i.e. a region of the parameter space in which the DM particles should not be found. In the following paragraphs, we will explain how building up non-annihilating DM particles in a neutron star allows us to put new constraints on the DM parameter space.

Degenerate Fermionic Matter

In the case of non-annihilating DM particles, there would be no heating of the neutron star due to annihilation - the neutron star would simply accrete DM in its core. If the amount of Dark Matter in the core were to increase without limit, there would be various possible outcomes. In the case of fermionic Dark Matter and in the absence of any pressure due to the exchange of gauge bosons, the density would increase until Fermi statistics starts to play a role. When this occurs, the Dark Matter core would develop the equation of state of non-relativistic degenerate fermionic matter, $P \propto \rho^{5/3}$.

In order to calculate the effect of such a degenerate Dark Matter core upon the neutron star, the correct thing to do would be to simultaneously solve the Oppenheimer-Volkoff equation for the two stars co-located on top of each other and therefore both contributing to the gravitational field relevant for the solution. We have obtained such solutions, and have confirmed that when there is a large mass contribution due to a degenerate Dark Matter core existing in the star, the normal mass-radius and indeed maximum mass of the neutron star that can be obtained varies.

Chandrasekhar Limit

In practice, the amount of Dark Matter which needs to be added to the core of the neutron star for this to happen is typically far in excess of the Chandrasekhar mass ($M_{\rm Ch}$) corresponding to the degenerate Dark Matter star for all but the lightest Dark Matter candidates. At this critical point, the degeneracy pressure of Dark Matter would become relativistic and the degenerate Dark Matter core would become unstable. Gravitational collapse of the Dark Matter core would

occur, creating a black hole at the centre of the neutron star, resulting in the neutron matter also becoming unstable.

The black hole thus created would swallow the neutron star entirely. This is a particularly intriguing possibility not simply for its inherent drama but also because it could in principle provide an additional explanation of the unexplained gamma ray bursts observed in the Universe other than the coalescence of a neutron star with another compact object. It would therefore be interesting if enough Dark Matter could be accreted for reasonable values of the relevant parameters - namely the density of Dark Matter in the places where neutron stars reside, the mass of the Dark Matter and its cross section for scattering off nuclei.

Resulting Limits on the $\sigma_0 - m_\chi$ Plan

Fixing the accretion time available for the neutron star to capture DM particles, one can determine, for a given m_χ, the cross section needed to accrete a mass equivalent to $M_{\rm Ch}(m_\chi)$ which is the amount of accreted Dark Matter required to instigate the collapse of the neutron star. This procedure allows us to pick out regions on the $\sigma_0 - m_\chi$ plane where this could occur (Fig. 7.5). We assume that the Chandrasekhar limit is of the order of

$$M_{\rm Ch} \approx M_{\rm Pl}^3/m_\chi^2$$

and we consider three accretion times: 10^6, 10^8 and 10^{10} years, corresponding roughly to 0.01%, 1% and 100% of the age of the Universe respectively. We also consider two different densities 10^{11} and 10^5 GeV cm^{-3}. The higher density 10^{11} GeV cm^{-3} is the rather extreme limit of the predictions of Bertone and Merritt for non-annihilating Dark Matter in a central spike.

Since we consider the limiting effective cross section given by the geometrical cross section of the neutron star ($\sigma_0^{\rm max} = 2\times10^{-45}$ cm^2), there exists a minimum value for the DM particle mass below which the fixed accretion time is too short for the star to accrete $M_{\rm Ch}$. The corresponding limiting σ_0 is shown on the graph by the upper cut-off at high cross sections. It is possible to see that in the most extreme case, namely a neutron star immersed in a density of 10^{11} GeV cm^{-3} for 10^{10} years do we obtain results which are approaching the region of interest for direct detection experiments.

The cross sections required become much smaller for higher Dark Matter masses since much fewer of these particles need to be accreted to reach their correspondingly smaller Chandrasekhar mass limit. The change in the slope of the line at high masses can be understood in the following way:

- The typical energy exchanged in a recoil of a Dark Matter particle with a nucleon goes like $m_{nuc}v^2$ for $m_\chi \gg m_{nuc}$.
- When a 10^3 GeV mass Dark Matter particle travelling at 200 km s^{-1} falls onto a neutron star, its velocity increases to close to the speed of light and the energy exchanged in this collision is much larger than the total kinetic energy the particle had at infinity. Such a particle will lose so much energy in the kick it will almost certainly be captured by the neutron star.
- For a much more massive particle this is no longer true and it will have a lower probability of being captured due to a single scatter, hence the different slope at higher energies.

The above reasoning is the physical interpretation of the reality described by the accretion rate equations 2.18 around the critical value of $m_\chi = 10^6$ GeV. The change of behaviour occuring around $m_\chi \approx 10^6$ GeV is caused by the fact that, at this point, $\chi(A_-, A_+)$ becomes comparable to $\chi(-\eta, \eta)$. More precisely, the change is observed when $A \approx \eta$, which means for a Dark Matter mass resulting in

$$\left(\frac{3v^2(r)\mu}{2\bar{v}^2\mu_-^2}\right)^{1/2} \approx \left(\frac{3v_\star^2}{2\bar{v}^2}\right)^{1/2}, \text{ or}$$

$$\frac{\mu}{\mu_-^2} \approx \left(\frac{v_\star}{v(r)}\right)^2.$$

Considering that $\mu = m_\chi/M_n \gg 1$ at this regime, then we obtain

$$\frac{4}{\mu} \approx \left(\frac{v_\star}{v(r)}\right)^2$$

and the corresponding mass for the DM particle is

$$m_\chi \approx M_n \left(\frac{2v(r)}{v_\star}\right)^2.$$

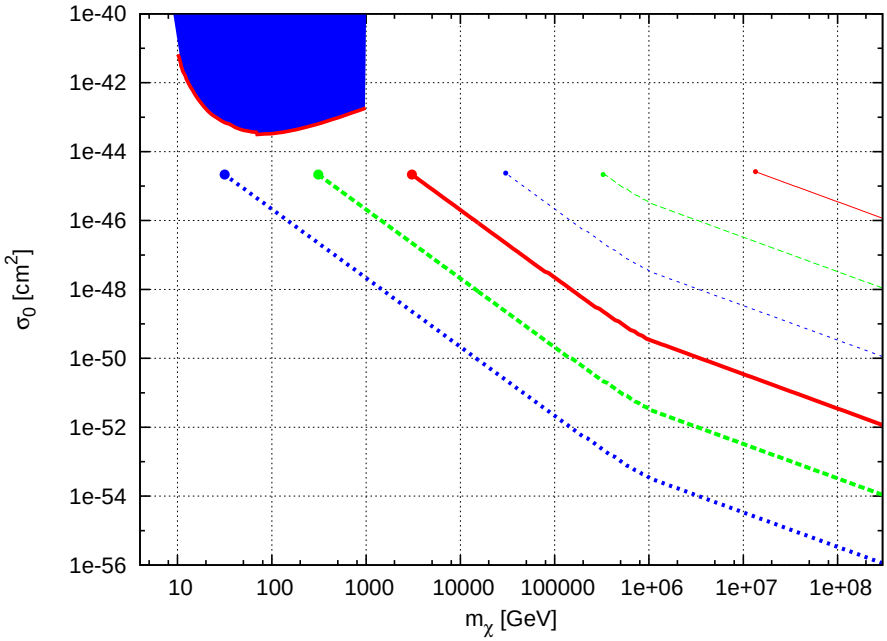

Figure 7.5: Neutron stars immersed for long enough in a high enough density of non-annihilating Dark Matter will eventually accumulate the amount of DM particles which correspond to the Chandrasekhar limit M_{Ch} and collapse. The red solid lines here correspond to the cross section σ_0 and mass m_χ required to cause collapse after 10^6 years. The green longer dashed lines correspond to 10^8 years and the blue shorter dashed lines correspond to 10^{10} years. The thicker the line the higher the density - we plot two lines for each duration of time corresponding to 10^{11} and 10^5 GeV cm^{-3}. The upper right region of each line is excluded since the conditions in this region would give rise to a black hole. The curved line corresponds to the latest data from the CDMS experiment (assuming a velocity dispersion $\bar{v} = 230$ km/s and $\rho_{\mathsf{DM}} = 0.3$ GeV/cm^3) to place the results in context. The change in the slope of the lines around 10^6 GeV is explained in Subsection 7.2.2.

Chapter 8

Conclusions

The search for Dark Matter particles has kept busy a large number of scientists during the past two decades and will remain an important part of experimental endeavours in the next 10 years. Many clever devices, some of which were described in the previous Chapters, have been designed in order to understand the true nature of this elusive though essential component of our Universe. In this conclusive Chapter, we propose to summarise our approach, synthetise the main results obtained and open up the discussion on future prospects in the domain.

In the present study, we have investigated whether or not it would ever be possible to use the accretion of Dark Matter onto neutron stars in order to better understand the properties of Dark Matter. In order to draw a consistent picture and guaranty the meaningfulness of our conclusions, we took care to properly define and quantify the various parameters involved in the DM accretion process. This included, among others, a good understanding of the physics of neutron stars and a detailed modelling of the DM density distribution in our galaxy.

8.1 Annihilating Dark Matter: Some Hope of Detection

We first looked at the effects of annihilating Dark Matter on the temperature of the neutron stars. As can be seen in Fig. 7.3, the highest final surface temperatures which could be caused by the heating of neutron stars with Dark Matter lie around

$$T_{\max} = 5 \times 10^5 \text{ K}$$

even in the most optimistic circumstances (at $r_{GC} = 10^{-4}$ pc, for $m_\chi = 10$ GeV, $\sigma_0 = 1.5 \times 10^{-41}$ cm^2 and using $r_{-2} = 10$ kpc). If we consider a pessimistic variable velocity dispersion calculated using Jeans equation and rising towards the centre of the galaxy, the final temperature drops to 1.8×10^5 K. Given the surface area of the neutron stars, these values would produce luminosities in the vicinity of

$$L \approx 10^{-2}\, L_\odot,$$

respectively $2 \times 10^{-4}\ L_\odot$ with variable velocity dispersion, with a peak wavelength at about 6 nm (16 nm), corresponding to a frequency of about 50 PHz (18

PHz). These sources would thus radiate mainly in the range between extreme ultraviolet (UV) and soft X-rays. Given the important absorption due to dust between us and the centre of our galaxy and the presence of other luminous X-ray sources in this region, we believe that the objects in question would prove rather tricky to detect.

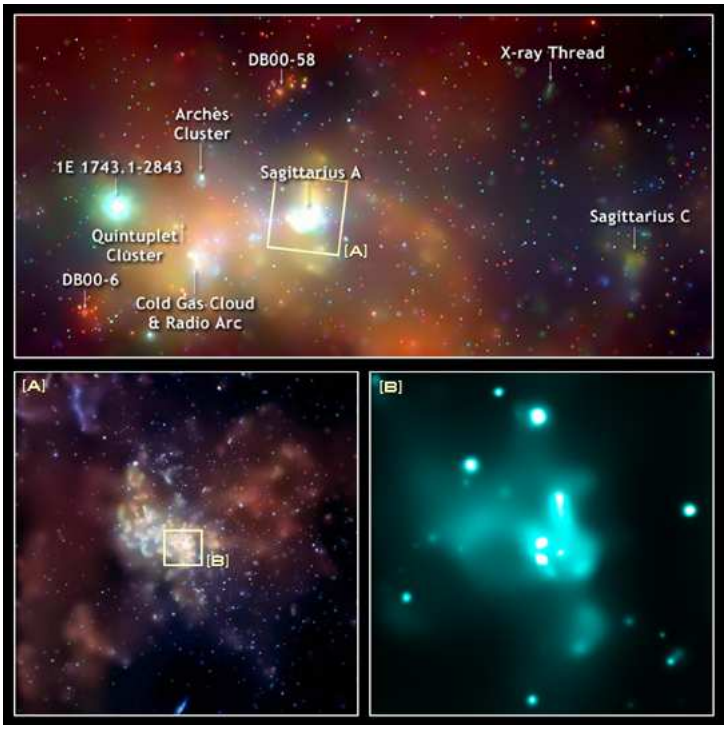

Figure 8.1: Chandra X-ray images of the Galactic Centre region; the bottom right panel is centred on Sgr A*, the central Super Massive Black Hole. [Credit: NASA/Chandra/UMass]

8.2 Non-Annihilating Dark Matter: Constraints on $\sigma_0 - m_\chi$

Perhaps more interesting are the constraints on non-annihilating Dark Matter which come from the fact that if enough of such Dark Matter were to accumulate onto a neutron star it would form a degenerate star at the centre. If this internal star were to get too large, it could reach its own Chandrasekhar mass, which is smaller than that of the neutron star since the Dark Matter mass is greater than the nucleon mass in most models.

In the event of the mass of Dark Matter in the star reaching the Chandrasekhar mass of the star, the Dark Matter would lead to the collapse of the neutron star which collected it. Such an event might happen for the kind of values of Dark Matter mass and cross section currently being probed by direct detection experiments but only in regions of extremely high density. On the

other hand, for higher mass Dark Matter particles, required cross sections are much smaller, since a much smaller mass of Dark Matter would need to be accumulated in order for collapse to occur.

The idea that the accretion of stable Dark Matter could be responsible for the collapse of neutron stars is very exciting, in this part of our thesis we have quantified how likely that is. For low mass Dark Matter particles, it seems extremely unlikely, since we would need DM densities of the order of 10^{11} GeV/cm^3 in order to put significant constraints on the $\sigma_0 - m_\chi$ plane.

8.3 Research Perspectives

Using neutron stars to probe Dark Matter proves meaningful and many projects have been developed around this idea. Among these projects, two important categories emerge: exploring the formation of dark or strange stars [138, 139, 140], or constraining particular types of Dark Matter [141, 142, 143, 144, 145].

In [139], the authors investigate the formation of strange quark matter inside neutron stars. Using the self-annihilation mechanism of WIMPs, they estimate that, for DM particles in the range $m_\chi \gtrsim 4$ GeV/c^2, the energy generated by the WIMP annihilation would be sufficient to burn nucleon matter into a long-lived strange quark matter that would trigger the conversion of the whole neutron star into a strange star. This conversion process could be the cause of the emission of powerful γ-ray bursts (GRBs) and could therefore present observational consequences.

In their letter [145], Kouvaris and Tinyakov propose to use old neutron stars observations in order to put constraints on non-interacting or weakly interacting Dark Matter. Developing on the scenario of black hole formation inside neutron stars, they come to the conclusion that light non-annihilating bosonic DM candidates were excluded from the mass range 2 keV to 16 GeV. Furthermore, they were able to exclude large zones on the DM parameter space in the case of repulsive self-interactions, completing the constraints provided by observations of the Bullet Cluster.

Research of Dark Matter based on the study of compact objects will probably continue strongly in the near future, as these objects offer interesting conditions to investigate the nature of this still mysterious component of the Universe.

Bibliography

[1] P. J. E. Peebles, "The Standard Cosmological Model," in Les Rencontres de la Vallee d'Aosta (1998), ed. M. Greco.

[2] A. L. Maroto and J. Ramirez, "A Conceptual Tour About the Standard Cosmological Model," arXiv:astro-ph/0409280 (2004).

[3] D. Scott, "The Standard Cosmological Model," arXiv:astro-ph/0510731 (2005).

[4] H. Bondi and T. Gold, "The Steady-State Theory of the Expanding Universe," Mon. Not. Roy. Astron. Soc. **108**, 252 (1948).

[5] F. Hoyle, "A New Model for the Expanding Universe," Mon. Not. Roy. Astron. Soc. **108**, 372 (1948).

[6] F. Zwicky, "Die Rotverschiebung von extragalaktischen Nebeln," Helv. Phys. Acta **6**, 110 (1933).

[7] L. Bergstrom, "Non-baryonic Dark Matter: Observational evidence and detection methods," Rept. Prog. Phys. **63**, 793 (2000) [arXiv:hep-ph/0002126].

[8] G. Bertone, D. Hooper and J. Silk, "Particle Dark Matter: evidence, candidates and constraints," Phys. Rep. **405**, 279 (2005) [arXiv:hep-ph/0404175].

[9] L. Volders, "Neutral hydrogen in M 33 and M 101," Bull. of the Astron. Instòf the Neth. **14**, 323 (1959).

[10] N. A. Bahcall and X. Fan, "The Most Massive Distant Clusters: Determining Omega and delta 8," Astrophys. J. **504**, L29 (1998) [arXiv:astro-ph/9803277].

[11] R. G. Carlberg *et al.*, "The $\Omega_M - \Omega_\Lambda$ Dependence of the Apparent Cluster Ω," Astrophys. J. **516**, 552 (1999).

[12] A. Kashlinsky, "Determining Omega from the cluster correlation function," Phys. Rep. **307**, 67 (1998) [arXiv:astro-ph/9806236].

[13] K. G. Begeman, A. H. Broeils and R. H. Sanders, "Extended rotation curves of spiral galaxies - Dark haloes and modified dynamics," Mon. Not. Roy. Astron. Soc. **249**, 523 (1991).

[14] J. A. Tyson, G. P. Kochanski and I. P. dell'Antonio, "Detailed Mass Map of CL 0024+1654 from Strong Lensing," Astrophys. J. Lett. **498**, L107 (1998).

[15] W. H. Tucker, H. Tananbaum and R. A. Remillard, "A search for 'failed clusters' of galaxies," Astrophys. J. **444**, 532 (1995).

[16] M. Markevitch *et al.*, "Direct Constraints on the Dark Matter Self-Interaction Cross Section from the Merging Galaxy Cluster 1E 0657-56," Astrophys. J. **606**, 819 (2004) [arXiv:astro-ph/0309303].

[17] D. Clowe *et al.*, "A direct empirical proof of the existence of Dark Matter," Astrophys. J. **648**, L109 (2006) [arXiv:astro-ph/0608407].

[18] W. Hu, N. Sugiyama and J. Silk, "The Physics of Microwave Background Anisotropies," arXiv:astro-ph/9604166 (1996).

[19] W. Hu and S. Dodelson, "Cosmic Microwave Background Anisotropies," Ann. Rev. of Astron. & Astrophys. **40**, 171 (2002) [arXiv:astro-ph/0110414].

[20] A. A. Penzias and R. W, Wilson, "A Measurement of Excess Antenna Temperature at 4080 Mc/s," Astrophys. J. **142**, 419 (1965).

[21] E. Komatsu *et al.*, "Seven-year Wilkinson Microwave Anisotropy Probe (WMAP) Observations: Cosmological Interpretation," Astrophys. J. Suppl. **192**, 18 (2011) [arXiv:1001.4538 [astro-ph.CO]].

[22] V. Mukhanov, "Physical Fundations of Cosmology", Chap. 9, Camb. U. Press (2008).

[23] K. A. Olive, "TASI Lectures on Dark Matter," arXiv:astro-ph/0301505 (2003).

[24] J. L. Feng, "Dark Matter Candidates from Particle Physics and Methods of Detection," Annu. Rev. Astron. Astrophys. **48**, 495 (2010) [arXiv:1003.0904 [astro-ph.CO]].

[25] CDMS Collaboration, "Search for Weakly Interacting Massive Particles with the First Five-Tower Data from the Cryogenic Dark Matter Search at the Soudan Underground Laboratory," Phys. Rev. Lett. **102**, 011301 (2009) [arXiv:0802.3530 [astro-ph]].

[26] CoGeNT Collaboration, "Experimental constraints on a Dark Matter origin for the DAMA annual modulation effect," Phys. Rev. Lett. **101**, 251301 (2008) [arXiv:0807.0879 [astro-ph]].

[27] XENON100 Collaboration, "First Dark Matter Results from the XENON100 Experiment," Phys. Rev. Lett. **105**, 131302 (2010) [arXiv:1005.0380 [astro-ph.CO]].

[28] R. J. Gaitskell, V. Mandic and J. Filippini, http://dmtools.brown.edu (2010).

[29] M. Fujii and T. Yanagida, "A solution to the coincidence puzzle of Ω_B and Ω_{DM}," Phys. Lett. B **542**, 80 (2002) [arXiv:hep-ph/0206066].

[30] R. Kitano and I. Low, "Dark matter from baryon asymmetry," Phys. Rev. D **71**, 023510 (2005) [arXiv:hep-ph/0411133].

[31] G. R. Farrar and G. Zaharijas, "Dark Matter and the Baryon Asymmetry of the Universe," Phys. Rev. Lett. **96**, 041302 (2006) [arXiv:hep-ph/0510079].

[32] DAMA Collaboration (R. Bernabei *et al.*), "Search for WIMP annual modulation signature: Results from DAMA/NaI-3 and DAMA/NaI-4 and the global combined analysis," Phys. Lett. B. **480**, 23 (2000).

[33] C. Savage *et al.*, "Compatibility of DAMA/LIBRA dark matter detection with other searches," Journ. of Cosm. and Astropart. Phys. **4**, 10 (2009) [arXiv:0808.3607 [astro-ph]].

[34] F. J. Petriello and K. M. Zurek, "DAMA and WIMP dark matter," Journ. of High En. Phys. **9**, 47 (2008) [arXiv:0806.3989 [hep-ph]].

[35] C. Savage, K. Freese, P. Gondolo and D. Spolyar, "Compatibility of DAMA/LIBRA dark matter detection with other searches in light of new galactic rotation velocity measurements," Journ. of Cosm. and Astropart. Phys. **9**, 36 (2009) [arXiv:0901.2713 [astro-ph.CO]].

[36] B. Kiziltan, A. Kottas and S. E. Thorsett, "The Neutron Star Mass Distribution," arXiv:1011.4291 [astro-ph].

[37] F. Özel, G. Baym and T. Güver, "Astrophysical measurement of the equation of state of neutron star matter," Phys. Rev. D **82**, 101301 (2010) [arXiv:1002.3153 [astro-ph]].

[38] M. D. Young, R. N. Manchester and S. Johnston, "A radio pulsar with an 8.5-second period that challenges emission models," Nature **400**, 848 (1999).

[39] Z. Ahmed *et al.* [The CDMS-II Collaboration], "Results from the Final Exposure of the CDMS II Experiment," arXiv:0912.3592 [Unknown].

[40] J. Angle *et al.* [XENON Collaboration], Phys. Rev. Lett. **100**, 021303 (2008) [arXiv:0706.0039 [astro-ph]].

[41] V. N. Lebedenko *et al.*, "Result from the First Science Run of the ZEPLIN-III Dark Matter Search Phys. Rev. D **80**, 052010 (2009) [arXiv:0812.1150 [astro-ph]].

[42] S. Nussinov, "Technocosmology: Could A Technibaryon Excess Provide A 'Natural' Missing Phys. Lett. B **165**, 55 (1985).

[43] D. B. Kaplan, "A Single explanation for both the baryon and Dark Matter densities," Phys. Rev. Lett. **68**, 741 (1992).

[44] D. Hooper, J. March-Russell and S. M. West, "Asymmetric sneutrino Dark Matter and the Omega(b)/Omega(DM) puzzle," Phys. Lett. B **605**, 228 (2005) [arXiv:hep-ph/0410114].

[45] G. D. Kribs, T. S. Roy, J. Terning and K. M. Zurek, "Quirky Composite Dark Matter," arXiv:0909.2034 [hep-ph].

[46] E. W. Kolb, D. J. H. Chung and A. Riotto, "WIMPzillas!," arXiv:hep-ph/9810361.

[47] DAMA Collaboration (R. Bernabei *et al.*), "First results from DAMA/LIBRA and the combined results with DAMA/NaI," Eur. Phys. J. C **56** (2008) 333 [arXiv:0804.2741 [astro-ph]].

[48] C. E. Aalseth *et al.* [CoGeNT collaboration], "Results from a Search for Light-Mass Dark Matter with a P-type Point Contact Germanium Detector," arXiv:1002.4703 [astro-ph.CO].

[49] M. T. Frandsen and S. Sarkar, "Asymmetric Dark Matter and the Sun," arXiv:1003.4505 [Unknown].

[50] A. Bouquet, J. Kaplan, F. Martin and P. Salati, "Wimps And Stellar Structure," A. Bouquet and P. Salati, "Capture And Equilibrium Of Cosmions In Stars,"

[51] D. Spolyar, K. Freese and P. Gondolo, "Dark matter and the first stars: a new phase of stellar evolution," Phys. Rev. Lett. **100**, 051101 (2008) [arXiv:0705.0521 [astro-ph]].

[52] M. Fairbairn, P. Scott and J. Edsjo, "The Zero Age Main Sequence of WIMP burners," Phys. Rev. D **77**, 047301 (2008) [arXiv:0710.3396 [astro-ph]].

[53] P. Scott, M. Fairbairn and J. Edsjo, "Dark stars at the Galactic Centre - the main sequence," Mon. Not. Roy. Astron. Soc. **394**, 82 (2008) [arXiv:0809.1871 [astro-ph]].

[54] F. Iocco, A. Bressan, E. Ripamonti, R. Schneider, A. Ferrara and P. Marigo, "Dark matter annihilation effects on the first stars," Mon. Not. Roy. Astron. Soc. **390**, 1655 (2008) [arXiv:0805.4016 [astro-ph]].

[55] M. Taoso, G. Bertone, G. Meynet and S. Ekstrom, "Dark Matter annihilations in Pop III stars," Phys. Rev. D **78** (2008) 123510 [arXiv:0806.2681 [astro-ph]].

[56] I. V. Moskalenko and L. L. Wai, "Dark matter burners," Astrophys. J. **659** (2007) L29 [arXiv:astro-ph/0702654].

[57] C. Kouvaris, "WIMP Annihilation and Cooling of Neutron Stars," Phys. Rev. D **77**, 023006 (2008) [arXiv:0708.2362 [astro-ph]].

[58] M. McCullough and M. Fairbairn, "Capture of Inelastic Dark Matter in White Dwarves," arXiv:1001.2737 [hep-ph].

[59] F. Sandin and P. Ciarcelluti, "Effects of mirror Dark Matter on neutron stars," arXiv:0809.2942 [astro-ph].

[60] G. Bertone and M. Fairbairn, "Compact Stars as Dark Matter Probes," Phys. Rev. D **77**, 043515 (2008) [arXiv:0709.1485 [astro-ph]].

[61] I. Goldman and S. Nussinov, "WEAKLY INTERACTING MASSIVE PARTICLES AND NEUTRON STARS," Phys. Rev. D **40**, 3221 (1989).

[62] A. Gould, B. T. Draine, R. W. Romani and S. Nussinov, "NEUTRON STARS: GRAVEYARD OF CHARGED DARK MATTER," Phys. Lett. B **238**, 337 (1990).

[63] D. Tucker-Smith and N. Weiner, "Inelastic Dark Matter," Phys. Rev. D **64**, 043502 (2001) [arXiv:hep-ph/0101138].

[64] S. Nussinov, L.-T. Wang and I. Yavin, "Capture of Inelastic Dark Matter in the Sun," JCAP **0908**, 037 (2009) [arXiv:0905.1333 [hep-ph]].

[65] A. Gould, "Resonant Enhancements In Wimp Capture By The Earth," Astrophys. J. **321** (1987) 571.

[66] R. C. Tolman, "Effect of Inhomogeneity on Cosmological Models," Proceed. of the NAS **20**, 169 (1934).

[67] J. R. Oppenheimer and G. M. Volkoff, "On Massive Neutron Cores," Phys. Rev. **55**, 374 (1939).

[68] R. C. Tolman, "Relativity, Thermodynamics and Cosmology," Clarendon Press (Oxford, 1950).

[69] A. Akmal, V. R. Pandharipande and D. G. Ravenhall, "The equation of state for nucleon matter and neutron star structure," Phys. Rev. C **58**, 1804 (1998) [arXiv:nucl-th/9804027].

[70] P. Haensel and A. Y. Potekhin, "Analytical representations of unified equations of state of neutron-star Astron. Astrophys. **428** (2004) 191 [arXiv:astro-ph/0408324].

[71] J. S. Clark, S. P. Goodwin, P. A. Crowther, L. Kaper, M. Fairbairn, N. Langer and C. Brocksopp, "Physical parameters of the high-mass X-ray binary 4U1700-37," Astron. Astrophys. **392**, 909 (2002) [arXiv:astro-ph/0207334].

[72] J. F. Navarro, C. S. Frenk and S. D. M. White, Astrophys. J. **462**, 563 (1996) [arXiv:astro-ph/9508025].

[73] B. Moore *et al.*, "Resolving the Structure of Cold Dark Matter Halos", Astrophys. J. **499**, L5 (1998) [arXiv:astro-ph/9709051v2].

[74] B. Moore *et al.*, "Cold Collapse and the Core Catastophe", Mon. Not. Roy. Astron. Soc. **310**, 1147 (1999) [arXiv:astro-ph/9903164].

[75] S. M. Kent, "Dark matter in spiral galaxies. I - Galaxies with optical rotation curves", Astrophys. J. **91**, 1301 (1986).

[76] G. Bertone and D. Merritt, "Time-dependent models for Dark Matter at the Galactic Center," Phys. Rev. D **72**, 103502 (2005) [arXiv:astro-ph/0501555].

[77] D. Merritt, J. F. Navarro, A. Ludlow and A. Jenkins, "A Universal Density Profile for Dark and Luminous Matter?," Astrophys. J. **624**, L85 (2005) [arXiv:astro-ph/0502515].

[78] R. Catena and P. Ullio, "A novel determination of the local Dark Matter density," arXiv:0907.0018 [astro-ph.CO].

[79] M. Weber and W. de Boer, "Determination of the Local Dark Matter Density in our Galaxy," Astron. and Astrophys. **509**, A25 (2010) [arXiv:0910.4272 [astro-ph.CO]].

[80] P. Salucci, F. Nesti, G. Gentile and C. F. Martins, "The Dark Matter density at the Sun's location," arXiv:1003.3101 [Unknown].

[81] A. R. Duffy, J. Schaye, S. T. Kay and C. D. Vecchia, "Dark matter halo concentrations in the WMAP5 cosmology," Mon. Not. Roy. Astron. Soc. **390**, L64 (2008) [arXiv:0804.2486 [astro-ph]].

[82] G. R. Blumenthal *et al.*, "Contraction of dark matter galactic halos due to baryonic infall," Astrophys. J. **301**, 27 (1986).

[83] O. Y. Gnedin, A. V. Kravtsov, A. A. Klypin and D. Nagai, "Response of Dark Matter halos to condensation of baryons: cosmological simulations and improved adiabatic contraction model," Astrophys. J. **616**, 16 (2004) [arXiv:astro-ph/0406247].

[84] M. Gustafsson, M. Fairbairn and J. Sommer-Larsen, "Baryonic Pinching of Galactic Dark Matter Haloes," Phys. Rev. D **74**, 123522 (2006) [arXiv:astro-ph/0608634].

[85] S. H. Hansen, "Might we eventually understand the origin of the Dark Matter velocity Astrophys. J. **694**, 1250 (2009) [arXiv:0812.1048 [astro-ph]].

[86] M. I. Wilkinson and N. W. Evans, "The Present and Future Mass of the Milky Way Halo", Mon. Not. Roy. Astron. Soc. **310**, 645 (1999) [arXiv:astro-ph/9906197].

[87] G. Battaglia *et al.*, "The radial velocity dispersion profile of the galactic halo: Constraining the density profile of the dark halo of the Milky Way," Mon. Not. Roy. Astron. Soc. **364**, 433 (2005) [arXiv:astro-ph/0506102].

[88] X. X. Xue *et al.*, "The Milky Way's Circular Velocity Curve to 60 kpc and an Estimate of the Dark Matter Halo Mass from Kinematics of 2400 SDSS Blue Horizontal Branch Stars," Astrophys. J. **684**, 1143 (2008) [arXiv:0801.1232 [astro-ph]].

[89] J. Holmberg and C. Flynn, "The local surface density of disc matter mapped by Hipparcos," Mon. Not. Roy. Astron. Soc. **352**, 440 (2004) [arXiv:astro-ph/0405155].

[90] T. Naad and J. P. Ostriker, "A simple model for the evolution of disc galaxies: The Milky Way," Mon. Not. Roy. Astron. Soc. **366**, 899 (2006) [arXiv:astro-ph/0505594]

[91] K. Kuijken and G. Gilmore, "The galactic disk surface mass density and the galactic force K(z) at z=1.1kpc," Astrophys. J. **367**, L9 (1991).

[92] O. Bienayme *et al.*, "Vertical distribution of galactic disk stars: III. The galactic disk surface mass density from red clump giants," arXiv:astrp-ph/0510431.

[93] Y. Sofue *et al.*, "Unified Rotation Curve of the Galaxy - Decomposition into de Vaucouleurs Bulge, Disk, Dark Halo, and the 9-kpc Rotation Dip," arXiv:0811.0859 [astro-ph].

[94] V. F. Cardone and M. Sereno, "Modelling the Milky Way through adiabatic compression of cold dark matter halo," arXiv:astro-ph/0501567.

[95] L. S. Sparke and J. S. Gallagher, "Galaxies in the Universe - An Introduction," Cambridge University Press (2007).

[96] F. Hammer *et al.*, "The Milky Way: An Exceptionally Quiet Galaxy: Implications for the formation of spiral galaxies," Astrophys. J. **662**, 322 (2007) [arXiv:astro-ph/0702585].

[97] H. T. Freudenreich, "COBE's Galactic Bar and Disk," Astrophys. J. bf 492, 495 (1998) [arXiv:astro-ph/9707340].

[98] J. F. Navarro, C. S. Frenk and S. D. M. White, "A Universal Density Profile from Hierarchical Clustering," Astrophys. J. bf 490, 493 (1997) [arXiv:astro-ph/9611107].

[99] B. Moore *et al.*, "Dark matter substructure within galactic halos," Astrophys. J. bf 524, L19 (1999) [arXiv:astro-ph/9907411].

[100] P. Sakamoto, M. Chiba and T. C. Beers, "The Mass of the Milky Way: Limits from a Newly Assembled Set of Halo Objects," Astron. Astrophys. **397**, 899 [arXiv:astro-ph/0210508].

[101] F. J. Kerr and D. Lynden-Bell, "Review of galactic constants," Mon. Not. Roy. Astron. Soc. **221**, 1023 (1986).

[102] M. J. Reid and A. Brunthaler, "The Proper Motion of Sgr A*: II. The Mass of Sgr A*," Astrophys. J. bf 616, 872 (2004) [arXiv:astro-ph/0408107].

[103] S. Gillessen *et al.*, "Monitoring stellar orbits around the Massive Black Hole in the Galactic Centre," Astrophys. J. bf 692, 1075 (2009) [arXiv:0810.4674 [astro-ph]].

[104] M. Pato *et al.*, "Systematic uncertainties in the determination of the local dark matter density," Phys. Lett. D **82**, 023531 (2010).

[105] S. L. Shapiro and S. A. Teukolsky, "Black holes, white dwarfs, and neutron stars: The physics of compact objects," New York, USA: Wiley (1983).

[106] E. H. Gudmundsson, C. J. Pethick and R. I. Epstein, "Neutron star envelopes," Astrophys. J. **259**, L19 (1982).

[107] E. H. Gudmundsson, C. J. Pethick and R. I. Epstein, "Structure of neutron star envelopes," Astrophys. J. **272**, 286 (1983).

[108] D. Page, "The Minimal Cooling of Neutron Stars," arXiv:astro-ph/0405196.

[109] D. Page, J. M. Lattimer, M. Prakash and A. W. Steiner, "The Minimal Cooling of Neutron Stars: A New Paradigm," Astrophys. J. S. **155**, 623 (2004) [arXiv:astro-ph/0403657].

[110] W. Dehnen, D. E. McLaughlin and J. Sachania, "The velocity dispersion and mass profile of the Milky Way," Mon. Not. Roy. Astron. Soc. **369**, 1688 (2006) [arXiv:astro-ph/0603825].

[111] M. Gustafsson, M. Fairbairn and J. Sommer-Larsen, "Baryonic Pinching of Galactic Dark Matter Halos," Phys. Rev. D **74**, 123522 (2006) [arXiv:astro-ph/0608634].

[112] J. F. Navarro *et al.*, "The Diversity and Similarity of Cold Dark Matter Halos," arXiv:0810.1522 [astro-ph].

[113] A. D. Ludlow *et al.*, "Secondary Infall and the Pseudo-Phase-Space Density arXiv:1001.2310 [Unknown].

[114] E. Bertschinger, "Self - similar secondary infall and accretion in an Astrophys. J. Suppl. **58**, 39 (1985)

[115] P. Gondolo and J. Silk, "Dark matter annihilation at the galactic center," Phys. Rev. Lett. **83**, 1719 (1999) [arXiv:astro-ph/9906391].

[116] M. P. Muno, E. Pfahl, F. K. Baganoff, W. N. Brandt, A. Ghez, J. Lu and M. R. Morris, "An Overabundance of Transient X-ray Binaries within 1 pc of the Galactic Center," Astrophys. J. **622**, L113 (2005) [arXiv:astro-ph/0412492].

[117] O. Kargaltsev, G. G. Pavlov and R. W. Romani, "Ultraviolet Emission from the Millisecond Pulsar J0437-4715," Astrophys. J. **602**, 327 (2004) [arXiv:astro-ph/0310854].

[118] D. Gonzalez, A. Reisenegger and R. Fernandez, "Internal Heating of Old Neutron Stars: Contrasting Different Mechanisms," arXiv:1003.0015 [astro-ph.HE].

[119] C. T. Hill and E. H. Simmons, "Strong dynamics and electroweak symmetry breaking," Phys. Rep. **381**, 235 (2003) [arXiv:hep-ph/0203079].

[120] S. Nussinov, "Technocosmology - could a technibaryon excess provide a "natural" missing mass candidate?," Phys. Lett. B **165**, 55 (1985).

[121] R. S. Chivukula and T. P. Walker, "Technicolor cosmology," Nucl. Phys. B **329**, 445 (1990).

[122] S. B. Gudnason, C. Kouvaris and F. Sannino, "Dark matter from new technicolor theories," Phys. Rev. B **74**, 095008 (2006) [arXiv:hep-ph/0608055].

[123] Particle Data Group (C. Amsler *et al.*), "Review of Particle Physics," Phys. Lett. B **667**, 1 (2008).

[124] F. Sannino and K. Tuominen, "Orientifold theory dynamics and symmetry breaking," Phys. Rev. D **71**, 051901 (2005) [arXiv:hep-ph/0405209].

[125] D. K. Hong, S. D. H. Hsu and F. Sannino, "Composite Higgs from higher representations," Phys. Lett. B **597**, 89 (2004) [arXiv:hep-ph/0406200].

[126] D. D. Dietrich, F. Sannino and K. Tuominen, "Light composite Higgs boson from higher representations versus electroweak precision measurements," Phys. Rev. D **72**, 055001 (2005) [arXiv:hep-ph/0505059].

[127] C. Kouvaris, "Dark Majorana Particles from the Minimal Walking Technicolor," Phys. Rev. D **76**, 015011 (2007) [arXiv:hep-ph/0703266].

[128] R. Foadi, M. T. Frandsen and F. Sannino, "Technicolor dark matter," Phys. Rev. D **80**, 037702 (2009) [arXiv:0812.3406 [hep-ph]].

[129] M. T. Frandsen and F. Sannino, "Isotriplet technicolor interacting massive particle as dark matter," Phys. Rev. D **81**, 097704 (2010) [arXiv:0911.1570 [hep-ph]].

[130] T. D. Lee and C. N. Yang, "Question of Parity Conservation in Weak Interactions," Phys. Rev. **104**, 254 (1956).

[131] R. Foot, H. Lew and R. R. Volkas, "A model with fundamental improper space-time symmetries," Phys. Lett. B **272**, 67 (1991).

[132] S. I. Blinnikov and M. Yu. Khlopov, "Possible astronomical effects of mirror particles," Sov. Astron. **27**, 371 (1983).

[133] M. Yu. Khlopov *et al.*, "Observational physics of mirror world," Soviet Astr. **35**, 21 (1991).

[134] H. M. Hodges, "Mirror baryons as the dark matter," Phys. Rev. D **47**, 456 (1993).

[135] R. Foot, "Mirror Matter-Type Dark Matter," Int. Journ. of Mod. Phys. D **13**, 2161 (2004) [arXiv:astro-ph/0407623].

[136] D. J. Schlegel, D. P. Finkbeiner and M. Davis, "Maps of Dust IR Emission for Use in Estimation of Reddening and CMBR Astrophys. J. **500**, 525 (1998) [arXiv:astro-ph/9710327].

[137] C. Kouvaris and P. Tinyakov, "Can Neutron stars constrain Dark Matter?," arXiv:1004.0586 [astro-ph.GA].

[138] P. Scott, "Dark stars: structure, evolution and impacts upon the high-redshift Universe," arXiv:1101.1029 [astro-ph.CO].

[139] M. A. Perez-Garcia, J. Silk and J. R. Stone, "Dark Matter, Neutron Stars, and Strange Quark Matter," Phys. Rev. Lett. **105**, 141101 (2010) [arXiv:1007.1421 [astro-ph.CO]].

[140] P. Ciarcelluti and F. Sandin, "Have neutron stars a dark matter core?," Phys. Lett. B **695**, 19 (20011) [arXiv:1005.0857 [astro-ph.HE]].

[141] L. Iorio, "Phenomenological constraints on accretion of non-annihilating dark matter on the PSR B1257+12 pulsar from orbital dynamics of its planets," Journ. of Cosm. and Astropart. Phys. **11**, 46 (2010) [arXiv:1005.5078 [gr-qc]].

[142] J. Casanellas and I. Lopes, "Towards the use of asteroseismology to investigate the nature of dark matter," Mon. Not. Roy. Astron. Soc. **410**, 535 (2011) [arXiv:1008.0646 [astro-ph.CO]].

[143] S. D. McDermott, H.-B. Yu and K. M. Zurek, "Constraints on Scalar Asymmetric Dark Matter from Black Hole Formation in Neutron Stars," arXiv:1103.5472 [hep-ph].

[144] C. Kouvaris and P. Tinyakov, "Constraining asymmetric dark matter through observations of compact stars," Phys. Rev. D **83**, 083512 (2011) [arXiv:1012.2039 [astro-ph.HE]].

[145] C. Kouvaris and P. Tinyakov, "Excluding Light Asymmetric Bosonic Dark Matter," Phys. Rev. Lett. **107**, 091301 (2011) [arXiv:1104.0382 [astro-ph.CO]].

Part III

Swiss-Cheese Universe and Central Void Models

Chapter 9

Introduction

Over the past decades, cosmologists have developed a rather convincing model to explain the history of our Universe as a whole. Observational data have been harvested in large amounts and confronted to theoretical interpretations in order to form and adjust progressively our understanding of the cosmological works. The resulting paradigm, commonly called the *Standard Cosmological Model*, has received many strong confirmations over the years, as the precision of astrophysical measurements was continuously improved.

The Standard Cosmological Model, although being extremely satisfying on numerous aspects, presents some serious issues which tend to weaken its attractiveness. In this third and last part of our thesis, we will show how alternative models can be considered and what consequences they would have on our representation of the Universe. These models will question one of the key assumption of the Standard Cosmological Model, its homogeneity, and propose two differents approaches: a world made of matter and holes (the Swiss-Cheese Universe), and a world in which the observer lives near the centre of a large underdensity (central void models).

After a brief description of the Standard Cosmological Model and these alternative concepts in the current Chapter, we will present some analytical considerations (Chapter 10). The results will then be discussed separately in Chapter 11, before a few words of conclusion (Chapter 12).

9.1 Dark Energy in the Standard Cosmological Model

In the previous part of our thesis, we presented the fundamental elements constituing the so-called Standard Cosmological Model (see Subsection 5.1.1), leaving apart one of them, Dark Energy, to be treated in a more appropriate time. Since we are going to talk about cosmological scales and the evolution of the Universe as a whole, the time has come to explain what physicists mean by Dark Energy, what evidences we have of its existence (Subsection 9.1.1) and what are its limitations (Subsection 9.1.2).

Dark Energy (DE) is thought to permeate the whole Universe and to cause its expansion rate to accelerate. In the Standard Cosmological Model, it is calculated that DE accounts for about 73% of the total mass-energy in the

Universe. The simplest and most common candidate for DE is the cosmological constant Λ which is characterised by a constant energy density in space and time. Its equation of state, which gives the relationship between the pressure P and the energy density ρ, is

$$w = P/\rho = -1.$$

As cosmological constant, DE is simply included in Einstein's field equations of General Relativity and in the Friedmann equations as presented in Subsection 5.1.1. From Eq. (5.4), it is clear that Dark Energy acts, at the background level, as a repulsive force against gravity. Its negative pressure generates the accelerated expansion on large scales, making it an essential part of the Standard Cosmological Model's success in explaining the observations.

9.1.1 Evidences for the Existence of Dark Energy

The Standard Cosmological Model, including Dark Energy as a cosmological constant Λ, has proven very efficient at explaining the complex network of observational data. Over the years, an always stronger beam of evidences formed around its fundamental principles, so much so that it has become increasingly delicate for scientists to depart from its convincing paradigm. In the next paragraphs, we will briefly talk about some of the most striking evidences: constraints given by Type Ia supernovae (see Section 9.2), the deduced age of the Universe, interpretations from the Cosmic Microwave Background radiation and from large scale structure formation.

Deduced Age of the Universe

The age of our Universe can be determined by using the Hubble parameter, which is given by

$$H(z) = H_0 \left[\Omega_{m,0}(1+z)^3 + \Omega_{\Lambda,0}(1+z)^{3(1+w_\Lambda)} + \Omega_{r,0}(1+z)^4\right]^{1/2}, \qquad (9.1)$$

for a flat FLRW Universe, without making any assumption regarding the nature of the DE and its equation of state. From the relation $dt = -dz/\left[H(z)(1+z)\right]$, we can calculate the age of the Universe as

$$t_0 = \int_0^\infty \frac{dz}{H(z)(1+z)}.$$

If we neglect the contribution of the radiation and consider a cosmological constant for the DE, then it becomes

$$t_0 = \frac{1}{H_0}\int_0^\infty \frac{dz}{(1+z)\left[\Omega_{m,0}(1+z)^3 + \Omega_\Lambda\right]^{1/2}}. \qquad (9.2)$$

When integrating Eq. (9.2) and taking the limit $\Omega_\Lambda \to 0$ for a flat Universe with $\Omega_{m,0} + \Omega_\Lambda = 1$, we obtain

$$t_0 = \frac{2}{3H_0}.$$

Using a standard value of $H_0 = 72$ km/s/Mpc, this leads to an age, for a Universe without DE, of about 9 Gyr. This result is however inconsistent with

the estimated age of globular clusters, thought to be a least a few Gyr older [1, 2, 3]. Thus, it seems that a matter dominated Universe could not be old enough to contain its oldest objects. Dark Energy must indeed be included in order to increase its age and make it reach at least the lower bound fixed by globular clusters.

Cosmic Microwave Background

Over the past 15 years, the Cosmic Microwave Background (CMB) radiation has been thoroughly studied in order to deduced information about the early evolution of our Universe. Increasingly precise measurements of its temperature fluctuations have led to one of the most significant result of modern cosmology: the CMB anisotropy power spectrum (cf. corresponding paragraph in Subsection 5.1.2). This power spectrum represents an imprint of the physics happening before recombination, and its features reveal the evolution of pressure waves in the primordial photon-baryon plasma. With a good understanding of the physical processes acting on the CMB anisotropies, the specific features of its power spectrum, which are sensitive to the value of the cosmological parameters, can be used to test cosmological models [4, 5, 6, 7].

So far, the most accurate measurements of the CMB anisotropies were made by WMAP [8], which collected data over a period of seven years and played a key role in confirming the pertinence of the current Standard Cosmological Model. WMAP data clearly indicate that the shape of our Universe is very close to being flat, which means that its total mass-energy density is very close to its theoretical critical density. As measurements of the CMB show that the total amound of matter, including any kind of Dark Matter, cannot account for more that about 30%, Dark Energy is thought to represent about 70% of it.

When taking into account all the known constraints on cosmological parameters, the Dark Energy density is estimated at

$$\Omega_\Lambda = 0.728^{+0.015}_{-0.016}.$$

Baryon Acoustic Oscillations

The acoustic peaks observed in the Cosmic Microwave Background power spectrum are predicted to be detectable in the galaxy power spectrum as well, under the form of a series of weak fluctuations as a function of scale [9, 10, 11, 12], features usually known as *wiggles*.

Since the position of the peaks can be considered as standard rulers [13], an analysis of the galaxy power spectrum can be used to measure cosmological parameters. Baryon Acoustic Oscillations (BAO) have indeed been detected at low reshift in the 2dF and SDSS galaxy surveys [14, 15].

Standard rulers can be defined when there is a possible comparison between the known, true size of an object, and its observed dimensions in the sky. In the case of the BAO signal, one uses the measured subtended angle, $\Delta\theta$ (i.e. how wide in angle the object looks), and the length of the ruler, $\Delta\chi$, in order to find the angular diameter distance

$$d_A(z) = \frac{\Delta\chi}{\Delta\theta},$$

where $d_A(z) \propto \int_0^z \frac{dz'}{H(z')}$. And the measured redshift interval, Δz (i.e. how deep

in space the object is), provides an estimate of the Hubble parameter through

$$H(z) = c\frac{\Delta z}{\Delta \chi}.$$

Refering to Friedmann equation (Eq. 9.1), the BAO data can therefore put constraints on the cosmological parameters.

Large Scale Structure

The formation of large structures in the Universe is conventionally considered to emerge from small perturbations in the matter-energy distribution, caused by gravitational instabilities. The mechanism required to generate these initial instabilities in the very early phase of the Universe is thought to be quantum fluctuations. The best tool to describe the perturbations and their evolution is the density contrast

$$\delta(t, \vec{x}) = \frac{\rho(t, \vec{x}) - \bar{\rho}(t)}{\bar{\rho}(t)},$$

where $\rho(t, \vec{x})$ is the energy density and $\bar{\rho}(t)$ represents its background value.

The initial density perturbations in the early Universe can be represented as a Gaussian random variable and a given intial power spectrum given by

$$P(k)(2\pi)^3 \delta_D \left(\vec{k} - \vec{k'}\right) = \left\langle \delta(\vec{k}) \delta^\star(\vec{k'}) \right\rangle,$$

where $\delta(\vec{k})$ is the Fourier transform of $\delta(t, \vec{x})$ and $\langle ... \rangle$ stands for an average over all the elements in the statistical ensemble. This power spectrum is the best insight we might have in structure formation.

At matter-radiation equality, the pressure support created by photons becomes smaller that the gravitational attraction due to the matter component: objects start to form in the Universe. Hence matter-radiation equality fixes the position of the peak in the matter power spectrum. In particular, its position is shifted towards larger scales (smaller k) in the presence of Dark Energy (Fig. 9.1). Large scale structures can therefore be used to probe the existence of Dark Energy.

The necessity for Dark Energy is made clear when studying the matter power spectrum based on the distribution of the galaxies in the Universe. Large galaxy surveys like the Two-degree-Field Galaxy Redshift Survey (2dF) [16] and the Sloan Digital Sky Survey (SDSS) [17] brought observational data and helped to reaffirm that ΛCDM is indeed the most favored cosmological model. Fig. 9.2 shows the galaxy power spectra for the Luminous Red Galaxy (LRG) and for the main galaxy samples of SDSS [18]. The position of the peaks around $0.01h\text{Mpc} < k < 0.02h\text{Mpc}$ confirms that ΛCDM is favored over CDM, as shown in Fig. 9.1. Observations of large scale structures are definitely consistent with the existence of Dark Energy.

If the FLRW metric trully describes our Universe, then the evidences for the existence of Dark Energy are compelling. However, the assumptions made when assuming an FLRW Universe might not be true, and ΛCDM could prove to be an unaccurate, though phenomenologically successful description of the cosmos. In this case, we would have to look for alternative explanations for the apparent acceleration of the expansion rate. Inhomogeneous metrics, like the

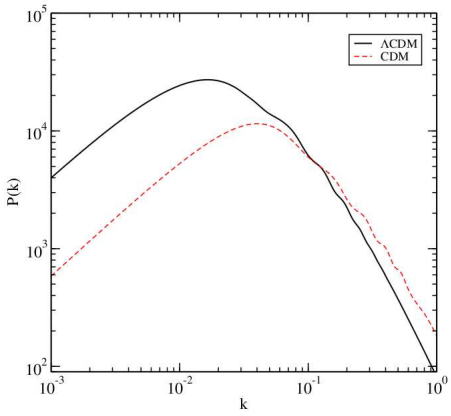

Figure 9.1: Matter power spectrum for two different CDM models: ΛCDM includes Dark Energy ($\Omega_{m,0} = 0.289$) whereas CDM represents a Universe without DE ($\Omega_{m,0} = 1$). From [6], evaluated with CAMB code.

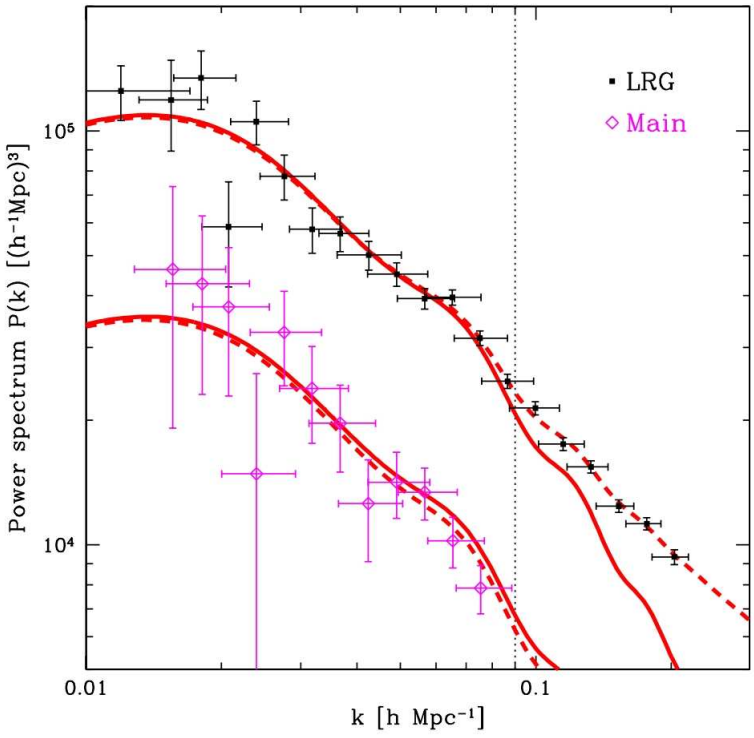

Figure 9.2: Power spectra with errorbars for the Luminous Red Galaxy (LRG) sample and the main galaxy sample from the SDSS survey [18]. Solid lines show the theoretical prediction for ΛCDM in the linear perturbation theory, whereas dashed lines include the non-linear corrections to the matter power spectrum.

Swiss-Cheese Universe and central void models, count among these alternatives. We will present them briefly in Section 9.3, before studying them in depth throughout this last part of our thesis.

9.1.2 Conceptual Issues with Dark Energy

Although including Dark Energy in our current view of the Universe might seem like a perfect answer to many cosmological puzzles, there is a certain number of conceptual issues rising with doing so. These problems cast a shadow the Standard Cosmological Model and incite scientists to try and look for alternative models where Dark Energy would not have such an essential role, if any at all. We will briefly mention here two of these issues: the fine tuning problem and the coincidence problem.

Fine Tuning Problem

This first conceptual issue comes from the fact that Dark Energy, as cosmological constant Λ, can be associated with the vacuum energy of an empty space: the discrepancy between the observed value of Λ and the theoretical value of the vacuum energy is absurdly large - 120 orders of magnitude!

From the expression of the Hubble parameter

$$H^2 = \frac{8\pi G}{3}\rho - \frac{K}{a^2} + \frac{\Lambda}{3},$$

one deduces that, in order to have a phase of accelerated expansion today, we need the cosmological constant Λ to be of the order of

$$\Lambda \approx H_0^2 = (2.12h \times 10^{-42}\text{GeV})^2,$$

which corresponds to an energy density of

$$\rho_\Lambda = \frac{\Lambda m_{\text{Pl}}^2}{8\pi} \approx 10^{-47}\text{GeV}^4,$$

where $m_{\text{Pl}} = G^{-1} = 1.22 \times 10^{19}\text{GeV}$ is the Planck mass.

On the other hand, the vacuum energy is evaluated by the sum of the zero point energies of a quantum field of mass m:

$$\rho_{vac} = \int_0^\infty \frac{\mathrm{d}^3k^3}{(2\pi)}\frac{1}{2}\sqrt{k^2+m^2},$$

where k is the momentum. If we choose the cut-off scale k_{max} to be the Planck scale, then the vacuum energy density is:

$$\rho_{vac} \approx \frac{k_{\text{Pl}}^4}{16\pi^2} \simeq 10^{47}\text{GeV}^4$$

.

The ratio between these two results, which are supposed to be similar, is:

$$\frac{\rho_{vac}}{\rho_\Lambda} = \frac{10^{74}\text{GeV}^4}{10^{-47}\text{GeV}^4} = 10^{121}. \tag{9.3}$$

The theoretical value of the Dark Energy density is 121 orders of magnitude larger than its observed value. None of the numerous attempts to solve the fine tuning problem (QCD, supersymmetry, string theory, etc. [19, 20, 21, 22, 23]) has proven convincing so far.

Coincidence Problem

This second conceptual issue is not a characteristic of the cosmological constant Λ as it is relevant for all Dark Energy models. According to the observations, it seems that the value of the Dark Energy density today, $\Omega_{\Lambda,0}$, is comparable to the matter energy density $\Omega_{m,0}$. There is no obvious reason for this to happen, as these to values follow very different evolution path during the history of the Universe. Having them so close to each other at the present time might appear as a suspicious coincidence, and cosmologists usually dislike putting the observer in a particular position.

The energy density for a general fluid is given by

$$\rho(t) = \rho_0(1+z)^{3(1+w)},$$

where ρ_0 is the current energy density and w the equation of state parameter. Comparing the matter energy density ($w_m = 0$) and the DE density ($w_\Lambda = -1$), one can deduce the time at which they become comparable:

$$z_c = \left(\frac{\Omega_\Lambda}{\Omega_m}\right)^{1/3} - 1,$$

which corresponds to a value of $z_c \approx 0.3$ if we consider $\Omega_\Lambda \approx 0.7$ and $\Omega_m \approx 0.3$.

It is not completely impossible that we are indeed living in the special time where these two cosmological parameters coincide. Because of its subjectiveness, however, many attempts have been tried (e.g. [24, 25, 26, 27]) in order to solve this coincidence problem. One of the alternative models, known as *quintessence*, was developed from the idea that the equation of state of Dark Energy might be varying in space and time [28]. We will come back to the latter in Section 11.2.

9.2 Type Ia Supernovae as Standard Candles

Supernovae count among the most spectacular cataclysmic events which can be observed in the Universe. They represent the ultimate phase of stellar evolution for massive stars and can be of completely different types. The observational distinction between them is based on the contrasting aspect of their electromagnetic spectra [29], which result from different formation mechanisms. Thus, Type I supernovae do not exhibit any hydrogen lines whereas Type II supernovae do. The former are further subdivided into Type Ia (with a strong Si II line at 615 nm) and Type Ib/c (no Si II line, but presence/absence of helium lines) supernovae.

Supernovae are extremely luminous and generate a burst of intense radiation which can become brighter than their entire galaxy. When occuring in our Milky Way, their apparent magnitude might even reach a level of brightness comparable to the moon. Besides their spectral signature, supernovae are characterised by typical light curves which present recognisable features. All of them share the same general profile: rapid increase in intensity reaching a peak of brightness, before a progressive decline. Distinction between the different types comes from the relative value of the peak brightness and the rate of decline. Type Ia supernovae possess the highest maximum brightness and a rate of dimming about 50% faster than other Type I supernovae.

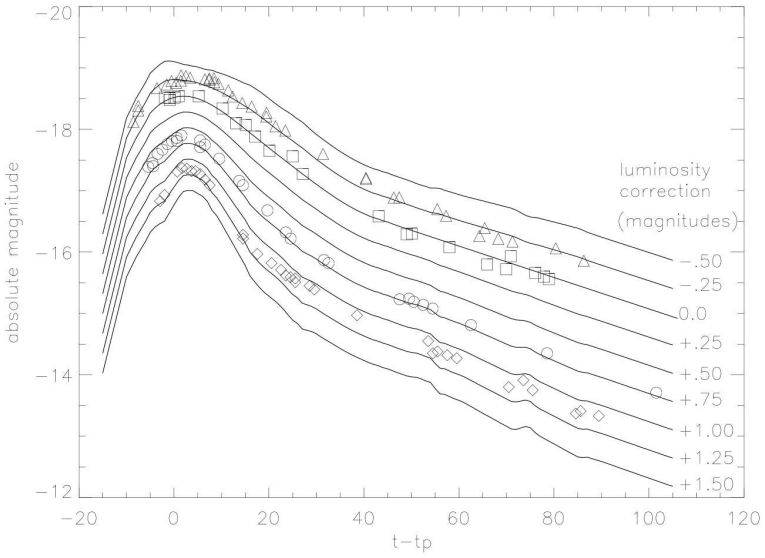

Figure 9.3: Comparison of light curves for different Type Ia supernovae showing the inverse correlation between the maximum brightness and the decline rate [30].

It is understood that Type Ia supernovae (SNe Ia, singular SN Ia) are fundamentally different from other supernovae events. The remarkable consistency of their light curves and spectra lead scientists to think that they must be the result of a fairly uniform mechanism. Although the details of this mechanism are yet to be clearly established, the generally accepted view is that SNe Ia are caused by the catastrophic explosion of a white dwarf star[1] in a binary system. Such a dramatic event would be triggered by accretion of matter from the white dwarf's companion, driving its mass close to the Chandrasekhar limit. The increasing weight causes the pressure and density to rise, until the conditions become favorable for carbon fusion. Since degeneray pressure is independant of temperature, the white dwarf cannot regulate the fusion process, and the resulting runaway reaction provokes a violent explosion which disruptes the star and causes an extreme increase in luminosity.

Most SNe Ia reach a consistent maximum brightness in the visual wavelenght bands of

$$M_V \simeq -19.3 \pm 0.03,$$

with a typical spread of less than about 0.3 magnitude. A clear relationship has been observed between the peak luminosity and the rate of decline, which allows astronomers to precisely determine the individual maximum brightness of any SN Ia (Fig. 9.3). This similarity in absolute magnitude implies that SNe Ia can be used as standard candles in order to measure the distance of the galaxies in which they reside, based on the relation between their absolute magnitude M_V

[1] White dwarves are small but very dense stars mainly made of electron-degenerate matter. They are the last stage of a low-to-medium mass main sequence stars, in which the core temperature is not high enough to allow carbon fusion. They are thought to be the final evolutionary state of most stars in our galaxy, including the Sun.

and apparent magnitude m_V:

$$m_V - M_V = 5\log_{10}(\frac{D_L}{\text{Mpc}}) + 25,$$

where D_L is the distance of the star in Mpc. Once the relative magnitude m_V is measured, the redshift of the source can be obtained by comparing the frequency of the photons. It is then possible to generate a Hubble diagram by plotting the distance modulus $\mu = m_V - M_V$ against the redshift z. In order to extract information from these observational data, the theoretical luminosity distance must be calculated according to the chosen cosmological model. In the case of an FLRW background, the luminosity distance reads

$$D_L = c(1+z)\int_0^z \frac{dz'}{H(z)},$$

with $H^2(z) = H_0^2 \sum_i \Omega_{i,0}(1+z)^{3(1+w)}$. This translates into

$$D_L = c\frac{1+z}{H_0}\int_0^z \frac{dz'}{\sqrt{\Omega_{m,0}(1+z)^3 + \Omega_{\Lambda,0} + \Omega_{r,0}(1+z)^4 + \Omega_{k,0}(1+z)^2}}. \quad (9.4)$$

At the end of the 1990s, precise measurements of distant SNe Ia, combined with previous observations of closer supernovae, have lead to the conclusion that the expansion of the Universe was accelerating (e.g. [31]). This discovery was deduced from the attempt to fit the SN Ia data in order to yield values for the cosmological parameters. Based on the fit of the effective magnitude versus redshift relation, it has been concluded that the data were strongly inconsistent with a flat or an open $\Lambda = 0$ cosmology (Fig. 9.4). Refinements in terms of observations and cosmological consistency have been regularly performed during the past decade (e.g. [33]), always confirming the excellent fits to the observational constraints that non-zero Λ cosmologies can provide.

9.3 Inhomogeneous Alternatives

One of the fundamental assumptions made in the Standard Cosmological Model concerns the homogeneity of the energy distribution throughout the Universe. This strong assumption allows theoreticians to describe its evolution at large scales in an elegant way, but it does not hold at smaller scales where irregular clumps of matter are clearly observed. Besides the observational evidence of galaxy clustering, N-body simulations and theoretical considerations also predict that our Universe is mainly made of large underdense regions surrounded by fine walls and filaments of matter [34, 35, 36, 37].

Two different paradigms have been deduced from this fact, depending on the assumed location of the observer and the scale of the underdensities considered: the Swiss-Cheese Universe [38, 39], made of cheesy matter surrounding empty holes, and the central void models, in which the observer lives near the centre of a rather large underdensity. These two approaches, conceptually close and thus treated here in parallel, will be briefly introduced in the end of this Section. We will then bring some common analytical considerations, before presenting the investigation methods and results for each paradigm in Sections 11.2 and 11.3 respectively.

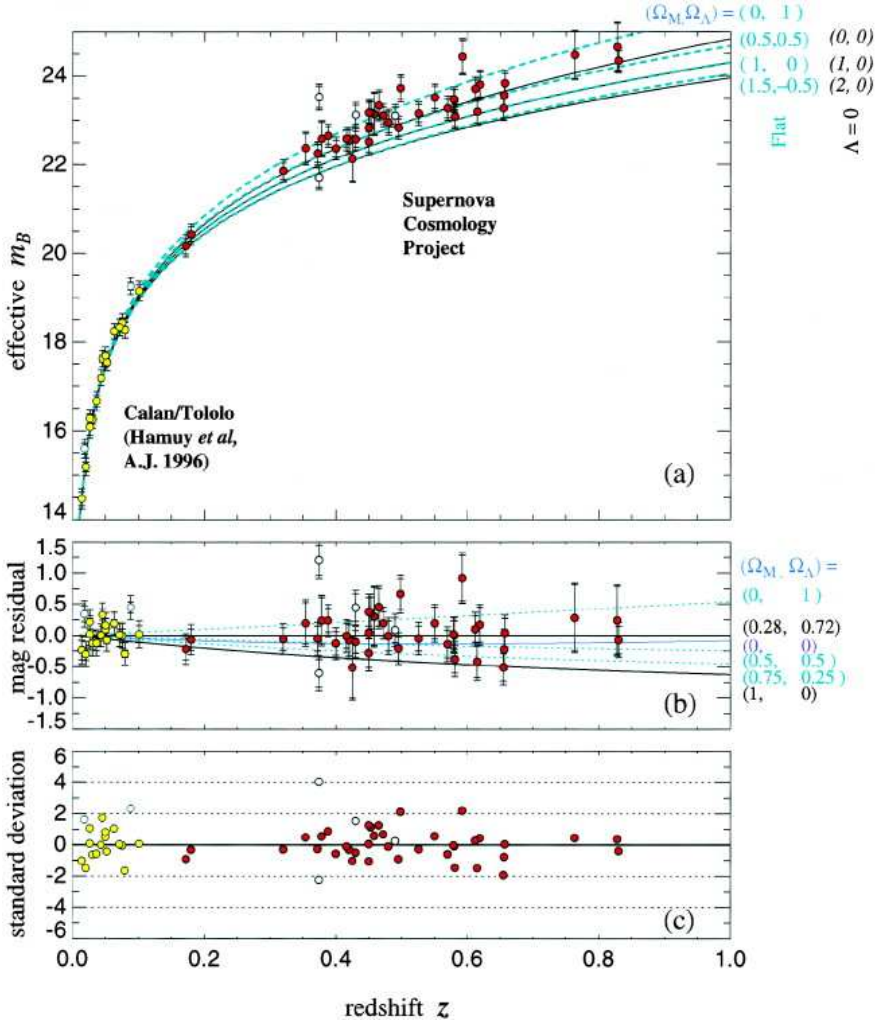

Figure 9.4: (a) Hubble diagram for the two series of SNe Ia considered in [31]: 42 high-redshift SNe Ia from the Supernova Cosmology Project and 18 low-redshift SNe Ia from the Calán/Tololo Supernova Survey [32]; (b) Magnitude residuals from the best-fit flat cosmology, $(\Omega_M, \Omega_\Lambda) = (0.28, 0.72)$; (c) Uncertainty-normalised residuals from the same best-fit cosmology.

9.3.1 Swiss-Cheese Universe

The Swiss-Cheese[2] cosmology has been studied in details during the past decade [40, 41, 42, 43, 44] as an inhomogeneous alternative to the ΛCDM model. It is built as a combination of two interconnected metrics: a standard FLRW metric describing the *cheese*, i.e. the walls and parts of the Universe characterised by a homogeneous matter distribution, and a Lemaître-Tolman-Bondi metric (see Section 10.1) describing the *holes*, i.e. the underdense regions around which matter is concentrated. The geometry of these holes is such that they match exactly the FLRW metric at their border. Moreover, mass compensation in their density profile assures that the global effect of a zone containing such a hole is as if it were FLRW, following Birkhoff's theorem[3] [45]. Being an exact solution to Einstein's equations, the Swiss-Cheese model approximates today's inhomogeneous Universe in an exactly solvable manner.

The main interest in the Swiss-Cheese Universe comes from the fact that its underdensities have a lensing effect which causes the light emitted by distance objects to appear dimmer than in a homogeneous Universe. Two important points have been found concerning this effect [46]: if the holes are perfectly aligned, the underdense holes can mimic a Dark Energy of about $\Omega_\Lambda = 0.4$, but a random distribution of spherical voids produces a vanishing average effect.

In the next Chapter, we will present in detail the technical aspects of such models and explain how we propose to study their evolution based on a chosen parametrisation and a set of initial conditions.

9.3.2 Central Void Models

One of the most studied inhomogeneous alternative to Dark Energy is the so-called "local void" or "central void" paradigm [47, 48, 49]. The basic idea is that we live near the middle of a large underdense region of the Universe and that this underdensity has the ability to mimic the effects of Dark Energy on cosmological observations.

The local void scenario has been studied under various forms and methods:

- Void modelled as an open FLRW region connected through a singular mass shell to a FLRW background [50], which showed that a void with a radius of 200 Mpc can fit the supernovae data without the need for DE;
- A central LTB (see Section 10.1) region [51], similar to an Einstein-de Sitter cosmology with a Hubble parameter of $H_0 = 51$ km/s/Mpc and a radius of 1.3 Gpc, which can match both the SN Ia observations and the location of the first acoustic peak in the CMB;
- An LTB-based 'minimal void' model [52], which predicts that the smallest possible void fitting the supernovae constraint has a radius of 350 Mpc, but is inconsistent with the measurements of the Baryon Acoustic Oscillations peak [53];

[2] We ought to warn the reader about this somewhat fallacious name: not all Swiss cheeses have holes. This common misconception probably comes from the popularity of the *Emmentaler*, which indeed contains holes and is widely exported (and copied) all around the world.

[3] Birkhoff's theorem states that any spherically symmetric solution of the vacuum field equations must be stationary and asymptotically flat.

- LTB models using much larger voids ($r \approx 2.5$ Gpc) [54], which have been demonstrated to match all the current constraints, i.e. SN Ia observations, BAO data and CMB peak.

Research for the best fit of the supernovae given by a void model has consistently evolved with the release of new sets of data. A void with radius 1.3 Gpc and underdensity of about 70% at its centre has been shown, in [55], to convincingly fit the first Union dataset from the Supernova Cosmology Project[4] [56]. Based on the more extended dataset of the Union2 compilation [33] and other updated constraints, the radius of the optimal void has been found to lie at around 3.5 Gpc, for a matter underdensity of about $\Omega_m \approx 0.13$ [57].

The main conceptual issue regarding the central void paradigm comes from the fact that the observer, in most cases, must be situated very near the centre of the underdensity in order to insure consistent predictions [51, 58]. This strong constraint seems to contradict the Copernican principle as the observer would indeed have to be a specially favored position.

[4] http://supernova.lbl.gov

Chapter 10

Theory and Numerical Models

We construct our Swiss-Cheese Universe by combining two components: the 'cheese', made of spatially flat FRW solution and the 'holes', made of LTB solution. For simplicity, we assume that the effects of *complete* holes situated between the source and the observer cancel out along the light path. Our interest is focused on the hole nearest to the source only. So we will not discuss the influence of holes spatial distribution in this study.

10.1 The Model: Lemaître-Tolman-Bondi Universe

Our model is based on the Lemaître-Tolman-Bondi (LTB) metric [59, 60, 61], a spherically symmetric solution of Einstein's equations, which can be written as (in units $c = 1$)

$$ds^2 = -dt^2 + S^2(r,t)dr^2 + R^2(r,t)(d\theta^2 + sin^2\theta d\phi^2) \tag{10.1}$$

where we use comoving coordinates (r, θ, ϕ) and proper time t. Considering pressureless dust, Einstein's equations imply the following constraints:

$$S^2(r,t) = \frac{R'^2(r,t)}{1+2E(r)}, \tag{10.2}$$

$$\frac{1}{2}\dot{R}^2 - \frac{GM(r)}{R(r,t)} - \frac{1}{3}\Lambda R^2 = E(r), \tag{10.3}$$

$$4\pi\rho(r,t) = \frac{M'(r)}{R'(r,t)R^2(r,t)}, \tag{10.4}$$

where a dot stands for partial derivative with respect to t and a prime with respect to r; $\rho(r,t)$ is the energy density of the matter, and $G \equiv 1/m_{Pl}^2$ is the Newton constant. To specify the model we intend to use, we have to define the two arbitary functions $E(r)$, corresponding to the spatial curvature, and $M(r)$, which is simply the mass integrated within a comoving radial coordinate r:

$$M(r) = 4\pi \int_0^r \rho(r,t)R^2R'dr.$$

In order to do so, we must choose an initial density profile $\rho(r, t_{\rm LTB})$, where $t_{\rm LTB} = t_{\rm LTB}(r)$ refers to the beginning of the LTB evolution and is set to a constant for simplicity. We then have to choose $E(r)$ in order to match the flat FRW model at the boundary of the hole. The main point of this process is to assure that the average density inside the hole equals the one outside, so that an observer situated in the cheese would not be aware, *locally*, of the presence of the hole.

We intend to test our model by sending photons through the voids and measuring redshifts. To do so, we must integrate the equation for their radial trajectory

$$\frac{dt(r)}{dr} = \frac{R'\left(r, t(r)\right)}{\left(1 + 2E(r)\right)^{1/2}}. \tag{10.5}$$

Compared to other models based on the Swiss-Cheese Universe, the present study presents some decisive characteristics: we assume that the observer, although occupying no particular position in space with respect to the holes, is always situated in the cheese; we consider only the effects caused by the 'last hole', assuming that, on average, the effects due to all the other holes placed on the light path cancel out.

10.2 Parameters and Initial Conditions

In order to characterise the LTB model we intend to use, we have to define the initial density profile $\rho(r, t_{\rm LTB})$. We then will build the two arbitrary functions $E(r)$ and $M(r)$ based on this profile. The expression we choose for it is based on Valentin Kostov's work [62] on average luminosity distances in inhomogeneous Universes where the density profile is designed as follows:

$$\rho(r, t_0) \quad = \quad \bar{\rho}(t_0) \;\times\; \left\{A_1 + A_2 tanh\left[\alpha\left(r - r_1\right)\right] - A_3 tanh\left[\beta\left(r - r_2\right)\right]\right\},$$

for $r < r_h$, where r_h is the radius of the void; and $\rho(r, t_0) = \bar{\rho}(t_0)$ for $r \geq r_h$. Given (r_1, r_2), the values of the coefficients (A_1, A_2, A_3) and (α, β) are chosen so that $\rho(r_h, t_0) = \bar{\rho}(t_0)$ and the integrated mass inside the hole $M(r_h) = 4\pi \int_0^{r_h} \rho(r, t_0) r^2 dr = \frac{4}{3}\pi\bar{\rho}(t_0) r_h^3$.

The function $E(r)$ plays the role of the spatial curvature in the LTB solution. It is defined using Eq. (10.3) and considering the initial time of the LTB evolution $t_{\rm LTB}$. At this early time, $R(r, t_{\rm LTB}) = a(t_{\rm LTB}) r = a_{\rm LTB} r$ and we have, in real units:

$$E(r) = \frac{1}{2}\frac{H_{\rm LTB}^2 a_{\rm LTB}^2}{c^2}\left(r^2 - \frac{3}{4\pi}\frac{M(r)}{a_{\rm LTB}^3 r \bar{\rho}(t_{\rm LTB})}\right), \tag{10.6}$$

where $\bar{\rho}(t)$ is the average energy density at time t.

In order to guarantee that the chosen parametrisation of the voids is consistent with observational constraints, we compare the density profiles with observed values of over- and underdensities at different times of the LTB evolution: at initial time $t = t_{\rm LTB}$ and at final time $t = t_{\rm now}$. We set $t_{\rm LTB}$ to be the time of last scattering, $t_{\rm LTB} = t(z = 1100)$. So the constraint at initial time comes from the scale of temperature fluctuation in the Cosmic Microwave Background (CMB) $\Delta T/T \approx 10^{-5}$, which corresponds to a variation in density of the order of 10^{-4}.

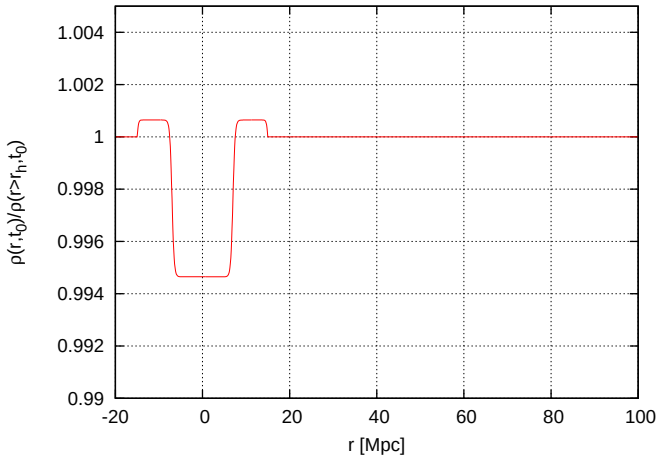

Figure 10.1: Initial density profile define at $t = t_{\mathsf{LTB}}$ and showing the shape of the cosmological voids and of its surrounding walls of denser matter.

Density Profile Parameters	
r_1	7 Mpc
r_2	15 Mpc
A_1	9.97×10^{-1}
A_2	2.99×10^{-3}
A_3	1.70×10^{-4}
α	0.6
β	3.0

Table 10.1: Chosen parametrisation of the voids, taking into account the constraints at initial time t_{LTB} and final time t_{now}.

At the other extremety, when $t = t_{\mathrm{now}}$, the guideline for density profiles is given by observations of the present underdensities in the matter distribution of our Universe. Recent studies (e.g. [37]) show that the voids that we see nowadays probably correspond to regions where the density is $\sim 20\%$ of the mean cosmic density.

Assuring that these constraints are taken into account implies that we carefully choose the spatial geometry of the voids. The chosen parameters are given in Table 10.2.

10.3 Numerical Modelling of Central Voids

The central void models that we are developing here are based on the theoretical considerations presented in Chapter 10. Instead of placing the spherical voids far away from the observer and close to the luminous source, we will simply create a large underdensity around the observer itself. One major difference comes from the fact that the observer will not necessarily be situated at the centre of the coordinate system. This fact has to be taken into account when

describing the photon path through the geodesic equation

$$\frac{d^2x^\mu}{d\lambda^2} + \Gamma^\mu_{\alpha\nu}\frac{dx^\alpha}{d\lambda}\frac{dx^\nu}{d\lambda} = 0, \tag{10.7}$$

where $\Gamma^\mu_{\alpha\nu}$ is the Christoffel symbol, and λ is the monotonically increasing parameter defined along the photon path. We follow the reasoning presented in [67] in order to derive a set of first-order differential equations. Starting from the LTB metric

$$ds^2 = -dt^2 + S^2(r,t)dr^2 + R^2(r,t)(d\theta^2 + sin^2\theta d\phi^2),$$

where the function $R(r,t)$ and $S(r,t)$ are defined as in Eq. (10.2) and (10.3), and assuming an axial symmetry with makes the photon paths independent of the azimuth angle ϕ, we obtain the following series of equations (in $c = 1$ units):

$$\frac{dt}{d\lambda} = \left[\frac{R'^2}{1+2E}\left(\frac{dr}{d\lambda}\right)^2 + \frac{J^2}{R^2}\right]^{1/2}, \tag{10.8}$$

$$\frac{dr}{d\lambda} = p, \tag{10.9}$$

$$\frac{d\theta}{d\lambda} = \frac{J}{R^2}, \tag{10.10}$$

$$\frac{dp}{d\lambda} = -\left(\frac{R''}{R'} - \frac{E'}{1+2E}\right) - 2\frac{\dot{R}'}{R'}\frac{dt}{d\lambda}\frac{dr}{d\lambda} + \frac{R(1+2E)}{R'}\left(\frac{d\theta}{d\lambda}\right)^2, \tag{10.11}$$

$$\frac{dz}{d\lambda} = -\frac{(1+z)}{dt/d\lambda}\left[\frac{R'\dot{R}'}{1+2E}\left(\frac{dp}{d\lambda}\right)^2 + \frac{\dot{R}}{R^3}J^2\right]. \tag{10.12}$$

In these equations, $p = dr/d\lambda$, a dot stands for a partial derivative with respect to time, and a prime for a partial derivative with respect to the comoving coordinate r. J is a constant expressed as

$$J = J_0 = R\sin(\xi), \tag{10.13}$$

where ξ is given by $\cos(\xi) = -\frac{R'}{\sqrt{1+2E}}\frac{p}{u}$.

Initial conditions are simply given by

$$t_0 = t_{\rm now}, \tag{10.14}$$

$$r_0 = r_{\rm observer}, \tag{10.15}$$

$$\theta_0 = 0, \tag{10.16}$$

$$p_0 = \frac{\sqrt{1+2E}}{R'}\cos(\xi), \tag{10.17}$$

$$z_0 = 0. \tag{10.18}$$

The parametrisation of the void profile resembles closely the one we developed for Swiss-Cheese Universes (Chapter 10), the main difference being that the observer is now situated close to the centre of the LTB metric. Table 10.3 gives indicative ranges of values for the various parameters.

Since our aim is to mimick the effect of Dark Energy without having to require a cosmological constant, we naturally set $\Omega_\Lambda = 0$ and take Ω_m to vary freely between its boundaries. Therefore, the global geometry of the Universe is not necessarily flat.

Density Profile Parameters	
r_1	10-500 Mpc
r_2	11-5000 Mpc
A_1	0.99-1.00
r_0	1-200 Mpc
Ω_m	0.1-1.0
Ω_Λ	0.0
α	0.005
β	0.005

Table 10.2: Indicative ranges of values of the parametrisation of central void models, taking into account cosmological and numerical constraints described in the following Sections.

10.3.1 Luminosity Distance for Individual Photon Paths

Similarly to what we did for Swiss Cheese models (see Subsection 11.1.1), we obtain distance and redshift information by sending two photons through the metric with slightly different initial conditions and we compare their final states. Using the set of differential equations described before, along with the initial conditions and the constraints of the system, one has the possibility to follow the evolution of the physical parameters along the photon path, integrating backwards from the observer to the source.

Following the calculation presented in [68], we obtain the angular diameter distance from the expression:

$$d_A = \left(\frac{R\sin\theta}{\sin\gamma}\right)^{1/2} \left[\frac{R'^2}{1+2E}\left(\frac{\partial r}{\partial \xi}\right)^2 + R^2\left(\frac{\partial \theta}{\partial \xi}\right)^2\right]^{1/4}, \tag{10.19}$$

where $\partial r/\partial\xi$ and $\partial\theta/\partial\xi$ are the differences in comoving distance and azimuthal angle, respectively, between the two photons, resulting from the slight initial difference in ξ, as measured at the position of the source. The luminosity distance is then simply calculated as $d_L = d_A(1+z)^2$, and the distance modulus as $\mu = 5 \cdot \log_{10}(\frac{d_L}{10\text{ pc}})$.

In this process, we are considering each SN Ia individually in order to determine the influence of the void. This means that we have to take into account their actual position in the sky, since the observer does not necessarily sits in the middle of the LTB metric. In practice, we choose the re-align the coordinate system of the supernovae with a coordinate system in which the observer is situated on the z axis, so that the initial conditions $r_0 = r_{\text{observer}}$ and $\theta_0 = 0$ are respected.

Finally, the simulated value of the distance modulus μ is compared to its observed value, and the quality of the model is evaluated through its χ^2 value:

$$\chi^2 = \sum_{\text{SNe}} \frac{(\mu_{\text{simulated}} - \mu_{\text{measured}})^2}{\sigma^2_{\text{measured}}}.$$

10.3.2 Dealing with Shell-Crossing

One of the issues that might arise when working with dynamic underdensities is a phenomenon called *shell-crossing*. Its nature and implications have been studied in details ([69, 70, 71, 72] and references in [73]), but we will limit ourselves to describing this phenomenon and how we plan to avoid it in our present research.

Shell-crossing is usually taken into account when studying Swiss-cheese models where several voids evolve simultaneously and may interact with each other. The inner part of these voids expand much more rapidely than their external walls, causing the latter to be progressively squizzed between empty regions, forming shell-like structures. If the initial underdensities are too deep and the matter walls too thin, two external shells might eventually be forced to occupy the same physical position - causing a shell-crossing. It is important to note that nothing particulay happens to the photons passing through such features, except that they simply go through several shells at the same time. Although some regard this phenomenon as unphysical [74, 75], treating shell-crossing singularities as physical entities is perfectly sensible if one interpretes them as rims of expanding voids [76, 77].

For practical reasons, however, we choose to discard solutions in which shell-crossing occurs. Such events can be detected very easily, based on the value of the spatial derivative of the scale factor $R'(r,t)$: there is shell overlaping when

$$R'(r,t) = 0.$$

It then is straightforward to check for this condition throughout the metric and discard the situations in which it is observed.

10.4 Research for Optimal Central Void Models

10.4.1 Monte Carlo Markov Chain

Our aim is to determine the central void model which allows for the best possible fit of the SN Ia observations. As we are considering a complex parameter space with a large number of degrees of freedom, we choose to implement a complete Monte Carlo Markov Chain (MCMC). MCMC methods are a combination of two statistical approaches, Monte Carlo methods and Markov chains (cf. below). They form a family of algorithms for sampling from probability distributions.

Monte Carlo Methods

Monte Carlo methods can be loosely described as statistical simulation methods, i.e. methods which utilize sequences of random numbers to perform simulations. As computational algorithms, they are generally used when computing an exact result with a deterministic algorithm proves to be too complicated or infeasible. These methods are especially useful for simulating systems with many degrees of freedom and to evaluate complex integrals in mathematics [78]. But they have been applied successfully to many domains: nuclear reactor design, quantum chromodynamics, traffic flow, econometrics, Dow-Jones forecasting, etc.

The main components of a Monte Carlo algorithm are the following[1]:

- *Probability distribution functions* (PDFs), the physical or mathematical system must be described by a set of PDFs;
- *Random number generator*, a sequence of random numbers which are uniformly distributed on the unit interval;
- *Sampling rule*, a prescription for sampling from the specified PDFs, assuming the availability of the random numbers generated;
- *Scoring*, the outcomes must be accumulated into overall scores for the quantities of interest;
- *Error estimation*, an estimate of the statistical error (variance) as a function fo the number of trials and other quantities;
- *Variance reduction techniques*, methods for reducing the variance in the estimated solution in order to reduce the computational time.

Markov Chains

In the family of discrete-time random processes, Markov chains are mathematical systems which undergo transitions between a 'chain' of state, accordingly to the Markov property: the conditional probability distribution for the system at the next step depends only on its current state and not on the state of the system at previous steps. They have many applications as statistical models in real-world, mathematical and physical processes. Since the system described by a Markov chain changes its state at each step, it is usually impossible to predict exactly its state in the future, only its statistical properties can be predicted.

Formally, a Markov chain is a sequence of random variables $X_1,\ X_2,\ X_3, \ldots$ with the Markov property, i.e. given the present state, the future and past states are independant:

$$\Pr\left(X_{n_{+1}} = x \,|\, X_1 = x_1,\ X_2 = x_2, \ldots,\ X_n = x_n\right) = \Pr\left(X_{n+1} = x \,|\, X_n = x_n\right).$$

The possible values of X_i form a countable set S called the state space of the chain.

10.4.2 Metropolis-Hastings Algorithm

A particular type of MCMC method is know as Metropolis-Hastings algorithm [79]. It usually draws samples from any probability distribution $P(x)$, requiring only that a function proportional to the density can be calculated. The algorithm generates a Markov chain in which each state x_{t+1} depends only on the previous state x_t. It uses a *proposal density* $Q\left(x'; x_t\right)$, related to the current state, to generate a new proposed sample x'. A random value α is then drawn between 0 and 1. The new proposal becomes the next step if the following relation if satisfied:

$$\alpha < \frac{P\left(x'\right) Q\left(x_t; x'\right)}{P\left(x_t\right) Q\left(x'; x_t\right)}.$$

[1] Computational Science Education Project (http://www.phy.ornl.gov/csep).

If the proposal is not accepted, the current value of x stays unchanged and a new proposal is made and tested. The ratio $Q(x_t; x')/Q(x'; x_t)$ is equal to 1 if the proposal density is symmetric - which we will assume here. Some random initial value x_0 is chosen as starting point and the Markov chain is run for many iterations until this initial state is 'forgotten'. These discarded samples are called *burn-in*. The accepted steps represent of sample for the distribution $P(x)$.

One obtains better results with the Metropolis-Hastings algorithm if the proposal density matches the shape of the target distribution $P(x)$. If one chooses a Gaussian proposal density Q, one has to tune the variance parameter σ^2 during the burn-in period. The common way of controling it is to consider the *acceptance rate*, which is simply the fraction of the accepted steps for a given number of samples. If σ^2 is too small, the chain will mix slowly, which means that the successive samples will move safely but inefficiently around the space. If σ^2 is too large, the proposals are more likely to be picked in low probability density regions and the chain will also converge very slowly.

10.4.3 Application to Our Study

Our intention is to implement a Monte Carlo Markov Chain based on the Metropolis-Hastings algorithm in order to search for optimal central void models.

Aiming at a large flexibility for the void geometry and the cosmological parameters, we propose to consider eight variables which will be chosen independently from each other at each step of the MCMC. Some practical constraints need to be fixed so that we make sure to avoid unphysical or irrelevant situations (cf. Table 10.3). These restrictions allow us as well to reduce the frequency of shell-crossing events (see Subsection 10.3.2) and to provide proper initial conditions for the numerical integration.

Variable	Parameter	Constraints
r_1	Internal radius	$r_1 > 0.2\, r_2$ and $r_1 > 10$ Mpc
r_2	External radius	$r_1 < 0.9\, r_2$ and $r_2 < 5000$ Mpc
A_1	Density profile	$A1 < 1$ and $A1 > 0.99$
r_0	Observer's position	$r_0 > 1$ Mpc and $r_0 > r_1$
θ_{RA}	Observer's right ascension	*None*
θ_{Decl}	Observer's declinaison	*None*
H_0	Hubble parameter	*None*
Ω_m	Matter density	$0 < \Omega_m < 1$

Table 10.3: Free MCMC parameters for the void geometry and the cosmological background, with their respective constraints.

At every step, new values for all parameters are generated following a random Gaussian distribution around the previous values. The *temperatures*, i.e. the width of Gaussian probability distribution around its mean, are not necessarily chosen as proportional to the parameter value. They are rather adjusted in order to obtain reasonable acceptance rates. In order to fix initial conditions and temperatures wisely, we refer to previous studies in the literature [52, 58,

68, 80, 81, 82, 83]. These give precious indications on the void size needed and on the allowed off-centre distance of the observer.

For every model generated, we calculate the χ^2 value, summing the individual discrepancies between the simulated distance modulus and its observed value, as explained in Subsection 10.3.1. However, the number of degrees of freedom (557 SNe Ia) is much too large for us to directly compare the resulting χ^2 values. In order to obtain comparable results, we need to the cumulative distribution function of the χ^2 distribution:

$$F(x;k) = \frac{\gamma(k/2, x/2)}{\Gamma(k/2)}, \tag{10.20}$$

where $\Gamma(x)$ is the Gamma function and$\gamma(x, y)$ the lower incomplete Gamma function, expressed as:

$$\Gamma(x) = \int_0^\infty t^{x-1} e^{-t} dt,$$

$$\gamma(x, y) = \int_0^y t^{x-1} e^{-t} dt.$$

In Eq. (10.20), x is identified as the calculated χ^2 and k as the number of degrees of freedom.

Chapter 11

Results and Discussion

After some brief comments on numerical aspects, we will present here the main results obtained from our research. They will be grouped according to their underlying paradigm: first the influence of the Swiss-Cheese Universe on the estimates of the DE equation of state; then applications of central void models.

11.1 Notes on Numerical Results

11.1.1 Obtaining Redshifts and Distance Moduli

In order to compare the various models of Universe we intend to create, we need to build Hubble diagrams which allow us to analyse the discrepancies between models and Type Ia Supernoae data. In order to do so, one must obtain the redshift of distant sources situated around the void and then calculate the corresponding distance modulus.

Our strategy is to send two photons through the void from the same initial position $r_{\rm in}$ but at two different times $t_{\rm in}$ and $t'_{\rm in} = t_{\rm in} + \Delta t_{\rm in}$. We first follow the path of the first photon until the value of $t(r)$ reaches the present time, $t(r_{\rm fin}) = t_{\rm now}$. The corresponding comoving coordinate serves as ending point for the evolution of the second photon. We thus obtain $\Delta t_{\rm fin} = t(r_{\rm fin}) - t_{\rm now}$. The redshift is then simply given by $z(r_{\rm in}, t_{\rm in}) = \Delta t_{\rm fin}/\Delta t_{\rm in} - 1$. The luminosity distance is then given by

$$d_L = (1+z)^2 R(r_{\rm final}, t_{\rm now}) = a_0 r_{\rm obs}(1+z),$$

where a_0 is the value of the scale factor today and $r_{\rm obs} = r_{\rm fin} - r_{\rm in}$. To produce our Hubble diagrams, we consider the distance modulus $\mu = 5 \cdot \log_{10}(d_L/10 \text{ pc})$.

Our simulation strategy is built on the fact that we cannot choose a particular position for the sources in the void profile since we do not know it *a priori*. We indeed have to assume a random distribution of the sources within the void and its surroundings. The random initial positions are chosen in the 3-dimensional spherical void and their coordinates are projected on the axis defined by the photon path.

Avoiding arbitrary choice through this approach, we must however guarantuee a consistent statistical treatment to the resulting clouds of data (Fig. 11.1). The process in question is described in the next Subsection.

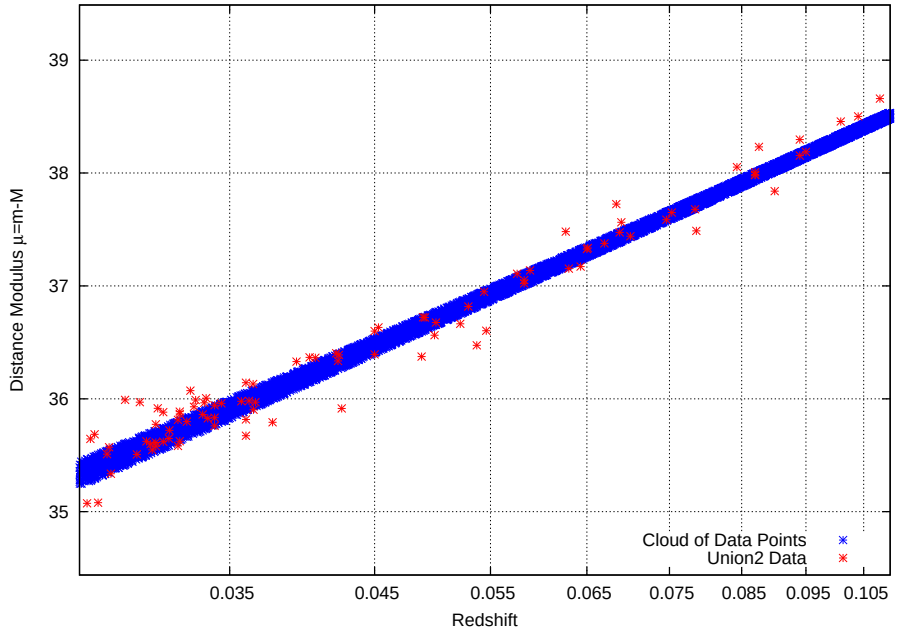

Figure 11.1: 'Cloud' or stripe of data points generated by the random positions of the sources with respect to the spherical void. The graph shows the simulated distance modulus μ versus redshift z of several thousands samples, compared to Union2's observational data.

11.1.2 Statistics: Binning Process

The aim of the binning process is to gather series of points given by simulations in order to deduct sensible observations from them. Given the range covered by the redshift, $0.01 < z < 2$, we choose to distribute the 10^5 data points between 200 bins of width $\Delta z = 0.01$ (Fig. 11.2). For each bin obtained, the mean and standard deviation are calculated (Fig. 11.3). We thus end up with a new series of points and corresponding errorbars which we can now compare to observations.

The Type Ia Supernovae data used in this study are extracted from the Union2 Compilation [33] of the Supernova Cosmology Project, which contains 557 sources drawn from 17 datasets. We base our comparison on the file called "Union2 Compilation Magnitude vs. Redshift Table"[1], which is an ASCII table with tab-separated columns: supernova name, redshift, distance modulus, and distance modulus error. To the latter we add the systematic error due to the peculiar velocities of the host galaxies, $\sigma_v = 400$ km/s, converted into a systematic error on the redshift of $\delta z = 0.00132$.

Once all data are binned and all errors known, we can compute χ^2 values for every combination $(\Omega_m, \Omega_\Lambda)$. In parallel, we do the same for all FRW Universes defined by the same density parameters.

[1] http://www.supernova.lbl.gov/Union

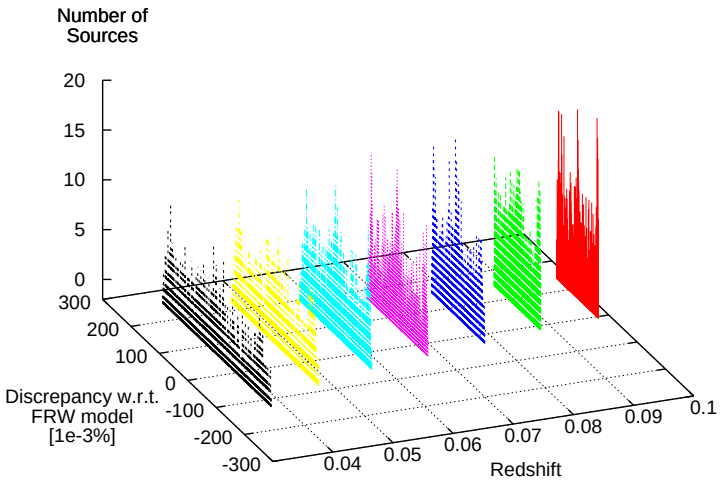

Figure 11.2: Illustration of the binning process allowing us to deal with the statistical nature of our results. The width of each bin is fixed in redshift, $\Delta z = 0.01$.

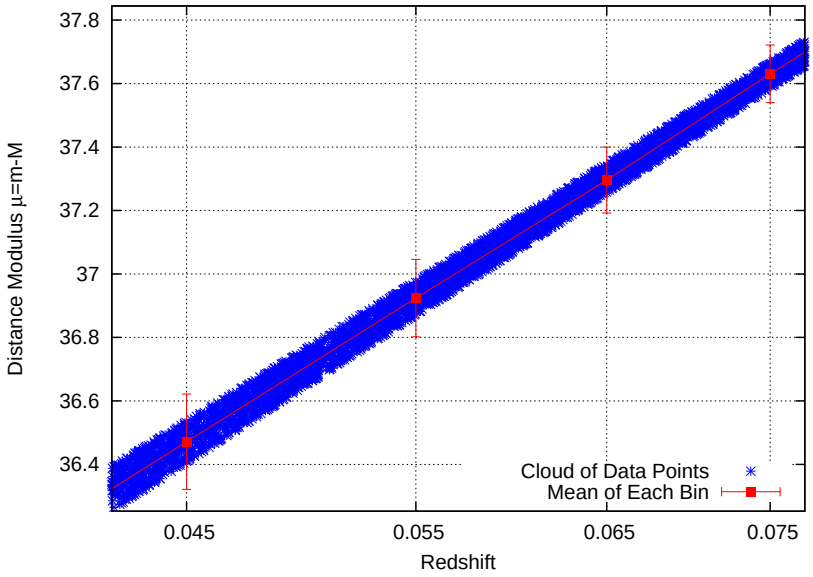

Figure 11.3: Calculated mean for selected data bins between $z = 0.045$ and 0.075.

11.1.3 Comparison of Errors

In order to compute consistent χ^2 values, we ought to take into account all the errors and uncertainties adding up for each source considered and which can be split into two categories: error on distance modulus, σ_μ, and binning process uncertainty, $\sigma_{\rm BP}$, so that

$$\chi^2 = \sum_{\rm SNe} \frac{\left[\mu_{\rm mean}(z) - \mu_{\rm meas}(z)\right]^2}{\sigma_\mu^2 + \sigma_{\rm BP}^2}.$$

Error on Distance Modulus

This first group gathers the variety of measurement errors due to the very nature of the sources and the way their luminosity is evaluated. Accordingly to the Union2 original paper [33], we sum in this component errors coming from the following causes: light curve fitting (through covariant matrix), galaxy peculiar velocities, galactic extinction, gravitational lensing and a floating dispersion term (for potential sample-dependent systematic errors).

All these errors are included in the error on distance modulus given by the Union2 Compilation data.

Binning Process Uncertainty

In the second group of errors, we chose to put the uncertainties related to the spread induced by the voids themselves. Here the error comes from the binning process itself, where we combine results of simulation for a large number of different sets of initial conditions.

For each bin created at a given redshift z, we determine the standard deviation of the data by evaluating the spans from the mean value that include 68% of all the points in the bin. The corresponding deviation, $\sigma_{\rm BP}(z)$, is then simply added in quadrature to the total uncertainty.

11.2 Estimates of the Equation of State

Our aim is to estimate the magnitude of the error implied by the inhomogeneities on the equation of state of Dark Energy. We will consider two different situations: Dark Energy as a cosmological constant, providing a constant value for w (Subsection 11.2.1), and a dynamical equation of state, $w(z)$, varying over time (Subsection 11.2.2).

11.2.1 Dark Energy with Constant Equation of State w

Having estimated the errors due to the growth of voids in the Universe, we are in a position to find out how this effects the reconstruction of the equation of state. To do this we perform a Monte Carlo Markov Chain (MCMC) fitting to the data. We assume a flat Universe and generate values of Ω_m (and therefore $\Omega_{DE} = 1 - \Omega_M$) and w randomly. For all fits in this paper we remove uncertainty in the Hubble constant by choosing the best fit value for each value of Ω_m. We also calculate the probability from the χ^2 values using the χ^2 cumulative distribution function rather than relative χ^2 values as an estimation of maximum likelihood.

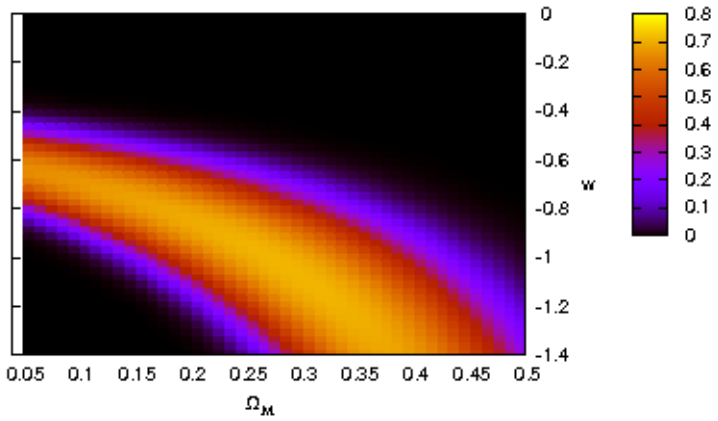

Figure 11.4: Ω_M vs Dark Energy equation of state w when fitting the Union2 data set only assuming a flat Universe. The shading represents probability from the χ^2 cumulative distribution function.

z_{min}	Smooth	With Voids	$\lvert\Delta w\rvert$
0.01	$-1.480^{+0.631}_{-1.005}$	$-1.613^{+0.740}_{-1.189}$	0.133
0.02	$-1.574^{+0.706}_{-1.125}$	$-1.662^{+0.776}_{-1.250}$	0.088
0.03	$-1.727^{+0.819}_{-1.320}$	$-1.823^{+0.889}_{-1.422}$	0.096
0.04	$-2.017^{+1.006}_{-1.678}$	$-2.056^{+1.028}_{-1.748}$	0.039

Table 11.1: The best fit for the equation of state of Dark Energy w to the Union2 supernova data set alone with the 67% errors. The fits are done for different minimum redshifts and with and without the additional errors created by the presence of voids. The fourth Column is the difference between the two best fit values. Note the general trend of the difference in errors going down as we cut out lower redshift supernovae (apart from when we go from $z_{min} = 0.02$ to $z_{min} = 0.03$ which must be a statistical fluctuation).

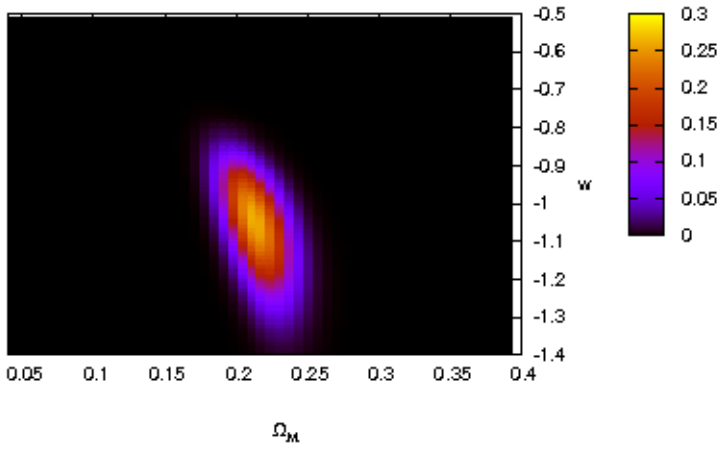

Figure 11.5: Ω_M vs Dark Energy equation of state w when fitting the Union2 data set, baryon acoustic oscillations and the shift parameter and acoustic scale of the CMB, again assuming a flat Universe. The shading represents probability from the χ^2 cumulative distribution function.

First we fit the supernova data alone. Typical favoured regions in the $\Omega_M - w$ plane can be seen in figure 11.4. Table 11.1 shows the projected constraints on the equation of state with and without the presence of the additional error due to voids. We have done MCMC runs for the supernova data sets with various minimum redshifts. When fitting to data, it is normal to cut out very small redshift supernova since they are the data points most vulnerable to large redshift errors such as peculiar velocities. Given that we expect the void effect to be at most the same magnitude as these other errors, we perform fits to the data with and without the voids neglecting supernovae below different minimum redshifts - $z_{min} = 0.01$, 0.02, 0.03 and 0.04. As expected, the discrepancy between the simulations with and without voids decreases as we increase the minimum redshift.

The constraint on the value of w when only including the supernova data is very weak and best fit values are quite far from $w = -1$. This regime is therefore far from the region of validity of our analysis - the growth of voids in such a Universe might be quite different to the LTB case due to structure formation in the Dark Energy and anisotropic pressure which in general is a challenge to calculate. However, we make no apologies for this as we only seek to highlight the possible magnitude of void effects upon the reconstruction of the equation of state in this work.

Next we include the effective distance measure D_V which is obtained from the SDSS Baryonic Acoustic Oscillation data [63, 15] and the WMAP constraint on Dark Energy from the shift parameter R and the acoustic scale l_A [64]. The favoured regions on the $\Omega - w$ plane can be seen in figure 11.5. These lead to much tighter constraints on possible values of w and the difference between the case with and without voids is much smaller.

We note here that we obtain slightly different constraints on the equation

z_{min}	Smooth	With Voids	$\lvert\Delta w\rvert$
0.01	$-1.064^{+0.116}_{-0.126}$	$-1.072^{+0.127}_{-0.139}$	0.008
0.02	$-1.073^{+0.122}_{-0.132}$	$-1.078^{+0.129}_{-0.141}$	0.005
0.03	$-1.097^{+0.131}_{-0.143}$	$-1.101^{+0.134}_{-0.147}$	0.004
0.04	$-1.128^{+0.134}_{-0.148}$	$-1.129^{+0.135}_{-0.149}$	0.001

Table 11.2: The best fit for the equation of state of Dark Energy w to the Union2 supernova data set, CMB and BAO, as described in the text, with the 67% errors. The fits are done for different minimum redshifts and with and without the additional errors created by the presence of voids.

of state to the analyses carried out in [33], which is probably mostly due to the way we marginalise over the Hubble constant. The basic preferred regions are compatible in the two studies.

11.2.2 Dark Energy with Dynamic Equation of State $w(z)$

So far, we have considered a constant value for the equation of state parameter w. It is however possible that the Dark Energy equation of state might vary over time and therefore redshift. A very commonly used parametrization of dynamic Dark Energy is

$$w = w_0 + w_a \frac{z}{1+z},$$

based on works by Chevallier, Polarski and Linder [65, 66]. Following the same procedure as before, we fit the supernovae data while taking into account the constraints given by the CMB and the BAO. The results for the best fits are given in Table 11.3.

z_{min}	w_i	Smooth	With Voids	$\lvert\Delta w_i\rvert$
0.01	w_0	$-0.523^{+0.457}_{-0.320}$	$-0.492^{+0.662}_{-0.636}$	0.031
	w_a	$-2.993^{+6.956}_{-2.672}$	$-3.223^{+8.166}_{-2.938}$	0.230
0.02	w_0	$-0.515^{+0.587}_{-0.343}$	$-0.424^{+0.426}_{-0.402}$	0.091
	w_a	$-3.064^{+5.037}_{-2.572}$	$-3.660^{+7.097}_{-3.096}$	0.596
0.03	w_0	$-0.444^{+0.395}_{-0.394}$	$-0.475^{+0.558}_{-0.417}$	0.031
	w_a	$-3.488^{+6.608}_{-2.686}$	$-3.272^{+5.751}_{-3.025}$	0.216
0.04	w_0	$-0.483^{+0.953}_{-0.412}$	$-0.493^{+0.489}_{-0.427}$	0.010
	w_a	$-3.173^{+5.173}_{-2.756}$	$-3.076^{+5.451}_{-2.798}$	0.097

Table 11.3: The best fit for the dynamic equation of state of Dark Energy $w = w_0 + w_a \frac{z}{1+z}$ to the Union2 supernova data set, CMB and BAO, with the 67% errors. The fits are done for different minimum redshifts and with and without the additional errors created by the presence of voids.

Even with the extra degree of freedom, the fits obtained when including the whole set of supernovae down to arbitrai;y small redshifts are not fantastic, the probability obtained from the χ^2 distribution of the best fit point in parameter

space being less than 50%. However, the situation changes dramatically depending on the redshift considered for the cut-off: the best fit probability comes close to 1 with $z_{min} = 0.04$. Fig. 11.6 shows the contour plots obtained for the different values of z_{min} studied here.

It is clear again that if we include the lowest redshift supernovae, the error which is introduced due to the presence of voids has a considerbale impact on the best-fitting regions in $w_o - w_a$ parameter space.

11.3 Results for Central Void Models

As for the Swiss Cheese Universe, our intention is to compare the central void models to the standard reference provided by ΛCDM. We do so by fitting Union2's supernovae data with the simulated cosmologies and calculating the resulting χ^2 values. The statistical approach of the Monte Carlo Markov chain allows us to investigate the landscape of different parameter configurations and determine the favoured regions of the parameter space.

11.3.1 Best Configurations on the Parameter Space

We undertake a series a simulation runs presenting different profiles, with a particular set of initial conditions and specific variation steps. Starting from various positions in the parameter space assures that build a consistent larger picture of the situation; it prevents us from dwelling in special regions while forgetting to explore others. This is further guaranteed by a wide range of parameter temperatures, which allow the Metropolis-Hastings algorithm to reach yet untouched regions and assert their relevence.

Table 11.4 shows three sets of simulations with their specific characteristics. All initial conditions have been chosen relatively close to the apparently most favoured region of the parameter space, as the large number of degrees of freedom severely hinders the MCMC process. The guessed values for the starting points as well as the temperatures are deduced from series of test simulation runs and adjusted consequently.

As can be seen from the results, the average χ^2 value per degree of freedom is comparable to a fiducial ΛCDM with $(\Omega_m, \Omega_\Lambda) = (0.27, 0.73)$, for which $\chi^2_{\mathrm{dof}} \lessapprox 1$ (e.g. [84, 85, 86]). The various simulation runs, independently from their MCMC parameters, point consistently towards prefered regions of the parameter space. This can be clearly observed when plotting certain variables with respect to each other, e.g. the Hubble parameter H_0 and the geometrical parameter of the void r_2 (Fig. 11.7), or the underdensity parameter A_1 versus the inner radius r_1 (Fig. 11.8).

The results provided by the MCMC approach make sense in a statistical interpretation, but it is also possible to extract from them individual simulations with particular interest. Thus, among the best configurations, one can identify the optimal case where the χ^2 value becomes comparable to ΛCDM values. Fig. 11.10 shows the Hubble diagram of the best fit obtained in Run 2, compared to the latest SNe Ia data and a standard ΛCDM. The corresponding parameters are listed in Table 11.5.

The results presented here aimed at illustrating the possibilities offered by central void models. They provide us with an alternative perspective on cos-

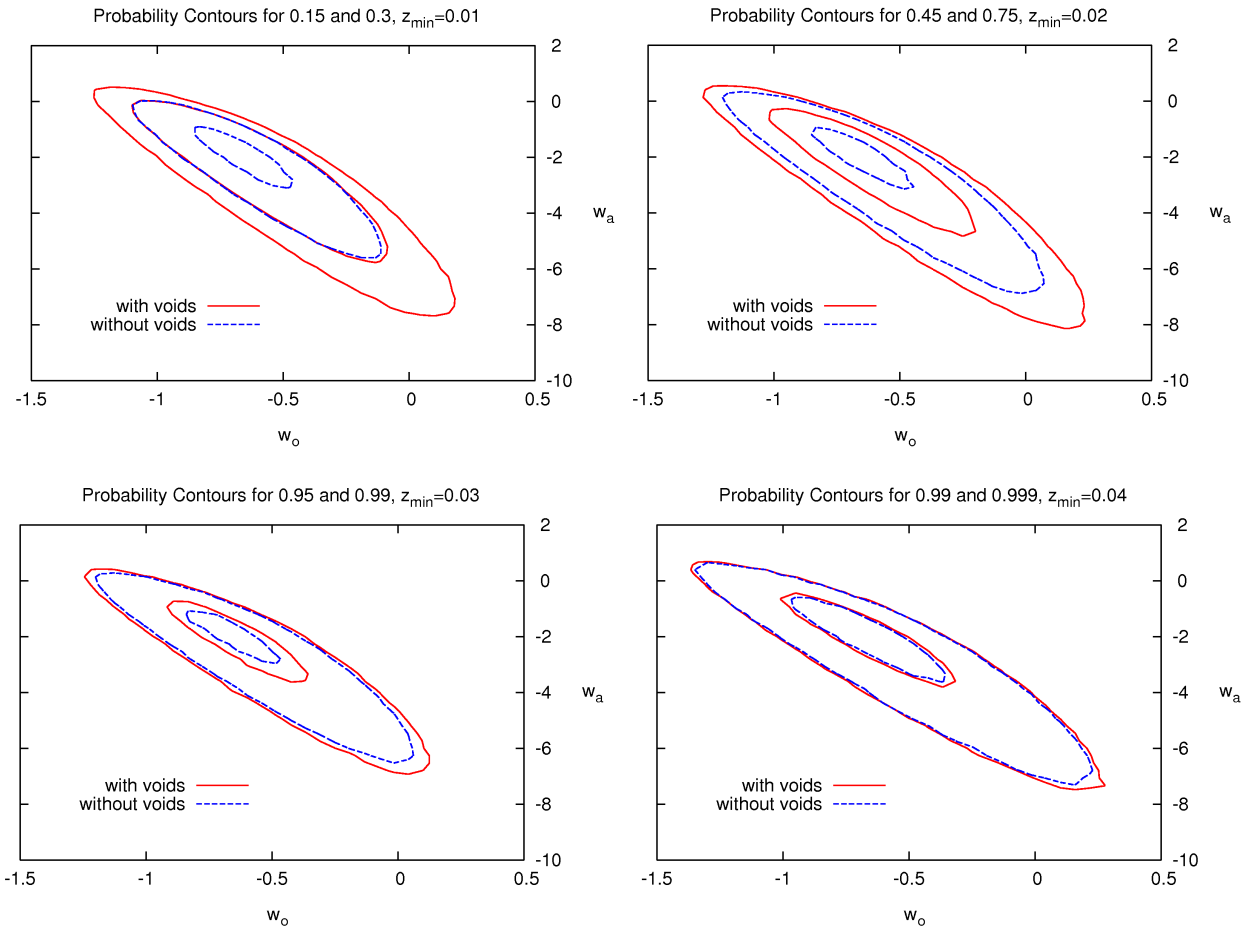

Figure 11.6: Dark Energy equation of state parameters w_0 versus w_a, with $z_{min} = 0.01, 0.02, 0.03$ and 0.04 respectively, when fitting the Union2 data set, Baryon Acoustic Oscillations and the shift parameter and acoustic scale of the CMB, always assuming a flat Universe. The contours correspond to the probabilities listed in the individual graph titles.

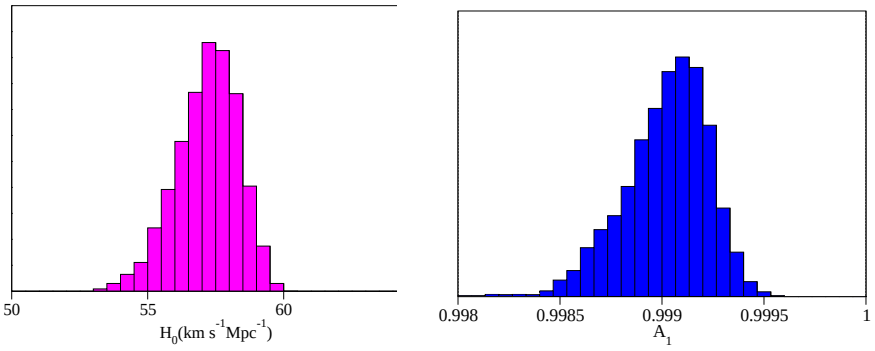

Figure 11.7: Histograms for the simulated void models for Run 2 as defined in Table 11.4. The results for the Hubble parameter are consistent with other measurements shown in Fig. 11.9, given that the actual value measured inside the void would be about 25% higher.

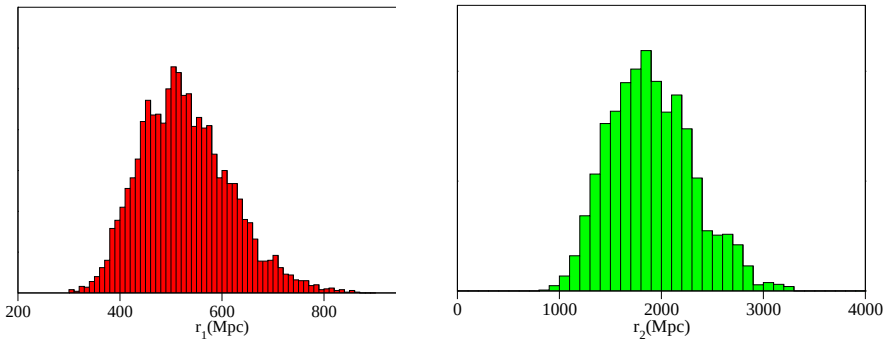

Figure 11.8: Same legend as in Fig. 11.7, but this time showing the histograms for the internal and external radii of the void, r_1 and r_2.

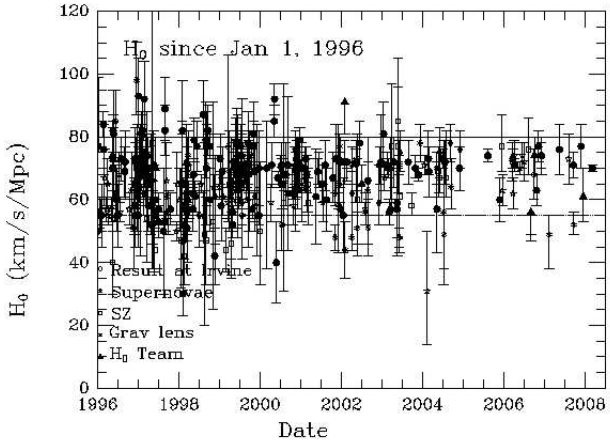

Figure 11.9: Sum of all the data (not all independent) for the Hubble parameter H_0 available since 1996 [89].

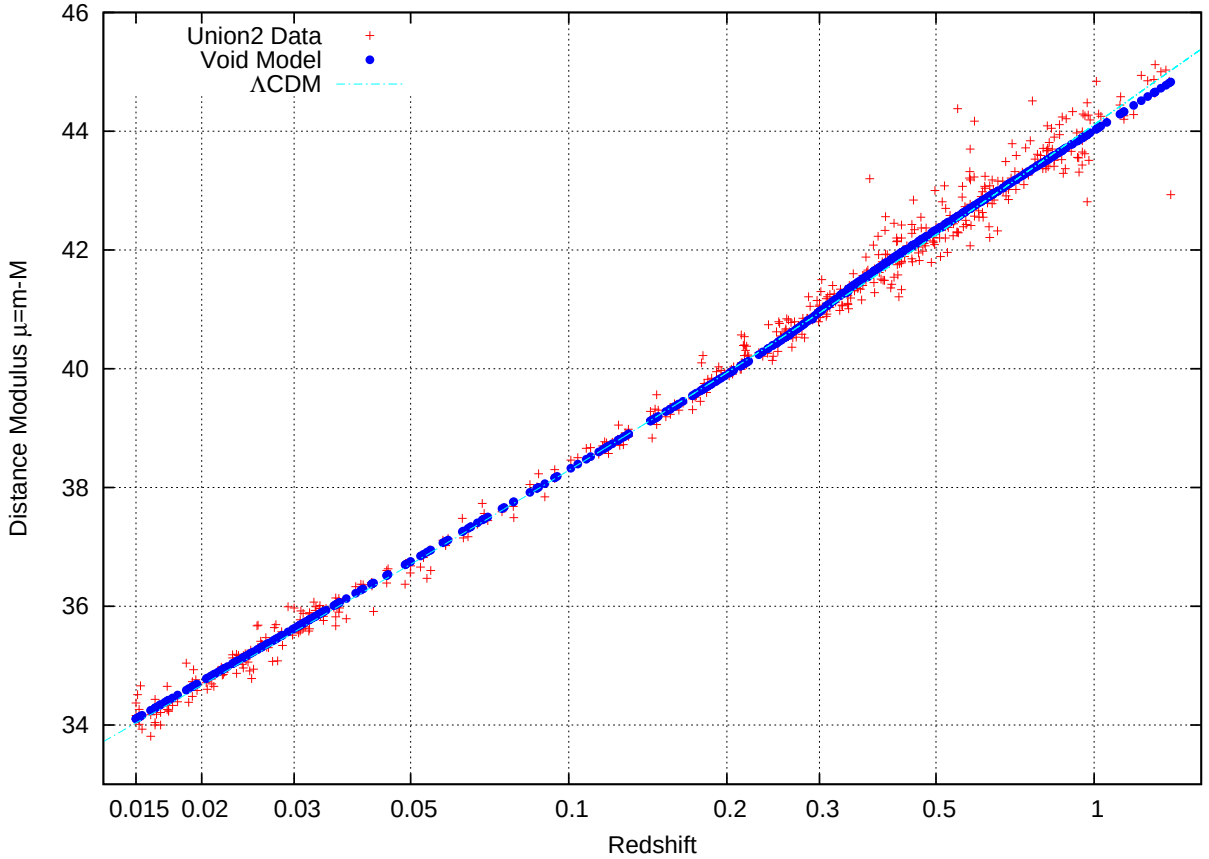

Figure 11.10: Hubble diagram for one of the best void model ($\chi^2 = 574.7$), compared with the Union2 supernovae data and a fiducial ΛCDM (with $\Omega_m = 0.27$, $\Omega_\Lambda = 0.73$ and $H_0 = 71$ km/s/Mpc). The change in the slope at redshift $z \approx 0.3$ is caused by the photons going through the wall surrounding the central underdensity.

Selection of Simulation Runs for Central Void Models			
Par.	Run 1	Run 2	Run 3
r_1	700[±20] Mpc	690[±30] Mpc	660[±40] Mpc
r_2	1460[±60] Mpc	1400[±70] Mpc	1630[±80] Mpc
r_0	27.4[±3] Mpc	37.6[±5] Mpc	25.5[±7] Mpc
A_1	$0.99908[\pm 8 \times 10^{-5}]$	$0.9999[\pm 10 \times 10^{-5}]$	$0.9998[\pm 20 \times 10^{-5}]$
θ_{RA}	$9.224[\pm 5] \times 10^{-4}$	$8.579[\pm 10] \times 10^{-4}$	$9.969[\pm 15] \times 10^{-4}$
θ_{Decl}	$3.206[\pm 5] \times 10^{-4}$	$3.278[\pm 10] \times 10^{-4}$	$2.082[\pm 15] \times 10^{-4}$
H_0	$58.35[\pm 5 \times 10^{-4}]$	$59.75[\pm 10 \times 10^{-4}]$	$58.91[\pm 15 \times 10^{-4}]$
Ω_m	$0.999903[\pm 3 \times 10^{-4}]$	$0.999936[\pm 5 \times 10^{-4}]$	$0.999944[\pm 7 \times 10^{-4}]$
AR	54.3%	41.4%	26.8%
$\langle \chi^2 \rangle$	635.55	613.37	613.98
$\langle \chi^2_{\mathrm{dof}} \rangle$	1.141	1.101	1.102

Table 11.4: MCMC parameters for three simulations runs with specific initial conditions and temperatures (within square brakets). The results of the simulations are given in terms of the acceptence rates (AR), average χ^2 values of the run $\langle \chi^2 \rangle$ and average χ^2 values per degree of freedom $\langle \chi^2_{\mathrm{dof}} \rangle$. No flatness of the Universe is assumed, as Ω_m can vary freely within its predefined boundaries (Table 10.3). The Hubble parameter H_0 is given in km/s/Mpc and corresponds to the value outside the underdensity.

Void Parameters (Run 2)	
Par.	Values
r_1	770 Mpc
r_2	3780 Mpc
r_0	46.47 Mpc
A_1	0.99889779
A_2	0.00110170
A_3	0.00002448
θ_{RA}	0.01194834
θ_{Decl}	0.00144922
H_0	54.85
Ω_m	0.99837825
χ^2	574.66
χ^2_{dof}	1.032

Table 11.5: Void geometry and cosmological parameters for the best fit obtained in Run 2. This particular configuration, with an extended but rather shallow wall, produces a χ^2 of less than 575 for 557 supernovae. As always, H_0 is in units km/s/Mpc.

mology and allow us to question the generally accepted paradigms. In order to give a consistent analysis, one would need to consider all the cosmological and astrophysical contraints related to our study. In particular, this means that the external and internal radii of the void and the observer's position must satisfy conditions discussed in details in the literature (e.g. [58, 68]). As well as for

the Hubble parameter, the values determined by our fitting process could be accommodated by current observations. It is worth noting that the value of H_0 increases inside the void, since the underdense region expands more rapidly. In the case of Run 2's best fit, for instance, an external value of $H_0 = 54.85$ km/s/Mpc gives an sensibly higher internal value of $H_0 = 68.44$ km/s/Mpc, which is compatible with the latest measurements of the Hubble parameter [87, 88].

11.3.2 Application to the Extragalactic Background Light

Our goal, however, when undertaking these MCMC simulations of central void models, was not to reproduce results already existing about the possibility of substituting Dark Energy for the mimicking effect of a large underdensity. We were rather interested in building models which we could use for other purposes. One of the possible applications is the study of their impact on our understanding of the Extragalactic Background Light. We will briefly describe here the phenomenon and present some interesting results.

The Extragalactic Background Light

Stars are formed continuously throughout the history of the Universe. Some of the first stars (the ones with low masses) are still burning after 10^{10} years, whereas stars with masses larger than 10 $M_\odot$ lasting less than a few million years on the main sequence. The larger stars are more short lived, but much more luminous and also bluer. The continual life cycle of stars throughout the history of the Universe creates a background radiation in addition to the CMB. While there are much fewer photons from stars compared to the CMB photons, they are bluer and a lot of the starlight fails to exit the dust in galaxies and is re-emitted in the infrared. This Extragalactic Background Light (EBL) therefore creates a spectrum of light from the ultra-violet to the far end of the infrared band, up until the point at which the CMB starts to dominate.

Because this background light is made of starlight, and we are surrounded by stars, it is rather difficult to observed. Nevertheless, there are lower limits on its magnitude across the whole range of frequencies due to galaxy counts and positive detections (see references in Fig. 11.11). It is therefore possible to reconstruct the evolution and history of this radiation field using a combiantion of the spectrum which is observed here on earth as well as the star formation history.

We do this following closely the simplified approach of [90] with a particular numerical implementation which lends itself to different expansion histories. According to their calculations, the overall spectrum of energy density $u_{ebl}(\epsilon, t)$ at $t = t_0$ is given by

$$\epsilon u_{ebl}(\epsilon, t_0) = \epsilon \int_{t_{start}}^{t_0} \dot{\rho}[z(t)] \left\{ \tilde{j}_{*part}(\epsilon, t_0, t) + \tilde{j}_{d-part}(\epsilon, t_0, t) \right\} dt \qquad (11.1)$$

where $\epsilon = h\nu/m_e c^2$ is the dimensionless photon energy, $\dot{\rho}(z)$ is the star formation rate in units of solar masses per unit time per unit volume; $\tilde{j}_{*part}$ is the energy emitted per solar mass of a particular stellar population created at time t over its lifetime up to the time of the observer t_0; $\tilde{j}_{d-part}$ is similarly defined, but

for the re-emitting dust components. To calculate the opacity of the Universe to photons we use

$$\tau(t) = \int_t^{t_0} \int_0^{\infty} c\sigma(2\epsilon E_\gamma(1+z(t'))^2) \frac{u_{EBL}(\epsilon, t')(1+z(t'))^3}{\epsilon m_e c^2} d\epsilon dt \tag{11.2}$$

where E_γ is the energy of the gamma ray at $t = t_0$ and $\sigma(y)$ is the cross section for electron-positron pair production:

$$\sigma(y) = H(2y)\pi r_e^2 \left\{ (1-\beta^2)(3-4\beta^4) \ln\left[\frac{1+\beta}{1-\beta}\right] - 2\beta(2-\beta^2) \right\} \tag{11.3}$$

where $y = s/m_e^2 c^4$ is the dimensionless centre of mass energy, $\beta = \sqrt{(}1 - 2/y)$ and σ_T is the Thomson cross section, $H(x)$ is the heavyside step function.

The attenuation in photons (i.e. the probability of them getting through from a given time t) is then given by $P = \exp(-\tau(t))$. We use the results of [91] to estimate the temperature and luminosity of stars as a function of time to build up the spectrum of a population of stars coming from this initial mass function at any given time. We implement infrared absorption and re-emission in the host galaxy. Then we integrate the stars that are produced througout the history of the Universe to obtain the spectrum at any given redshift given the star formation rate

$$\dot{\rho}_* = \frac{a + bz}{1 + (z/c)^d} \tag{11.4}$$

and we fit the values of a, b, c and d to fit both the observational constraints on $\dot{\rho}$ and the spectrum at $z = 0$. The data for the star formation rate evolution over time is taken from [92].

The procedure is then the following:

1. We take one of the void cosmologies which fits the supernova data from the Markov chain.
2. We convert this into a look-up table between redshift and lookback time.
3. We then apply the appropriate rescaling to the $\dot{\rho}_*$ data to make up for the different between this particular cosmology and the ΛCDM cosmology assumed in [92].
4. We then vary the parameters a, b, c and d in order to fit the re-scaled star formation rate data and the $z = 0$ spectrum.

By finding a good fit using this method, we are able to reconstruct the EBL spectrum at any redshift. We find it is possible to reconstruct the $z = 0$ spectrum and the star formation rate history with a reasonable fit.

We have therefore introduced two new pieces of data and shown that they cannot on their own discriminate between the void cosmologies and ΛCDM. However, by moving to a new cosmology, we have changed the relationship between redshift and time, so the physical photon density at any given redshift is actually different in the past in the two cosmologies in order to explain the data today. This is critical for the propagation of TeV energy gamma rays.

It has long been known that ultra high energy gamma rays would not be able to go very far in the Universe as if they have an energy of more than around 10^7 GeV they would pair-produce electrons and positrons off the $\sim 10^{-4}$ eV CMB photons. Since we need to increase the physical density of EBL photons in void Universes in order to explain the data, we are reducing the mean free path of TeV photons and we should not see them coming as abundantly from objects at very large distances.

Observations from gamma-ray detectors show that TeV gamma rays are arriving from blazars at truly cosmological distances. This is done by looking at the shape and position of the break in the power law spectrum of emission. Comparing our theoretical models with the observed limits allow us to either rule out some of them, or to confirm their consistency with observational evidences (Fig. 11.12 and 11.13).

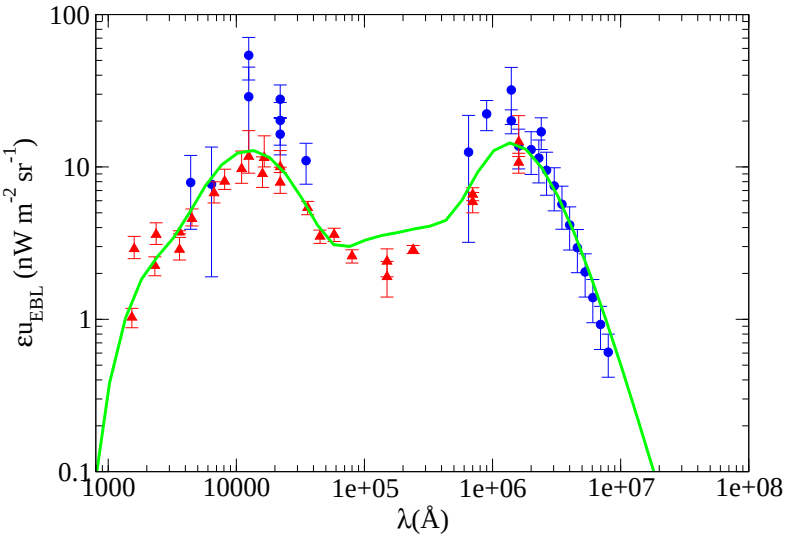

Figure 11.11: Our model for the Extragalactic Background Light plotted alongside measurements and constraints from observations: actual detections (*blue dots*) [93, 94, 95, 96, 97, 98, 99, 100] and lower limits (*red triangles*) [101, 102, 103, 104, 105, 106].

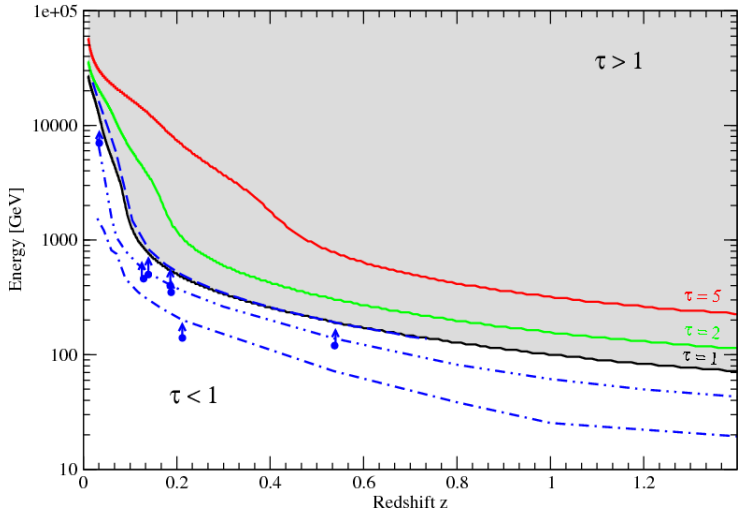

Figure 11.12: Gamma-ray horizon $\tau = 1,\ 2$ and 5 for the lower limit EBL model derived in [107]. Observed limits (*blue dots*) are taken from [108]. Other EBL models are shown for comparison (*blue lines*), from bottom: Stecker [109], Albert [108] and Primack [110].

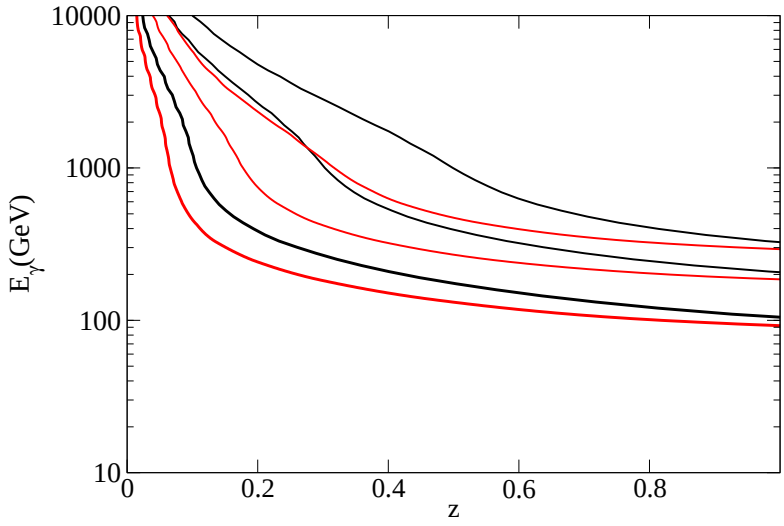

Figure 11.13: Gamma-ray horizons with $\tau = 1,\ 3$ and 5 (from bottom to top), for ΛCDM (*black*) and the central void model (*red*).

Chapter 12

Conclusions

In this third and last part of our thesis, we have been studying inhomogeneous alternatives to the Standard Cosmological Model. We investigated a Swiss-Cheese Universe and central void models in order to determine the effects on cosmological parameters caused by their respective inhomogeneities. Our results, together with other researches in this domain, confirm the interest of such models and prove that cosmologists' mind must remain open to new, more realistic ideas.

12.1 Swiss-Cheese Universe: Influence on Cosmological Parameters

The Swiss-Cheese Universe is arguably the most intriguing inhomogeneous alternative to ΛCDM. It proposes to see our world as a combination of cosmological voids surrounded by walls of matter. Although originally designed as a substitute to Dark Energy, the Swiss-Cheese pattern does not allow for a consistent Universe with $\Omega_\Lambda = 0$. But the effects caused by its inhomogeneities can be significant, and we chose to calculate them for the DE equation of state.

12.1.1 Effects of Voids on the EOS of Dark Energy

There are more than 100 supernovae below $z = 0.04$ in the Union2 data set so it is not surprising that including or not including them can have a considerable effect on the reconstruction of the equation state of Dark Energy w. In the same way, changing their error bars changes their pull on the best fit values of w.

In this work, we have shown that the growth of voids in the Universe can have a small effect upon the reconstruction of the equation of state of Dark Energy by inducing scatter into the redshift-luminosity data plane. If one considers only the supernova data, the effect of the voids may be relatively large, up to around 10% of the central value of w, becoming less as one increases the minimum redshift supernovae included in the fit.

When one includes the constraints from the CMB and from Baryonic Acoustic Oscillations, the magnitude of the effect is much smaller, below the percentage level. However, the induced error does start to compare with some of the other smaller errors that are considered by the Union2 team which are listed in

table 9 of [33]. This error is not important now and may turn out to be dwarfed by other systematics even in future studies using data from new observational programs. Conversely, one can invisage a situation where it would have an important effect upon the understanding of Dark Energy and we would need to parametrise and quantify our uncertainty.

If we consider dark energy with an equation of state which is allowed to vary, i.e. $w(z) = w_o + w_a z/(1+z)$, we find that the effect of the uncertainty introduced due to the voids is amplified and the best fit values of w_o and w_a can change around 10%, unless we neglect all supernovae at redshifts lower than $z \sim 0.04$. The magnitude of the errors around these best fit regions also increase significantly.

Another approach to understand the distribution of these voids and their effect is to try and map out the local voids using peculiar velocity flows in an attempt to quantify their effect. This seems difficult : a redshift of $z \sim 0.04$ corresponds to a comoving distance of roughly 150 Mpc. The size of typical voids in the Universe today is considerably smaller than this, of the order of 10-20 Mpc in radius. We should therefore expect many hundreds of voids to be present in this low redshift part of the Hubble diagram and it seems impossible to trace them given our lack of understanding of bias and the history of structure formation in the local Universe. What we do know is that there are voids, their gravitational potential may have implications for the reconstruction of w and we can in principle quantify this uncertainty.

12.2 Alternative View of Central Void Models

Within the extended family of inhomogeneous models, central void models have proven efficient at describing cosmological observations, but at a cost. Indeed, they assume that the observer lives near the centre of a large underdensity which can mimick the effects of Dark Energy. Because of observational constraints, however, the observer cannot be situated too far from the middle of the void. This non-generic situation is in strong disagreement with the Copernican principle which states that we should not stand in a specially favoured position.

Despite some weaknesses in the central void paradigm, we believe that it should not be discarded with disdain. These models offer an alternative view on our cosmos which might help us understand it better. We should not consider them as a perfect description of reality, but the different approach they provide can lead us towards a more complete and more realistic model of our Universe. Applying inhomogeneous models to specific studies like the Extragalactic Background Light allows us to potentially rule out some of them, as they might sometimes appear to be in conflict with observations. More data need to be collected and refined models have to be built, but the important thing is to keep an open mind about our cosmological understanding of the Universe.

Bibliography

[1] E. Carretta *et al.*, "Distances, ages, and epoch of formation of globular clusters," Astrophys. J. 533, 215 (2000) [arXiv:astro-ph/9902086].

[2] R. Jimenez *et al.*, "Ages of globular clusters: a new approach," Mon. Not. Roy. Astron. Soc. **282**, 926 (1996) [arXiv:astro-ph/9602132].

[3] B. M. S. Hansen *et al.*, "The White Dwarf Cooling Sequence of the Globular Cluster Messier 4," Astrophys. J. 574, L155 (2002) [arXiv:astro-ph/0205087].

[4] J. R. Bond and G. Efstathiou, "Cosmic background radiation anisotropies in universes dominated by nonbaryonic dark matter," Astrophys. J. 285, L45 (1984).

[5] P. J. E. Peebles and J. T. Yu, "Primeval Adiabatic Perturbation in an Expanding Universe," Astrophys. J. 162, 815 (1970).

[6] D. Sapone, "Dark Energy in Practice," Intern. J. of Mod. Phys. **25**, 5253 (2010) [arXiv:1006.5694 [astro-ph.CO]].

[7] J. Silk, "Cosmic Black-Body Radiation and Galaxy Formation," Astrophys. J. 151, 459 (1968).

[8] E. Komatsu *et al.*, "Seven-year Wilkinson Microwave Anisotropy Probe (WMAP) Observations: Cosmological Interpretation," Astrophys. J. Suppl. **192**, 18 (2011) [arXiv:1001.4538 [astro-ph.CO]].

[9] A. Meiksin, M. White and J. A. Peacock, "Baryonic signatures in large-scale structure," Mon. Not. Roy. Astron. Soc. **304**, 851 (1999) [arXiv:astro-ph/9812214].

[10] V. Springel *et al.*, "Simulations of the formation, evolution and clustering of galaxies and quasars," Nature **435**, 629 (2005) [arXiv:astro-ph/0504097].

[11] H. J. Seo and D. J. Eisenstein, "Baryonic Acoustic Oscillations in Simulated Galaxy Redshift Surveys," Astrophys. J. **633**, 575 (2005) [arXiv:astro-ph/0507338].

[12] D. J. Eisenstein, H. J. Seo and M. White, "On the Robustness of the Acoustic Scale in the Low-Redshift Clustering of Matter," Astrophys. J. **664**, 660 (2007) [arXiv:astro-ph/0604361].

[13] C. Blake and K. Glazebrook, "Probing Dark Energy Using Baryonic Oscillations in the Galaxy Power Spectrum as a Cosmological Ruler," Astrophys. J. **594**, 665 (2003) [arXiv:astro-ph/0301632].

[14] S. Cole *et al.*, "The 2dF Galaxy Redshift Survey: power-spectrum analysis of the final data set and cosmological implications," Mon. Not. Roy. Astron. Soc. **362**, 505 (2005) [arXiv:astro-ph/0501174].

[15] D. J. Eisenstein *et al.*, "Detection of the Baryon Acoustic Peak in the Large-Scale Correlation Function of SDSS Luminous Red Galaxies," Astrophys. J. **633**, 560 (2005) [arXiv:astro-ph/0501171].

[16] M. Colless *et al.*, "The 2dF Galaxy Redshift Survey: spectra and redshifts," Mon. Not. Roy. Astron. Soc. **328**, 1039 (2001) [arXiv:astro-ph/0106498].

[17] D. G. York *et al.* (SDSS Collaboration), "The Sloan Digital Sky Survey: Technical Summary," Astron. J. **120**, 1579 (2000) [arXiv:astro-ph/0006396].

[18] M. Tegmark *et al.* (SDSS Collaboration), "Cosmological constraints from the SDSS luminous red galaxies," Phys. Rev. D. **74**, 123507 (2006) [arXiv:astro-ph/0608632].

[19] S. Weinberg, "The Cosmological Constant Problem," Rev. Mod. Phys. **61**, 1 (1989).

[20] S. W. Hawking, "The Cosmological Constant Is Probably Zero," Phys. Lett. B **134**, 403 (1984).

[21] J. Yokoyama, "A cosmological constant from degenerate vacua," Phys. Rev. Lett. **88**, 151302 (2002) [arXiv:hep-th/0110137].

[22] S. Mukohyama and L. Randall, "A Dynamical Approach to the Cosmological Constant," Phys. Rev. Lett. **92**, 211302 (2004) [arXiv:hep-th/0306108].

[23] A. J. Albrecht and P. J. Steinhardtm, "Cosmology For Grand Unified Theories With Radiatively Induced Symmetry Breaking," Phys. Rev. Lett˙**48**, 1220 (1982).

[24] S. Dodelson, M. Kaplinghat and E. Stewart, "Solving the Coincidence Problem: Tracking Oscillating Energy," Phys. Rev. Lett˙**85**, 5276 (2000) [arXiv:astro-ph/0002360].

[25] L. P. Chimento *et al.*, "Interacting quintessence solution to the coincidence problem," Phys. Rev. D **67**, 083513 (2003) [arXiv:astro-ph/0303145].

[26] R.-G. Cai and A. Wang, "Cosmology with interaction between phantom dark energy and dark matter and the coincidence problem," Journ. of Cosm. and Astropart. Phys. **3**, 002 (2005) [arXiv:hep-th/0411025].

[27] B. Hu and Y. Ling, "Interacting dark energy, holographic principle, and coincidence problem," Phys. Rev. D **73**, 123510 (2006) [arXiv:hep-th/0601093].

[28] R. R. Caldwell, R. Dave and P. J. Steinhardt, "Cosmological imprint of an energy component with general equation of state," Phys. Rev. Lett. **80**, 1582 (1998) [arXiv:astro-ph/9708069].

[29] B. W. Carroll and D. A. Ostlie, "An Introduction to Modern Astrophysics," Pearson International Edition (San Fransisco, 2007).

[30] A. G. Riess, W. H. Press and R. P. Kirshner, "Using Type IA supernova light curve shapes to measure the Hubble constant," Astrophys. J. 438, L17 (1995) [arXiv:astro-ph/9410054].

[31] S. Perlmutter *et al.*, "Measurements of Omega and Lambda from 42 High-Redshift Supernovae," Astrophys. J. 517, 565 (1998) [arXiv:astro-ph/9812133].

[32] M. Hamuy *et al.*, "The Hubble Diagram of the Calan/Tololo Type IA Supernovae and the Value of HO," Astrophys. J. 112, 2398 (1996) [arXiv:astro-ph/9609062].

[33] R. Amanullah *et al.*, "Spectra and Light Curves of Six Type Ia Supernovae at $0.511 < z < 1.12$ and the Union2 Compilation," Astrophys. J. 716, 712 (2010) [arXiv:1004.1711 [astro-ph.CO]].

[34] F. Hoyle and M. S. Vogeley, "Voids in the Two-Degree Field Galaxy Redshift Survey," Astrophys. J. **607**, 751 (2004) [arXiv:astro-ph/0312533].

[35] D. C. Pan *et al.*, "Cosmic Voids in Sloan Digital Sky Survey Data Release 7," arXiv:1103.4156 [astro-ph.CO].

[36] M. Boylan-Kolchin *et al.*, "Resolving cosmic structure formation with the Millennium-II Simulation," Mon. Not. Roy. Astron. Soc. **398**, 1150 (2009) [arXiv:0903.3041 [astro-ph.CO]].

[37] R. Van de Weygaert and E. Platen, "Cosmic Voids: Structures, Dynamics and Galaxies," arXiv:0912.2997 [astro-ph.CO].

[38] R. A. Vanderveld, E. E. Flanagan and I. Wasserman, "Luminosity distance in "Swiss cheese" cosmology with randomized voids. I. Single void size," Phys. Rev. D. **78**, 083511 (2008) [arXiv:0808.1080 [astro-ph]].

[39] V. Marra, E. W. Kolb, S. Matarrese and A. Riotto, "Cosmological observables in a Swiss-cheese universe," Phys. Rev. D. **76**, 123004 (2007) [arXiv:0708.3622 [astro-ph]].

[40] H. Kozaki and K.-I. Nakao, "Volume expansion of a Swiss-cheese universe," Phys. Rev. D. **66**, 104008 (2002) [arXiv:gr-qc/0208091].

[41] N. Brouzakis, N. Tetradis and E. Tzavara, "The effect of large scale inhomogeneities on the luminosity distance," Journ. of Cosm. and Astropart. Phys. **2**, 13 (2007) [arXiv:astro-ph/0612179].

[42] N. Brouzakis and N. Tetradis, "Analytical estimate of the effect of spherical inhomogeneities on luminosity distance and redshift," Phys. Rev. B. **665**, 344 (2008) [arXiv:0802.0859 [astro-ph]].

[43] S. Ghassemi, S. K. Moghaddam and R. Mansouri, "Lensing effects in inhomogeneous cosmological models," Phys. Rev. D. **79**, 102002 (2009) [arXiv:0901.0340 [astro-ph.CO]].

[44] V. Marra, E. W. Kolb and S. Matarrese, "Light-cone averages in a swiss-cheese universe," Phys. Rev. D. **77**, 023003 (2008) [arXiv:0710.5505 [astro-ph]].

[45] A. Einstein and E. G. Strauss, "The influence of the expansion of space on the gravitation fields surrounding the individual stars," Rev. Mod. Phys. **17**, 120 (1945).

[46] W. Valkenburg, "Swiss Cheese and a Cheesy CMB," Journ. of Cosm. and Astropart. Phys. **6**, 10 (2009) [arXiv:0902.4698 [astro-ph.CO]].

[47] J. W. Moffat and D. C. Tatarski, "Redshift and structure formation in a spatially flat inhomogeneous universe," Phys. Rev. D. **45**, 3512 (1992).

[48] J. W. Moffat and D. C. Tatarski, "Cosmological Observations in a Local Void," Astrophys. J. **453**, 17 (1995) [arXiv:astro-ph/9407036].

[49] K. Tomita, "Distances and Lensing in Cosmological Void Models," Astrophys. J. **529**, 38 (2000) [arXiv:astro-ph/9906027].

[50] K. Tomita, "Analyses of Type Ia Supernova Data in Cosmological Models with a Local Void," Prog. of Theor. Phys. **106**, 929 (2001) [arXiv:astro-ph/0104141].

[51] H. Alnes, M. Amarzguioui and O. Gron, "Inhomogeneous alternative to dark energy?," Phys. Rev. D. **73**, 083519 (2006) [arXiv:astro-ph/0512006].

[52] S. Alexander *et al.*, "Local void vs dark energy: confrontation with WMAP and type Ia supernovae," J. of Cosm. and Astrop. Phys. **9**, 25 (2009) [arXiv:0712.0370 [astro-ph]].

[53] A. Blanchard *et al.*, "Large-scale galaxy correlations as a test for dark energy," Astron. and Astroph. **449**, 925 (2006) [arXiv:astro-ph/0512085].

[54] J. Garcia-Bellido and T. Haugbolle, "Looking the void in the eyes - the kinematic Sunyaev Zeldovich effect in Lemaître Tolman Bondi models," J. of Cosm. and Astrop. Phys. **9**, 16 (2008) [arXiv:0807.1326 [astro-ph]].

[55] T. Clifton, P. G. Ferreira and K. Land, "Living in a Void: Testing the Copernican Principle with Distant Supernovae," Phys. Rev. Lett. **101**, 131302 (2008) [arXiv:0807.1443 [astro-ph]].

[56] M. Kowalski *et al.*, "Improved Cosmological Constraints from New, Old, and Combined Supernova Data Sets," Astrophys. J. **686**, 749 (2008) [arXiv:0804.4142 [astro-ph]].

[57] S. Nadathur and S. Sarkar, "Reconciling the local void with the CMB," Phys. Rev. D. **83**, 063506 (2010) [arXiv:1012.3460 [astro-ph.CO]].

[58] M. Blomqvist and E. Moertsell, "Supernovae as seen by off-center observers in a local void," J. of Cosm. and Astrop. Phys. **5**, 6 (2010) [arXiv:0909.4723 [astro-ph.CO]].

[59] G. Lemaître, "L'Univers en expansion," Annales Soc. Sci. Brux. **A53**, 51 (1933).

[60] R. C. Tolman, "Effect of Inhomogeneity on Cosmological Models," Proc. Nat. Acad. Sci. **20**, 169 (1934).

[61] H. Bondi, "Spherically symmetrical models in general relativity," Mon. Not. Roy. Astron. Soc. **107**, 410 (1947).

[62] V. Kostov, "Average luminosity distance in inhomogeneous universes," arXiv:0910.2611 [astro-ph.CO].

[63] A. Labatie *et al.*, "Uncertainty in 2-point correlation function estimators and BAO detection in SDSS DR7," arXiv:1009.1232 [astro-ph.CO].

[64] E. Komatsu *et al.*, "Seven-year Wilkinson Microwave Anisotropy Probe (WMAP) Observations: Cosmological Interpretation," Astrophys. J. Suppl. **192**, 18 (2011) [arXiv:1001.4538 [astro-ph.CO]].

[65] M. Chevallier and D. Polarski, "Accelerating Universes with Scaling Dark Matter," Intern. J. of Mod. Phys. **10**, 213 (2001) [arXiv:gr-qc/0009008]].

[66] E. V. Linder, "Exploring the Expansion History of the Universe," Phys. Rev. Lett. **90**, 091301 (2003) [arXiv:astro-ph/0208512].

[67] H. Alnes and M. Amarzguioui, "CMB anisotropies seen by an off-center observer in a spherically symmetric inhomogeneous universe," Phys. Rev. D. **74**, 103520 (2006) [arXiv:astro-ph/0607334].

[68] H. Alnes and M. Amarzguioui, "Supernova Hubble diagram for off-center observers in a spherically symmetric inhomogeneous universe," Phys. Rev. D. **75**, 023506 (2007) [arXiv:astro-ph/0610331].

[69] K. Bolejko and P. D. Lasky, "Pressure gradients, shell-crossing singularities and acoustic oscillations - application to inhomogeneous cosmological models," Mon. Not. Roy. Astron. Soc. **391**, L59 (2008) [arXiv:0809.0334 [astro-ph]].

[70] P. Valageas, "Impact of shell crossing and scope of perturbative approaches, in real and redshift space," Astron. and Astroph. **526**, A67 (2011) [arXiv:1009.0106 [astro-ph.CO]].

[71] S. M. Goncalves, "Shell crossing in generalized Tolman-Bondi spacetimes," Phys. Rev. D. **63**, 124017 (2001) [arXiv:gr-qc/0107087].

[72] M. Le Delliou, F. C. Mena and J. P. Mimeso, "Role of shell crossing on the existence and stability of trapped matter shells in spherical inhomogeneous Λ-CDM models," Phys. Rev. D. **83**, 103528 (2011) [arXiv:1103.0976 [gr-qc]].

[73] A. Krasinski, "Inhomogeneous Cosmological Models," Cambridge University Press (1997).

[74] W. B. Bonnor and A. Chamorro, "Models of voids in the expanding universe," Astrophys. J. **361**, 21 (1990).

[75] A. Chamorro, "Models of voids in elliptic universes," Astrophys. J. **383**, 51 (1991).

[76] H. Sato, in "General Relativity and Gravitation," eds. B. Bertotti, F. de Felice and A. Pascolini, Reidel, Dordrecht (1984).

[77] Y. Suto, K. Sato and H. Sato, "Expansion of Voids in a Matter-Dominated Universe," Prog. of Theor. Phys. **71**, 938 (1984).

[78] N. Metropolis and S. Ulam, "The Monte Carlo Method," Jour. of American Stat. Ass. **44** 247, 335 (1949).

[79] W. K. Hastings, "Monte Carlo sampling methods using Markov chains and their application," Biometrika **57**, 97 (1970).

[80] J. Garcia-Bellido and T. Haugbolle, "Confronting Lemaitre Tolman Bondi models with observational cosmology," J. of Cosm. and Astrop. Phys. **4**, 3 (2008) [arXiv:0802.1523 [astro-ph]].

[81] T. Biswas, A. Notari and W. Valkenburg, "Testing the void against cosmological data: fitting CMB, BAO, SN and H0," J. of Cosm. and Astrop. Phys. **11**, 30 (2010) [arXiv:1007.3065 [astro-ph.CO]].

[82] A. Moss, J. P. Zibin and D. Scott, "Precision cosmology defeats void models for acceleration," Phys. Rev. D. **83**, 103515 (2011) [arXiv:1007.3725 [astro-ph.CO]].

[83] S. Foreman, A. Moss, J. P. Zibin and D. Scott, "Spatial and temporal tuning in void models for acceleration," Phys. Rev. D. **83**, 103532 (2011) [arXiv:1009.0273 [astro-ph.CO]].

[84] A. Clocchiatti *et al.*, "Hubble Space Telescope and Ground-based Observations of Type Ia Supernovae at Redshift 0.5: Cosmological Implications," Astrophys. J. **642**, 1 (2006) [arXiv:astro-ph/0510155].

[85] Z. Li, P. Wu and H. Yu, "Examining the cosmic acceleration with the latest Union2 supernova data," Phys. Lett. B. **695**, 1 (2011) [arXiv:1011.1982 [gr-qc]].

[86] D. Adak, A. Bandyopadhyay and D. Majumdar, "Reconstructing the equation of state and density parameter for dark energy from combined analysis of recent SNe Ia, OHD and BAO data," arXiv:1102.4726 [astro-ph.CO].

[87] A. G. Riess *et al.*, "A 3% Solution: Determination of the Hubble Constant with the Hubble Space Telescope and Wide Field Camera 3," Astrophys. J. **730**, 119 (2011) [arXiv:1103.2976 [astro-ph.CO]].

[88] F. Beutler *et al.*, "The 6dF Galaxy Survey: baryon acoustic oscillations and the local Hubble constant," Mon. Not. Roy. Astron. Soc. **416**, 3017 (2011) [arXiv:1106.3366 [astro-ph.CO]].

[89] https://www.cfa.harvard.edu/ dfabricant/huchra/hubble/

[90] J. D. Finske, S. Razzaque and C. D. Dermer, "Modeling the Extragalactic Background Light from Stars and Dust," Astrophys. J. **712**, 238 (2010) [arXiv:0905.1115 [astro-ph.HE]].

[91] P. P. Eggleton, C. Tout and M. J. Fitchett, "The distribution of visual binaries with two bright components," Astrophys. J. **347**, 998 (1989).

[92] A. M. Hopkins, "On the Evolution of Star-forming Galaxies," Astrophys. J. **615**, 209 (2004) [arXiv:astro-ph/0407170].

[93] C. K. Xu *et al.*, "Number Counts of GALEX Sources in Far-Ultraviolet (1530 Å) and Near-Ultraviolet (2310 Å) Bands," Astrophys. J. **619**, L11 (2005) [arXiv:astro-ph/0411317].

[94] J. P. Gardner, T. M. Brown and H. C. Ferguson, "ULTRAVIOLET GALAXY COUNTS FROM SPACE TELESCOPE IMAGING SPECTROGRAPH OBSERVATIONS OF THE HUBBLE DEEP FIELDS," Astrophys. J. **542**, L79 (2000) [arXiv:astro-ph/0008247].

[95] A. Garzian *et al.*, "Wide and deep near-UV (360 nm) galaxy counts and the extragalactic background light with the Large Binocular Camera," Astron. and Astroph. **505**, 1041 (2009) [arXiv:0906.4035 [astro-ph.CO]].

[96] P. Madau and L. Pozzetti, "Deep galaxy counts, extragalactic background light and the stellar baryon budget," Mon. Not. Roy. Astron. Soc. **312**, L9 (2000) [arXiv:astro-ph/9907315].

[97] R. C. Keenan *et al.*, "The Resolved Near-infrared Extragalactic Background," Astrophys. J. **723**, 40 (2010) [arXiv:1102.2428 [astro-ph.CO]].

[98] G. G. Fazio *et al.*, "Number Counts at 3 μm $< \lambda <$ 10 μm from the Spitzer Space Telescope," Astrophys. J. Suppl. Series **154**, 39 (2004) [arXiv:astro-ph/0405595].

[99] A. Franceschini *et al.*, "A long-wavelength view on galaxy evolution from deep surveys by the Infrared Space Observatory," Astron. and Astroph. **378**, 378 (2001) [arXiv:astro-ph/0108292].

[100] H. Dole *et al.*, "The cosmic infrared background resolved by Spitzer. Contributions of mid-infrared galaxies to the far-infrared background," Astron. and Astroph. **451**, 417 (2006) [arXiv:astro-ph/0603208].

[101] Y. Matsuoka *et al.*, "Cosmic Optical Background: The View from Pioneer 10/11," Astrophys. J. **736**, 119 (2011) [arXiv:1106.4413 [astro-ph.CO]].

[102] E. L. Wright, "DIRBE minus 2MASS: Confirming the Cosmic Infrared Background at 2.2 Microns," Astrophys. J. **553**, 538 (2001) [arXiv:astro-ph/0004192].

[103] L. Chambresy *et al.*, "The Cosmic Infrared Background at 1.25 and 2.2 Microns Using DIRBE and 2MASS: A Contribution Not Due to Galaxies?," Astrophys. J. **555**, 563 (2001) [arXiv:astro-ph/0103078].

[104] V. Gorjian, E. L. Wright and R. R. Chary, "Tentative Detection of the Cosmic Infrared Background at 2.2 and 3.5 Microns Using Ground-based and Space-based Observations," Astrophys. J. **536**, 550 (2000) [arXiv:astro-ph/0103101].

[105] S. Matsuura *et al.*, "Detection of the Cosmic Far-infrared Background in AKARI Deep Field South," Astrophys. J. **737**, 2 (2011) [arXiv:1002.3674 [astro-ph.CO]].

[106] D. J. Schlegel, D. P. Finkbeiner and M. Davis, "Maps of Dust Infrared Emission for Use in Estimation of Reddening and Cosmic Microwave Background Radiation Foregrounds," Astrophys. J. **500**, 525 (1998) [arXiv:astro-ph/9710327].

[107] T. M. Kneiske and H. Dole, "A lower-limit flux for the extragalactic background light," Astron. and Astroph. **515**, A19 (2010) [arXiv:1001.2132 [astro-ph.CO]].

[108] J. Albert *et al.*, "Very-High-Energy Gamma Rays from a Distant Quasar: How Transparent Is the Universe?," Sience **320**, 1752 (2008).

[109] F. W. Stecker, M. A. Malkan and S. T. Scully, "Intergalactic Photon Spectra from the Far-IR to the UV Lyman Limit for $0 < z < 6$ and the Optical Depth of the Universe to High-Energy Gamma Rays," Astrophys. J. **648**, 774 (2006) [arXiv:astro-ph/0510449].

[110] J. R. Primack, J. S. Bullock and R. S. Somerville, "Observational Gamma-ray Cosmology," AIPC **745**, 23 (2005) [arXiv:astro-ph/0502177].

Aknowledgements

Undertaking my PhD at the University of London was for me a great honour and a real pleasure. I felt incredibly privileged to be allowed to study the subjects of astrophysics and cosmology which are of greatest interest to me. Their diversity as well as the range of methods covered during my thesis provided me with a wider and deeper understanding of the present scientific challenges in these domains.

I would like to take this opportunity to thank all the people who helped me during this fascinating journey, and in particular:

- my supervisors, Dr Malcolm Fairbairn and Prof. Mairi Sakellariadou, for their insight and their patient guidance;
- my family, and specially my parents, for their loving support;
- Jessica, for her inspiring love;
- my colleagues and all members of staff at King's College London, as well as all the brilliant minds I was lucky enough to encounter on my way.

This work received the benefit of funding from the Graduate School of King's College London.

List of Figures

List of Tables

List of Abbreviations

2dF	Two-Degree-Field Galaxy Redshift Survey
ΛCDM	Cosmological model with cosmological constant and Cold Dark Matter
BAO	Baryonic Acoustic Oscillations
BH	Black Hole
CDMS	Cryogenic Dark Matter Search
CMB(R)	Cosmological Microwave Background (Radiation)
CoGeNT	Coherent Germanium Neutrino Technology
DAMA	Dark Matter
DE	Dark Energy
DM	Dark Matter
EOS	Equation of State
F(L)RW	Friedmann-(Lemaître-)Robertson-Walker
GC	Galactic Centre
GR	General Relativity
IMBH	Intermediate Mass Black Hole
LHC	Large Hadron Collider
LRG	Luminous Red Galaxy
LTB	Lemaître-Tolman-Bondi
MCMC	Monte Carlo Marko Chain
MOND	Modified Newtonian Dynamics
NFW	Navarro-Frenk-White
NS	Neutron Star
ODE	Ordinary Differential Equation
PDF	Probability Distribution Function
SDSS	Sloan Digital Sky Survey
SM	Standard Model
SMBH	Super Massive Black Hole
SN(e) Ia	Type Ia Supernova(e)
WIMP(s)	Weakly Interactive Massive Particle(s)
WMAP	Wilkinson Microwave Anisotropy Probe
ZAMS	Zero-Age Main Sequence